2016

Mathematical Scaling and Statistical Modeling of Geopressured Geothermal Reservoirs

Esmail Ansari
Louisiana State University and Agricultural and Mechanical College

MATHEMATICAL SCALING AND STATISTICAL MODELING OF GEOPRESSURED GEOTHERMAL RESERVOIRS

A Dissertation

Submitted to the Graduate Faculty of the
Louisiana State University and
Agricultural and Mechanical College
in partial fulfillment of the
requirements for the degree of
Doctor of Philosophy

in

The Craft & Hawkins Department of Petroleum Engineering

by
Esmail Ansari
B.S. in Petroleum Engineering, Sharif University of Technology, 2009
M.S. in Petroleum Engineering, Sharif University of Technology, 2011
May 2016

Acknowledgments

I am most grateful to my advisor, Dr. Richard Hughes, for providing me with the guidance and resources. I also thank him for giving me an opportunity to instruct a reservoir simulation lab which was helpful in solving some of my research problems. I gratefully thank my previous advisor, Dr. Christopher D. White, for pushing and introducing me to the beautiful world of statistics and R. This work would have not been possible without Dr. Hughes and Dr. White's patience and support.

I thank my committee members, Dr. Stephen Sears, Dr. Mayank Tyagi, Dr. Barbara Dutrow and Dr. Blaise Bourdin for their invaluable criticisms that have given shape to this work

I gratefully acknowledge financial support for this work from the US Department of Energy under grant DE-EE0005125. I thank the Computer Modeling Group for providing reservoir simulation software. Special thanks to R development team and their contributers. I thank the Center for Computation and Technology (CCT) at LSU for granting me access to High Performance Computing (HPC) resources. We also thank the members of the LSU Geothermal team for their comments, suggestions and ideas supporting our efforts.

This work is dedicated to my parents: Ahmad Ansari and Kheyronnesa Ghaedi.

Table of Contents

List of Tables

List of Figures

List of Abbreviations

ANOVA	Analysis Of Variance
CCD	Central Composite Design
CMG	Computer Modeling Group
DA	Dimensional Analysis
DHE	Downhole Heat Exchanger
DOE	Design Of Experiments
HSS	Hammersley Sequence Sampling
IA	Inspectional Analysis
MC	Monte Carlo
RSM	Response Surface Method
ZMW	Zero Mass Withdrawal

List of Nomenclature

c	Compressibility	Pa^{-1}
C_p	Isobaric specific heat capacity	$J.kg^{-1}.K^{-1}$
C_v	Volumetric specific heat capacity	$J.kg^{-1}.K^{-1}$
$\mathbf{g}$	Gravity vector	$m.s^{-2}$
H	Reservoir thickness	m
$\mathcal{H}$	Enthalpy	J
$\mathbf{K}$	Permeability tensor	m^2
k_x, k_y, k_z	Directional permeabilities	m^2
L	Reservoir length	m
M	Matrix/fluid heat capacity ratio	$-$
PV	Pore volume (ϕLWH)	m^3
p	Pressure	Pa
q	Flow rate	$m^3.s^{-1}$
T	Temperature	K
t	Time	s
U	Internal energy	J
u_T	Injection/Production velocity	$m.s^{-1}$
$\mathbf{u}$	Interstitial fluid velocity	$m.s^{-1}$
W	Reservoir width	m

Greek

ϕ	Porosity	$-$
$\alpha, \alpha_X, \alpha_Y$	Dip angle	$^\circ$
β	Thermal expansivity	K^{-1}
ρ	Density	$kg.m^{-3}$

τ	Geothermal gradient	$K.m^{-1}$
π	Scale group	$-$
$\boldsymbol{\lambda}$	Thermal conductivity tensor	$W.m^{-1}.K^{-1}$
λ	Thermal conductivity	$W.m^{-1}.K^{-1}$
κ	Thermal diffusivity	$m^2.s^{-1}$
μ	Viscosity	$Pa.s$

Subscript

$1\,or\,2$	Scale factor number
avg	Average
D	Dimensionless
f	Fluid
i	Initial
inj	Injection
r	Rock
ref	Reference
t	Total
ϕ	Pore

Superscript

$*$	Denotes a scale factor

Other Symbols

$\forall$	For all
$\nabla.$	Divergence
∇	Gradient

Abstract

The interest for developing geopressured-geothermal reservoirs along the US Gulf Coast is increasing for securing energy needs and reducing global warming. Identifying the most attractive candidate reservoirs for geothermal energy production requires quick and simple models. Analytical models are not always available and simulating each case individually is expensive. The use of scaling and statistical modeling is one approach to translate the output of a simulator into quick models with general applicability at all scales. The developed models can quickly estimate temperature and thermal energy recovery from the geopressured-geothermal reservoirs. These models can screen large databases of reservoirs to select the most attractive ones for geothermal energy production.

This study presents two different designs for extracting energy from geopressured-geothermal reservoirs: Regular line drive and Zero Mass Withdrawal (ZMW). First, the governing partial differential equations describing each design are derived from the fundamental equations. Inspectional analysis on the partial differential equations of each design provides the most succinct and meaningful form of the dimensionless numbers for scaling the designs. The dimensionless numbers are tested and verified by selecting models with identical dimensionless numbers but different dimensional parameters.

For creating the response models, statistics is used to find the important dimensionless numbers for predicting the response systematically. A procedure is used to compare possible sub-models and to select the best one. These simplified final models are then presented and assessed using testing runs. Applications of these models are presented.

To test the response models, two field cases from southern Louisiana are evaluated: the Gueydan Dome reservoir and the Sweet Lake reservoir. The Gueydan Dome reservoir (Vermilion parish, LA) is investigated using an optimization algorithm and it is concluded that the temperature map should be used for pre-development heat extraction assessments. The Sweet Lake reservoir (Cameron parish, LA) is studied using this conclusion.

Chapter 1

Introduction

The search for clean alternative energy resources to replace fossil fuels is important for securing the world's energy future and reducing global warming. Geothermal energy is an environmentally friendly alternative, although only a small fraction of the available geothermal energy can be economically produced with current technology. Thirty percent of the world's geothermal energy is produced in the USA, mostly in California and Nevada (GEA, 2012). The US Gulf Coast has geothermal energy potential in hot geopressured aquifers that have been extensively penetrated and mapped in the process of oil and gas exploration.

1.1 Previous work

Louisiana's geopressured sedimentary aquifers have been examined previously (Bassiouni, 1980; Bebout et al., 1981; McMullan and Bassiouni, 1984). However, these resources have not been developed, and uncertainty associated with their economics persists. For example, Quitzau and Bassiouni (1981) used Monte Carlo sampling to assess the effects of uncertainty on the controlling parameters to evaluate commercial production of dissolved gas from Louisiana's geothermal resources. They concluded that development of these reservoirs was not economically viable. However, they indicated that conversion of an unsuccessful oil or gas well into a geopressured brine well could be economically feasible if environmental and legal concerns could be overcome.

Griggs (2004) examined coproduction of geothermal energy and dissolved natural gas. He used an experimental design to generate a response surface to evaluate coproduction from Louisiana's geothermal reservoirs and concluded that a minimum bulk volume of 1.05 cubic kilometers is required for a single well to be a candidate for geothermal and natural gas coproduction.

Gray and Nunn (2010) studied the geothermal energy potential associated with salt domes in the Camerina A zone near the Gueydan field in Louisiana. They found that heat flow through the salt dome had limited impact on the geothermal potential of the reservoir because of the moderate burial depth.

Plaksina et al. (2011) studied the effects of coupled free convection and CO_2 injection on heat extraction from an idealized sedimentary geothermal reservoir. Their work indicated that more than 25 percent of the sensible energy could be extracted in a 30 year project life. They also compared wellbore chilling to geofluid production to the surface for heat extraction and showed that production is the more effective option. They did not assess the maximum net energy that could be produced from an actual geopressured geothermal reservoir.

1.2 Motivation and purpose

The interest in developing Gulf Coast geothermal reservoirs encourages identifying economically attractive candidates. Most of these reservoirs were produced only for a short period of time and available production data for them is limited. Detailed reservoir simulation and assessment of these resources is too costly and time-consuming. The work presented in this dissertation provides a detailed predictive model that quickly estimates the potential energy recovery from conventional geothermal reservoirs based on a set of dimensionless groups. The model can also be used for screening large databases of reservoirs to identify potential geopressured geothermal candidates for both conventional heat extraction and Zero Mass Withdrawal (ZMW) designs (the ZMW technique is described in Sec. 1.6).

1.3 Research approach

This research uses geothermal reservoir modeling, dimensional scaling, design of experiments and response surface evaluation to produce screening models for predicting energy recovery from a line drive well orientation system and from the Zero Mass Withdrawal de-

sign in which the heat exchanger is located inside the well. The following sections explain these terminologies and reviews previous work.

1.3.1 Reservoir modeling

Synthetic, yet representative models are developed based on field data. Two dimensional flow models are used for development of a line drive screening model and three dimensional flow models are used for ZMW. The data for these models come from statistical analysis of Gulf Coast geothermal reservoirs (see Chapter 2). An advanced thermal reservoir simulator is used to create the screening models (STARS manual, 2011). For evaluating the screening models, two field cases from southern Louisiana are modeled: the Gueydan Dome reservoir and the Sweet Lake reservoir, located in the Frio formation.

1.3.2 Reservoir Geology

The Frio formation (in southern Louisiana) has the potential for geopressured geothermal energy production (Hoffman et al., 1981). Figure 1.1 shows a vertical cross section of a potential geothermal reservoir located in the Camerina A zone at Gueydan Dome, southwest Louisiana. The Camerina zone is part of the Frio sandstone formation and is deposited during the late Oligocene (ca. 23-34 million years ago). The Gueydan salt dome dates back to the Callovian mid Jurassic (ca. 163-166 million years ago) when a widespread evaporite formation, known as Louann salt, had existed in the current Gulf of Mexico (Gray and Nunn, 2010). A shale sequence (100 to 150 m thick) underlies the Camerina and a shale sequence (365 to 426 m thick) overlies and seals the Camerina at its top. These shale layers show that Camerina has been part of marine transgressive sequence. Surface terrain in the study area is formed by deltaic deposits during late Pleistocene (ca. 11-126 thousand years ago, Gray and Nunn (2010)).

The Sweet Lake geopressured-geothermal aquifer, located southeast of Lake Charles, Louisiana, is a sedimentary basin, in the Miogypsinoides sequence of the Camerina zone of the upper Frio formation (upper Oligocene age). The Sweet Lake aquifer is located in a dipping graben which widens westward (John et al. (1998), see Section 7.2). The Sweet

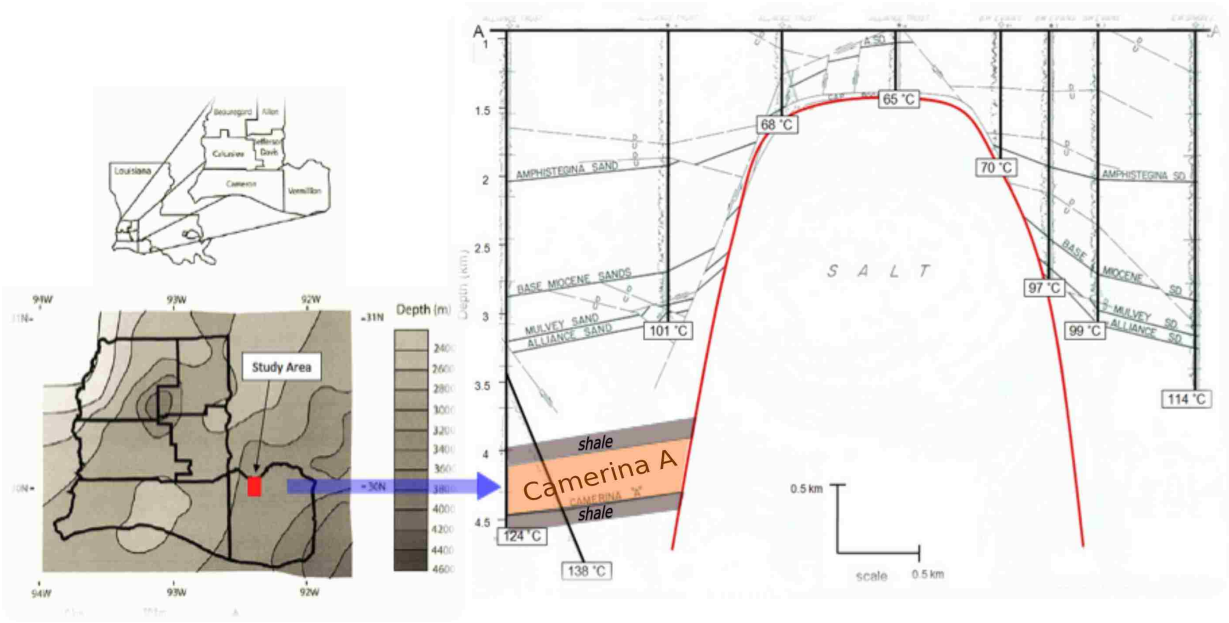

Figure 1.1: Vertical cross section of the Gueydan dome (modified from Robinson (1967)). The Gueydan Dome, located in the Vermilion parish, LA, is shown by the red dot. The Gueydan salt dome and the Camerina A sand zone are shown schematically in the right figure.

Lake aquifer consists of seven sand layers. The sands are medium to fine grained and are made up of 75% quartz, 19% feldspar and 6% clays. Sand production is not expected because the cementing material is quartz overgrowth and small amount of clay is present (Hoffman et al., 1981).

1.3.3 Dimensional scaling

Establishing similarity between different physical phenomena motivates dimensional analysis. Similarity means defining some equivalence between two phenomena and describing them in a more general way (Sonin, 2001). Scaling can also be seen as generalizing the results obtained at one scale size to other scales. There are two methods for defining scaling groups: Inspectional Analysis (IA) and Dimensional Analysis (DA). Each of these methods has advantages and limitations.

Inspectional Analysis is a mathematically rigorous method and requires the differential equations that govern the phenomena to make the dimensional equations dimensionless,

variable-by-variable (Ruark, 1935). In this method, the differential equations of the system are coupled with initial and boundary conditions and the entire system is transformed into dimensionless form to obtain a set of dimensionless groups. When all the groups in the set are independent of each other and every dimensionless group not belonging to the set can be formed by combining the existing groups in the set, the set is complete. IA is a systematic procedure and provides a higher degree of similarity than can be inferred by solely DA. Another advantage of IA is that the physical meaning of most of dimensionless groups are apparent (Ruark, 1935; Sonin, 2001).

Dimensional Analysis uses the primary dimensions of a system to form the scaling groups (Langhaar, 1951). The derived groups only scale the system and may not have physical meanings. A classic way of defining the dimensionless groups is to use Buckingham's π theorem (Buckingham, 1914). Dimensional analysis is useful in experiments when the underlying system of equations are unknown.

In the reservoir engineering context, the physical equations describing the behavior of the reservoir are known and can be described using partial differential equations. IA is used frequently for making these systems dimensionless (Geertsma et al., 1956).

Shook et al. (1992) scaled immiscible line drive waterflooding for a homogeneous two-dimensional cartesian tilted reservoir containing water and oil. They showed that their analytically derived and numerically analyzed dimensionless numbers confirmed the experimental results of Craig et al. (1957). They investigated the effect of dimensionless numbers on breakthrough oil recovery and then eliminated those which had small effects to minimize the number of dimensionless groups. They did not use statistical analysis for eliminating the insignificant factors and did not build a predictive model.

Jin et al. (2010) used IA to derive sixteen dimensionless groups for a novel "downhole water loop (DWL)" smart well completion that reduces the effect of water coning and yields more oil production. They reduced the sixteen dimensionless groups to fourteen after checking for redundancy and interdependence of the groups. They further reduced

the dimensionless groups from fourteen to seven by performing a sensitivity study, similar to the work of Shook et al. (1992).

1.3.4 Design of Experiments (DOE)

Many factors influence the energy recovery in a conventional geothermal system (i.e. not EGS) and the factors that most affect the response will be the focus of this work. Instead of changing factors one-at-a-time, by which, factor interactions cannot be obtained and a large number of simulation runs are needed, factors will be changed systematically using experimental design to reveal effects and interactions using a smaller set of designed simulation runs. Two important designs are the Central Composite Design (CCD) and the Box-Behnken design (Box et al., 2005).

- Central Composite Design (CCD)

Central Composite Designs are complete designs which are used to fit a full quadratic model including all interaction terms. Central Composite Design (CCD) includes all the corners of this n dimensional (n number of cubes) cube when all the factors are scaled between -1 and +1 (Montgomery et al., 1984; Box et al., 2005). In addition, there are several star points along the center of each face of the cube. Depending on where these center points are located along the face, there are three types of CCD. In the Central Composite Faced design (CCF), the star points are located exactly at the center of each face of the cube. In Inscribed design (CCI) and Circumscribed design (CCC), the star points are located inside and outside the face of the cube, respectively.

- Box-Behnken Design

Similar to CCD, Box-Behnken designs can also be used to fit a full quadratic response surface but with fewer simulation runs. This design also has three levels of factors and is rotatable but yields poorer predictions especially in the corners of the cube because it does not consider the corner points. Because Box-Behnken design requires fewer simulation runs, it will be used to fit a full quadratic response surface including all interaction terms to

the detailed simulation results (Box et al., 2005). Figure 1.2 shows Circumscribed Central Composite and the Box-Behnken designs.

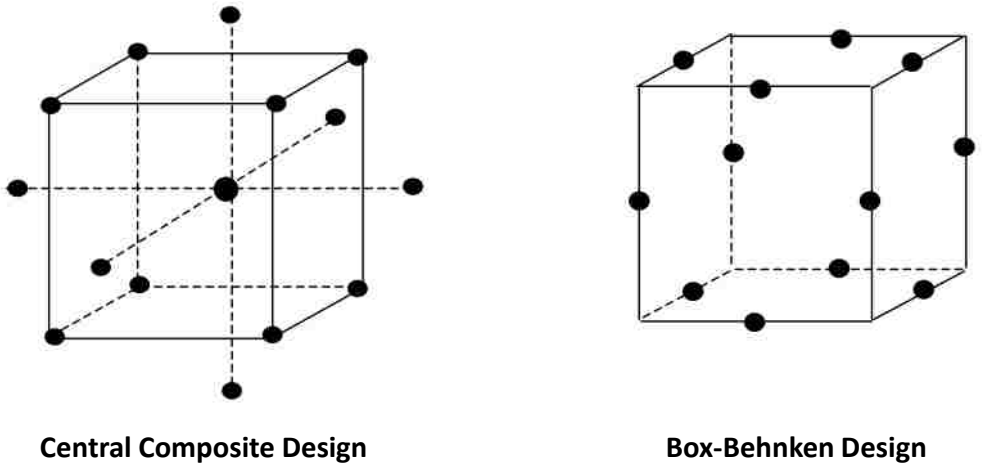

Figure 1.2: Two types of experimental design. The Box-Behnken design is used in this work (from Kalla (2005)).

1.3.5 Response Surface Method

Once the results of the designs are obtained, response surface methods will be used for determining the correlation between the factors and response. Two widely used formulations for the response surfaces are regression and kriging.

- Regression

The least squares method is conventionally used to estimate regression coefficients and fit a model (Montgomery and Myers, 1995). Exploratory data analysis is used to select the best fit to the data. The fitted linear model to the sparse detailed runs can be used to estimate the effect of each parameter on the objective function. This describes how changing the input variables changes the response. A large coefficient indicates that the factor is significantly influential as the parameter value is increased or decreased. Similarly, a small coefficient means that the parameter is not influencing the response. In addition, in order to eliminate the effect of parameter units (for example using bar instead of pascal for pressure), it is necessary to normalize the parameter to have a range from -1 to 1 so that the parameter coefficient is unit-invariant. In order to get a better estimation of the

response, in addition to linear effects, parameter interaction and quadratic effects are also needed. In these cases, a second degree or reduced polynomial model is used. In a reduced model, the unimportant factors and interactions are removed.

- Kriging

An alternative to using polynomials for producing response surfaces is kriging (Simpson et al., 2001; Landa and Bars, 2003). This method linearly combines weighted observations and the weights depend on distances between the target point and the observations. This distance is modeled using semivariogram models and these models can be directional. Covariance between two points depends on the semivariogram distance between them and it decreases as the semivariogram distance increases. Another feature of kriging is that it considers data redundancy and ensures that close points impose appropriate effects in predicting the target. These properties of kriging makes it a best linear unbiased estimator (BLUE) for correlated data.

1.3.6 Sampling

Once the proxy models are constructed, a sampling method is needed to sample the factors and to translate the uncertainty from the input to the response. For doing this, a Monte Carlo or quasi Monte Carlo method, such as Hammersley Sequence Sampling (HSS), is generally used (Kroese et al., 2011; Kalla, 2005).

Monte Carlo methods are random methods and require a large number of runs to uniformly fill the factor space (Figure 1.3). Extensions of Monte Carlo methods are becoming more popular for sampling. One of these quasi Monte Carlo methods is known as a Hammersley sequence (Kalla, 2005).

Unlike Monte Carlo methods which sample dimensional space randomly, a Hammersley sequence fills the space more uniformly. This characteristic is known as low-discrepancy sequence sampling (Kroese et al., 2011).

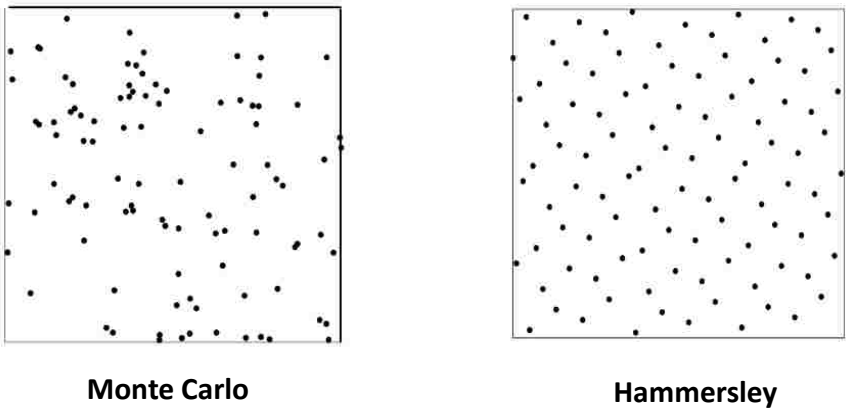

Figure 1.3: Monte Carlo vs. Hammersley method for sampling a two-dimensional factor space. HSS fills the factor space uniformly (Figure from Kalla (2005)).

1.4 Screening model

After scaling the partial differential equations (PDEs that describe the system) and obtaining a complete set of independent and succinct dimensionless groups, screening models are developed. These models are created by fitting polynomial response surfaces to the derived dimensionless groups. Commonly, Box-Behnken or Central composite designs are used to select these simulation runs. In developing screening models, there is no concern about casualty which is often a concern in statistical inference (Mendenhall et al., 2012), because similar partial differential equations are being solved numerically by the simulator. The following studies have used experimental design and response surface with scaling analysis to create screening models

Wood et al. (2008) modified the work of Shook et al. (1992) for predicting CO_2 flooding and storage in Gulf Coast reservoirs. They modified and completed the previous work by proposing five additional dimensionless groups. They proposed these new dimensionless numbers based on simulation results and the effects of various factors. They successfully used Box-Behnken experimental design and polynomial response surface modeling for obtaining predictive models. The authors state that the developed models can be effectively used for screening large reservoir databases to select the best candidates for CO_2 flooding

oil recovery and CO_2 storage. Shook et al. (1992) and Wood et al. (2008) used line drive patterns in their work.

After deriving various dimensionless groups, Jin et al. (2001) used Box-Behnken design to fit a predictive model on these groups for a downhole water loop application. They obtained 36 regression coefficients and reduced it to 7 by removing insignificant coefficients and dropping various interaction terms. They also used analysis of variance (ANOVA) to sort the dimensionless numbers based on their significance and concluded that mobility ratio and aquifer strength are the most important groups affecting movable oil recovery in their system.

Simpson et al. (2001) compared four different modern experimental designs for creating models: Latin hypercube, Hammersley Sequence Sampling (HSS), orthogonal arrays and uniform designs. They concluded that HSS yields more accurate results, effectively and efficiently. Afonja (2013) developed a metamodel for predicting oil recovery performance and pressure difference for use in CO_2-surfactant flooding. He used Hammersley Sequence Sampling instead of classical designs such as Box-Behnken following the work of Simpson et al. (2001).

1.5 Creating the experimental design

There are two approaches for creating the experimental design. One approach is to sample dimensionless space and create the experimental design based on the dimensionless numbers and the second approach is to sample the dimensional space and create the dimensionless numbers using the sampled parameters. Each of these methods have their own advantages and drawbacks. The first approach is useful for checking and validating the relevancy of the dimensionless groups. For validation purpose, it is important to keep some dimensionless numbers constant while changing the parameters. The first approach also requires fewer runs and is speedy, thus more convenient for validation purpose in which the modeler needs to test different sets of dimensionless numbers. The second approach is more useful for sensitivity analysis and model fitting, however it requires more runs.

The dimensionless numbers derived using inspectional analysis are algebraically independent but statistically dependent because they are functions of random parameters (Rice, 2006; Soong, 2004). By selecting the parameters orthogonally in the higher dimension, the correlation between the dimensionless numbers reduces and the multicollinearity in the regression model can be reduced. The second approach also reduces factor confounding in which the effect of one factor (dimensionless number) is obscured by another factor; thus making the results more interpretable.

1.6 Downhole heat exchangers

A downhole heat exchanger can be more economical compared with traditional multiwell heat extraction techniques because it eliminates the need for injection facilities and surface handling of the geofluid and reduces the surface footprint (Lund, 2003). The injected fluid gains energy from the adjacent cap/base rocks and this process helps in the renewability of the reservoir. A DHE also minimizes the geological risks such as induced seismicity or subsidence.

Feng et al. (2014) proposed a compact DHE design to exploit forced convection requiring only a single inclined or horizontal well (Figure 1.4). A downhole heat exchanger injects all the geofluid back into the reservoir withdrawing no mass from the system. An electric submersible pump drives the geofluid from the production to the injection section (Akhmadullin and Tyagi, 2014). This design is based on current drilling and well completion technology and may cut the capital cost significantly compared with traditional heat extraction techniques.

1.7 Research objective

A literature review does not reveal a comprehensive screening model which combines statistics and reservoir engineering to delineate guidelines for economic appraisal of geopressured-geothermal prospects. The primary goal of this research is to present a statistical analysis of the energy extraction from the geopressured-geothermal reservoirs and render a model for predicting energy recovery from these reservoirs. The study uses

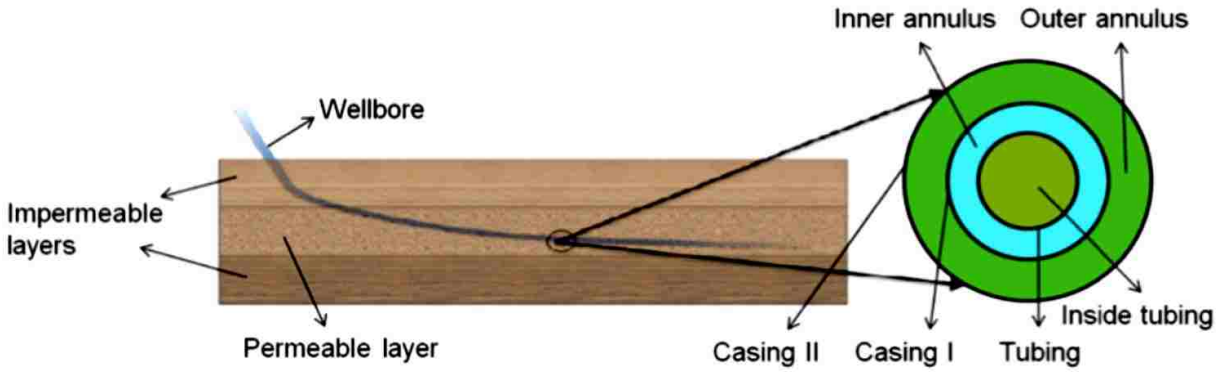

Figure 1.4: Schematic of DHE cross section in the wellbore (from Tyagi and White (2010))

Inspection Analysis (IA), Design of Experiments (DOE) and Response Surface Methods (RSM) for achieving its objective.

Two cases are then selected from the literature. The first case, the Gueydan Dome system (LA), has previously been the subject of research (Gray and Nunn, 2010; Plaksina et al., 2011). The second case, the Sweet Lake area (LA), was originally identified by the Gulf Geothermal Corporation in 1974 and was developed to explore the capability of geothermal energy production in the state of Louisiana (Durham Jr et al., 1981). Conclusions about the maximum heat recovery from these reservoirs using the single power plant design suggest that their temperature map and well flow rates are important factors in their evaluation (Ansari et al., 2014).

1.8 Dissertation layout

This work proceeds as follows. A comprehensive statistical analysis of Gulf Coast geothermal data is performed and uncertainty in the factors is quantified (Chapter 2). Fundamental equations governing a geopressured-geothermal reservoir are presented (Chapter 3 and Appendix A). The energy extraction response to two designs is then studied. First, the regular line drive (Chapters 3, 4 and Appendix B) and second, a zero mass withdrawal design in which horizontal wells are used (Chapters 5, 6 and Appendix C). IA is applied to these equations to obtain the dimensionless numbers which transforms the PDEs into the dimensionless form. Experimental design is applied to these dimensionless numbers to cre-

ate screening models for efficiently evaluating the energy extraction response of reservoirs. The outcome of this research are simple models which predict production temperature and thermal recovery of geopressured geothermal reservoirs.

Chapter 2

Resource characterization

The study in this chapter will be used to create the range of the parameters for the experimental design and response surface models in the next chapters (i.e. Chapters 4 and 6). Permeability, porosity, average reservoir temperature, thickness, areal extent, temperature gradient, reservoir dip angle, injection temperature and well flow rate were the parameters evaluated. These data were transformed using appropriate methods and distributions were fit to the transformed data. An approach for calculating the reservoir dip angle was developed which requires bootstrapping the temperature gradient in the area.

2.1 Available data and limitations

The geothermal data used in the present study is based on the reports published by Bassiouni (1980) and John et al. (1998). The sources contain the data collected in the US Department of Energy "Wells-of-Opportunity" and "Design Wells" programs respectively.

In the "Wells-of-Opportunity" program, the wells were selected from conventional oil and gas well dry holes based on necessary criteria for potentially productive geopressured geothermal aquifers. The program was designed to quickly provide information on the physical and petrophysical characteristics of a large number of reservoirs from a diverse geographic and geologic area without great expense. Such a program has the limitations of not locating wells in structurally favorable locations nor in positions which could provide information on the complete reservoir limits. The program ranked the fifteen most promising geopressured geothermal prospects in Louisiana out of sixty-three prospects that were studied. These fifteen wells are labeled as Source 1. All fifteen wells have reservoir volume and depth information. Permeability, porosity and temperature data were available for only the top five areas (Bassiouni, 1980).

The "Design Well" program was conducted between 1979 and 1990 to provide long term comprehensive information from wells located at targeted reservoir points and designed to produce geopresured brines at high rates from geologically favorable areas (Figure 2.1). The data contain measured temperature, depth, porosity, flow rate, derived permeability and other data (e.g. pressure and salinity) that were not used to prepare the evaluation results in the original work (a working data set has been developed for this work). There were seventeen wells reported for this program, three of which are located in Texas and the rest are located in Louisiana (John et al., 1998). These wells are labeled as Source 2.

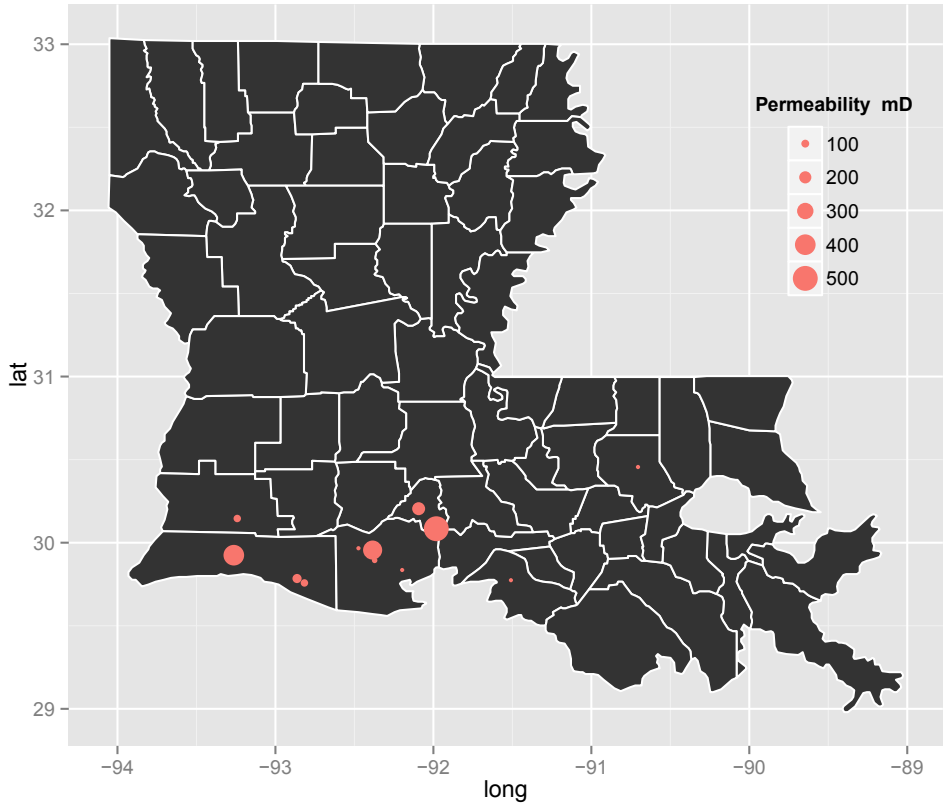

Figure 2.1: Location of source 2 geothermal reservoirs in Louisiana. There are also three reservoirs from Texas which are not shown. Red dots are scaled on permeability which varies between 7 and 500 md.

It is assumed that the data is collected randomly and the two data sources are compared using a statistical t-test and analysis of variance (ANOVA) for any inconsistency. A program developed using the R statistical analysis software package (R Core Team, 2014)

can regenerate the results shown below if or when any new information is added to the working data set. Table 2.1 shows the range and various statistical measures for a selected number of parameters from the data set and Figure 2.2 compares the data sources.

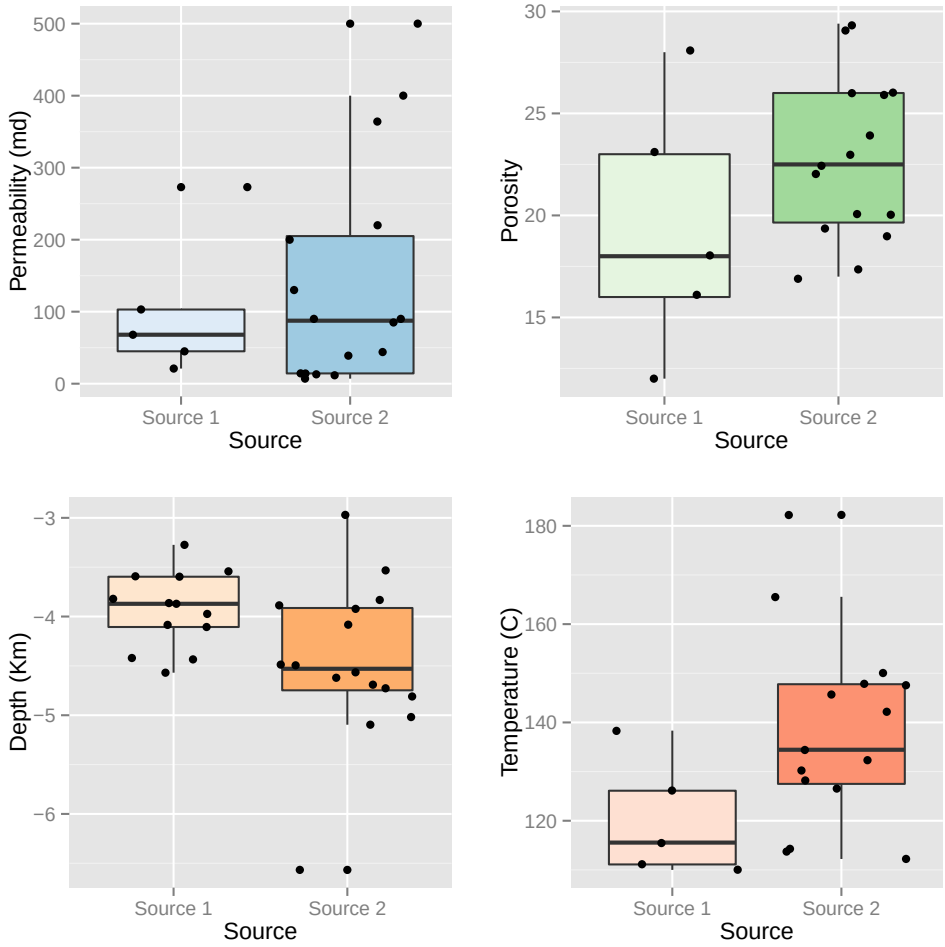

Figure 2.2: Comparing the data sources. Source 1 data is from Bassiouni (1980) and Source 2 data from John et al. (1998). Thick horizontal line shows the median and the thin horizontal lines (the top and bottom of shading areas) show the first and third quartile. Edges of the vertical lines shows the maximum and minimum values excluding the outliers.

A t-test is used to compare permeability, porosity and temperature that come from the two data sources. The result of the t-test on these parameters are shown in Table 2.2. The true difference in the mean permeability and the mean porosity are equal to zero (i.e. p-value > 0.05) which indicates that the permeability and porosity data from the two sources are consistent. The t-test comparing the temperatures from the two sources

Table 2.1: Summary of the available data. Fifteen wells from Source 1 (Bassiouni, 1980) had reservoir volume and depth information. Permeability, porosity and temperature data were available for only the top five areas. Seventeen wells from Source 2 (John et al., 1998) were used.

	permeability (mD)	porosity	temperature (C)	thickness (m)	length (m)
Min.	7	12	100	10	10,180
1st Qu.	21	18	125	83	11,320
Median	85	22	150	114	11,830
Mean	130	21	150	103	12,200
3rd Qu.	200	26	175	137	12,470
Max.	500	29	200	160	15,770

rejects the null hypothesis (p-value < 0.05) indicating that the mean temperatures of the groups are different. This result could be a type one error because the depths at which temperatures are noted in the two sources are different. A two way ANOVA is more appropriate for making final conclusions about temperature. The two way ANOVA test for the temperature is shown in Table 2.3.

Table 2.2: Results from the t test for permeability, porosity and temperature. Null hypothesis is not rejected for permeability and porosity showing consistency in the reports.

	df	t	p value
Permeability	10.74	-0.62	0.55
Porosity	5.13	-1.11	0.31
Temperature	11.54	-2.46	0.03

Table 2.3: Results from the two way ANOVA on the temperature. The difference in the temperature is caused by the depth.

	Df	Sum Sq	Mean Sq	F value	Pr(>F)
Depth	1	5,185.29	5,185.29	51.83	0
Source	1	146.12	146.12	1.46	0.2444
Depth:Source	1	111.92	111.92	1.12	0.3059
Residuals	16	1,600.56	100.04		

The effect of having different mean temperatures is due to the depth (p-value < 0.05) and not the source confirming the consistency between the sources. Failing to reject the null hypothesis for permeability, porosity and temperature also provides some preliminary basis to suggest that the hot saline aquifers of the Louisiana have gone through similar depositional and diagenetic histories.

2.2 Permeability

The geological processes that create and destroy permeability in conventional reservoir rocks appear to leave permeability distributed around the geometric mean (log normal distribution, White (2013)). The permeability is available for most of the wells (Figure 2.3). A normal distribution was then fit to the natural-log transformed permeability (Table 2.4, Figure 2.4).

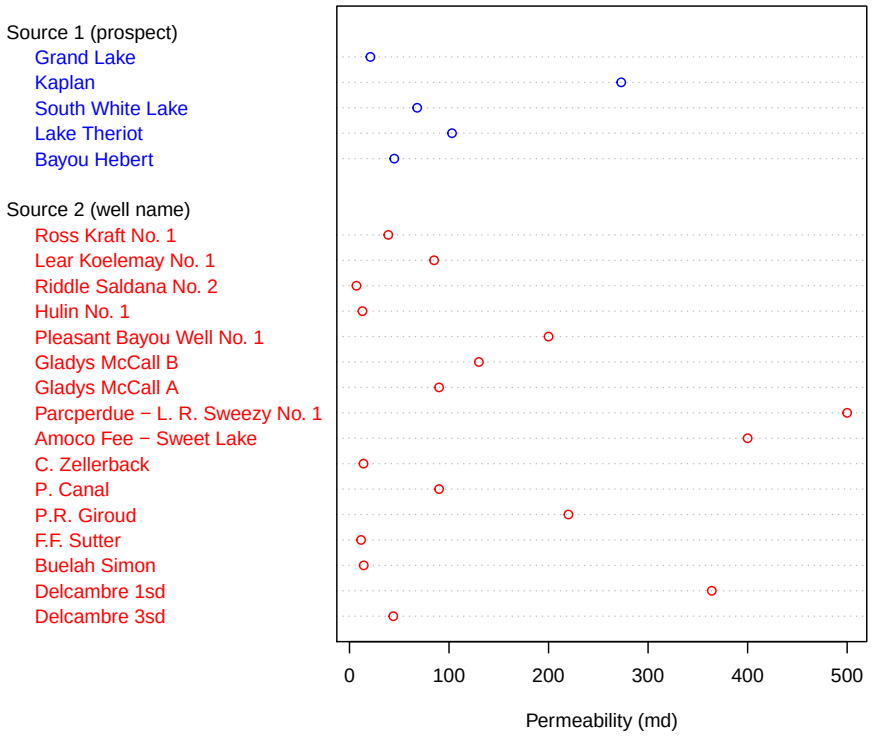

Figure 2.3: Wells with reported permeability. Source 1 data from Bassiouni (1980) and Source 2 data from John et al. (1998).

Table 2.4: Summary of the normal fit to the natural-log transformed permeability

	permeability (mD)
log-mean	4.20
log-sd	1.26

2.3 Porosity, thickness, length and temperature

The main underlying assumption of this section is that the samples represent all geothermal reservoirs in Louisiana. Porosity, thickness, areal extent (represented by "length"

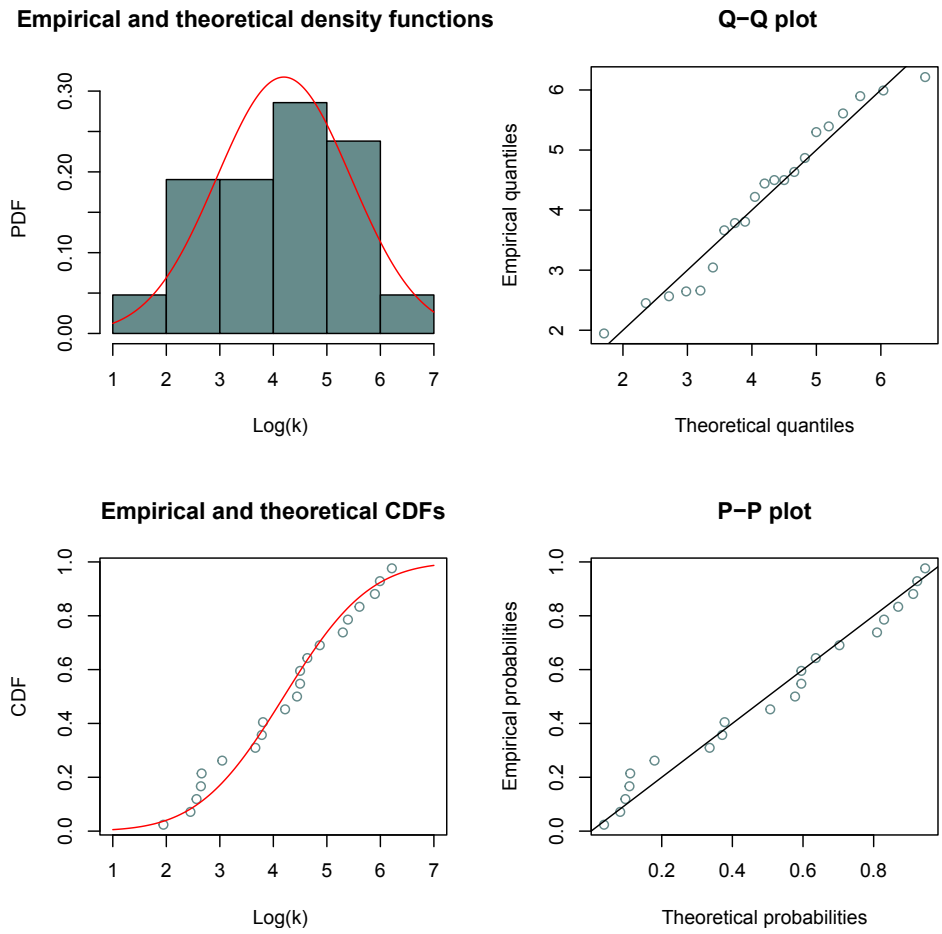

Figure 2.4: Fitting a normal distribution to the log transformed permeability.

where the length is the square root of the area) and temperature data (Figure 2.5) were transformed using a normal score transform (Figure 2.6) and a normal distribution was fit to the transformed data (Figure 2.7). Fitted Distributions are summarized in Table 2.5.

2.4 Geothermal gradient

The geothermal gradient appears in the dimensionless numbers (see Chapter 3 and Appendix A). The mean geothermal graident varies from less than 15 °C/km to more than 50 °C/km depending on environment. Depending on the lithology, this variation can be up to a factor of 5 or more in a single well (Tester et al., 2006). Gray and Nunn (2010) studied the geothermal gradient for the wells in the Gueydan Dome area and concluded that sediments shallower than 3,900 m have an average thermal gradient of 23 °C/km. They

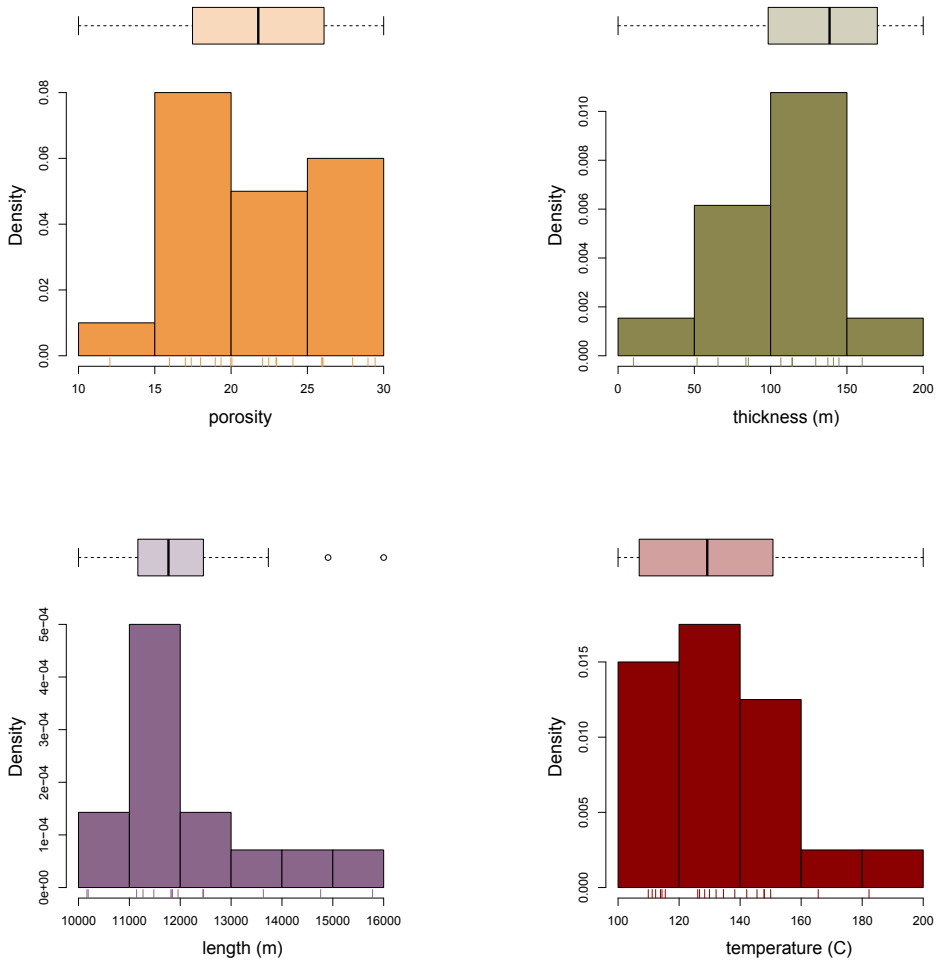

Figure 2.5: Parameter distributions before transformation (data from Bassiouni (1980)and John et al. (1998)). Data values are shown below the histogram as tiny lines and the box plot shows the quantiles of each parameter. The most likely value for the reservoir thickness and length lies between 100-150 m and 11,000-12,000 m respectively. The most likely value for the porosity and temperature are between 15-20 and 120-140 °C, respectively.

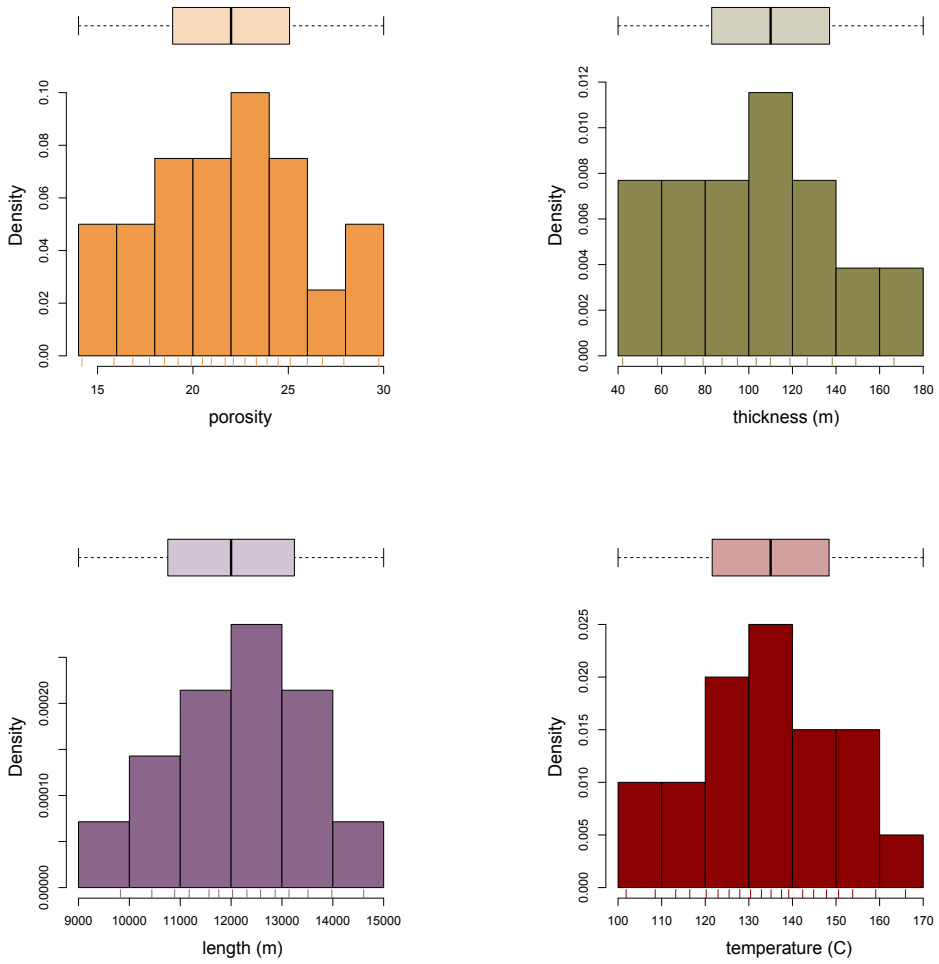

Figure 2.6: Normalized parameter distributions using normal score transform

suggest a geothermal gradient of 28.9 °C/km from depths between 3,900 to 5,000 m based on the well temperature data and attributed the variation to geopressured layers formed by rapid sedimentation. Average geothermal gradient is around 25 °C/km in most of the world (Fridleifsson et al., 2008) which is close to the average value for the sedimentary sections seen in this study. Depth and temperature data from the wells were used to estimate the geothermal gradient (i.e. regression coefficient, Figure 2.8). To establish a confidence interval for the calculated geothermal gradient (τ) without assuming any underlying theoretical distribution, a repeated random sampling with replacement (bootstrapping) is performed (Figure 2.9, White (2013)).

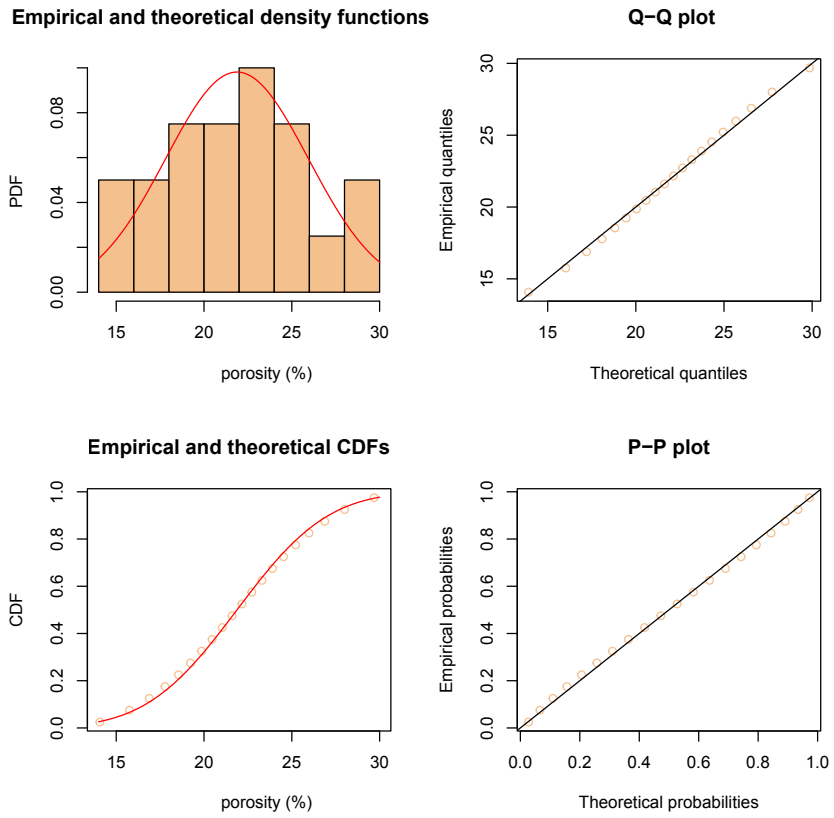

Figure 2.7: Gaussian distribution fit to the normalized porosity. As expected, both Q-Q and the CDF plot indicate good fit.

Table 2.5: Summary of the Gaussian fit to the normal score transformation of the porosity, thickness, length and temperature data

	porosity	thickness (m)	length (m)	temperature (C)
mean	21.88	103.42	12,198.87	133.72
sd	4.07	35.18	1,317.48	16.73

2.5 Reservoir dip angle

According to Gray and Nunn (2010), the range of the dip angle for the Camerina A reservoir is from 1.2° to 28°. Calculating the reservoir dip angle by investigating the gradient of structural maps is challenging. Further, for the purpose of this work, it is the average reservoir dip angle that is of interest to characterize geothermal systems and not the local dip angle. The average reservoir dip angle is found by recognizing that the temperature of the Louisiana's geopressured-geothermal reservoirs would remain lower than T_{max} (an arbitrary variable) and by using reservoir temperature gradient, average

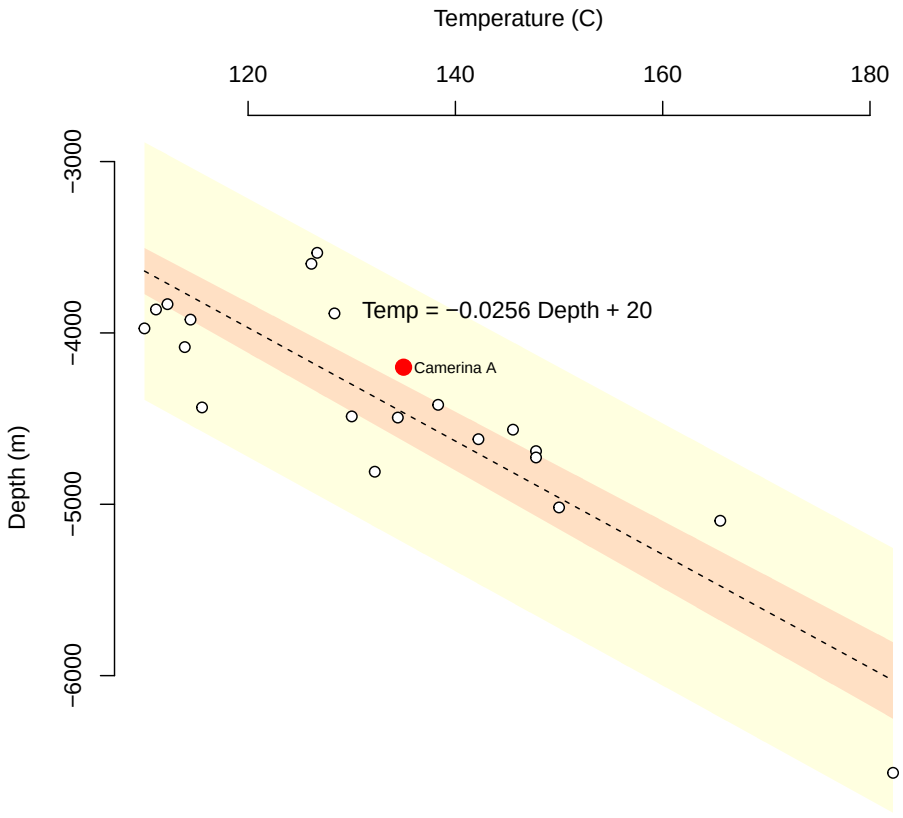

Figure 2.8: The dark tan region shows 95% confidence interval band around the predicted mean for the temperature of the geothermal reservoirs in Louisiana at each depth. Average geothermal gradient is around 25 °C/km in most areas (Fridleifsson et al., 2008) and the average value estimated here turned out to be very close. The light tan shows the 95% confidence interval for the mean of any random sample. The Camerina A reservoir is used to test the model and the model seems to be acceptable. Source code is modified from White (2013).

temperature and its size. Since no a priori information is contained in the dataset about where the average reservoir or bottomhole temperature was located, it was assumed that the data are sampled uniformly along the reservoir assigning the average reservoir temperature to (L/2,H/2). Available data can then be used to calculate this T_{max} using Eq. 2.1:

$$\alpha = \sin^{-1}\left(\frac{2(T_{max} - T_{avg})}{\tau L}\right) \tag{2.1}$$

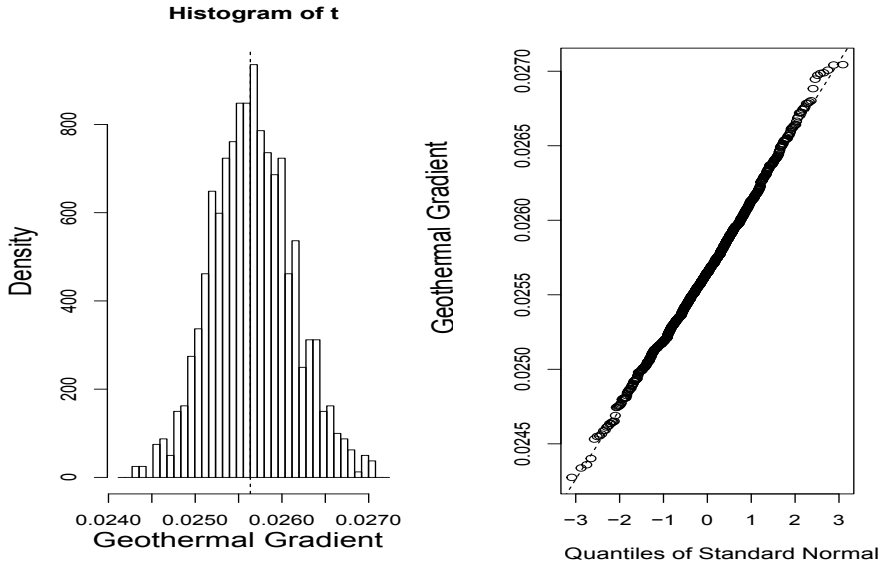

Figure 2.9: Bootstrapped geothermal gradient for hot saline aquifers of Louisiana. The value calculated for the mode is the same as the slope of the previous figure. The average geothermal gradient changes in the range 0.024-0.027 $^{\circ}C/km$.

in which:

$$\tau \sim \mathcal{N}(\mu_\tau, \sigma_\tau^2) \tag{2.2}$$

$$T_{avg} \sim \mathcal{N}(\mu_T, \sigma_T^2) \tag{2.3}$$

$$L \sim \mathcal{N}(\mu_L, \sigma_L^2) \tag{2.4}$$

$$T_{max} = ? \tag{2.5}$$

The symbol $\mathcal{N}$ in these equations represents normal distribution with mean μ and variance σ^2. Knowing that the dip angle of Eq. 2.1 cannot be more than 90 degrees, the fraction in Eq. 2.1 can be constrained to its maximum (i.e. one) which means:

$$\frac{2(T_{max} - T_{avg})}{\tau L} \leq 1 \tag{2.6}$$

$$T_{max} \leq T_{avg} + \frac{\tau L}{2} \tag{2.7}$$

$$T_{max} = (\mu_T - 3\sigma_T) + \frac{(\mu_\tau - 3\sigma_\tau)(\mu_L - 3\sigma_L)}{2} \tag{2.8}$$

T_{max} was found to be ca. 183 $°C$ and Eq. 2.1 can be solved using a sampling method (Kroese et al., 2011). A Hammersley Sequence Sampling was used to sample average temperature, geothermal gradient and reservoir length for finding the dip angle of the layers (Figure 2.10). The median of the dip angle is ca. 15° and if outliers are excluded (i.e. it is unlikely to have a reservoir with the dip angle of more than 60°) then the lower quartile is ca. 2.5° and the upper quartile is ca. 25°.

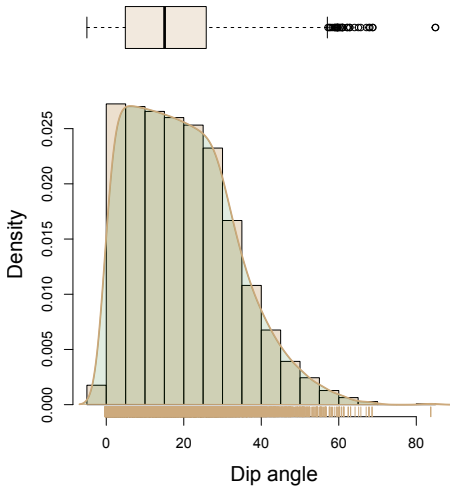

Figure 2.10: Modeled dip angle distribution for Gulf Coast geothermal reservoirs. The median of the dip angle is ca. 15° and if we exclude the outliers (i.e. it is unlikely to have a reservoir with the dip angle of more than ca. 60°) then the lower quartile is ca. 2.5° and the upper quartile is ca. 25°.

2.6 Injection temperature

Injection temperature reduces the temperature of the reservoir. In binary power plants, the discharge temperature varies between 25 and 90 °C (Tester et al., 2006). Average annual surface temperature for Louisiana is ca. 20 °C (www.ncdc.noaa.gov); so it is more likely that the injection temperature further cools down to this temperature. Though the range of injection temperature is known, no a priori knowledge of the distribution form is available.

For downhole heat exchangers (DHEs), the injection temperature will be a function of the length of the production section, the length of the injection section, the distance between

the injection and production sections, the input temperature and other factors such as the specifics of the working fluid, casing and tubing diameters, etc. A DHE with working fluid injected through the tubing and brine passing the casing is known as WFT (working fluid through tubing) which has higher efficiency compared with other designs. The proposed total length of the DHE varies between ca. 150 and 300 m which makes the injection temperature varying from ca. 120 down to 40 °C respectively for an input temperature of ca. 150 °C, and flow rate of ca. 400 $m^3.day^{-1}$, assuming engineering assumptions for other parameters (Feng, 2012). A uniform distribution is assumed for DHE's injection temperature because no a priori knowledge is available.

2.7 Flow Rate

Flow rate is also an important parameter, on which rate of power generation directly depends. The reported flow rate values appear to be constrained by tubing size meaning the reservoir could sustain higher rates. In fact researchers became aware of Gulf Coast geopressured aquifers for their geohydraulic potential rather than their geothermal energy (Hawkins, 1977). McMullan and Bassiouni (1984) realized that maximizing flow-rate maximizes Net Present Value (NPV) in geopressured geothermal reservoirs and showed that the effect of tubing size and skin overwhelms other effects such as well location with respect to aquifers. Their study indicates that these reservoirs can sustain rates higher than 6,350 $m^3.day^{-1}$ (40,000 $bbl.day^{-1}$) and may exceed 17,500 $m^3.day^{-1}$ (110,000 $bbl.day^{-1}$) for up to 5 years. The well test data shows a flow rate range between ca. 250 to 4,250 $m^3.day^{-1}$ (Figure 2.11). A uniform distribution is assumed for flow rate because there is no priori knowledge of the distribution. Based on the current data, it was assumed that the variable should not take values higher than the largest value from the well test records.

Previous DHE designs have a single point fluid inlet and a single point outlet for the geofluid and these are independent of the reservoir (Feng, 2012). However, new designs are evolving into having a length for the production completion and a length for the injection completion to minimize the pressure drop through the completions to minimize sand

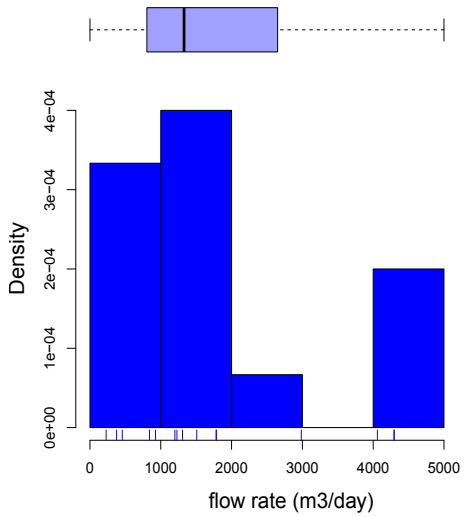

Figure 2.11: Well test data for flow rate (data from John et al. (1998)).

production or due to pump capacities. If the heat exchange occurs between the two completions, this means that the DHE is no longer isolated from the reservoir and flow rates may be lower than conventional heat exchangers (ca. 450 $m^3.day^{-1}$ or 5.25 $kg.s^{-1}$, Feng (2012), Akhmadullin and Tyagi (2014)).

This chapter discussed the typical range of parameters for a geopressured-geothermal reservoir. In the next chapter, a line drive pattern similar to what has been done in the waterflooding will be used to evaluate energy extraction response from geopressured-geothermal reservoirs.

Chapter 3

Regular line drive

In this chapter, the governing equations describing a line drive system (Figure 3.1) are derived from the fundamental partial differential equations for a geothermal system (Appendix A), because the line drive system has been used in studies such as waterflooding and CO_2 flooding (Shook et al., 1992; Wood et al., 2008). Regular design means injecting cooler water at the up-dip side of the reservoir and producing hot geofluid from the down-dip portion of the reservoir (Plaksina et al., 2011). Regular design is selected because producing from the hotter and injecting into the cooler sections of the reservoir recovers more heat (Ansari et al., 2014). Inspectional analysis is used to obtain the dimensionless groups for this design (see Appendix B). Then, these dimensionless groups are explained.

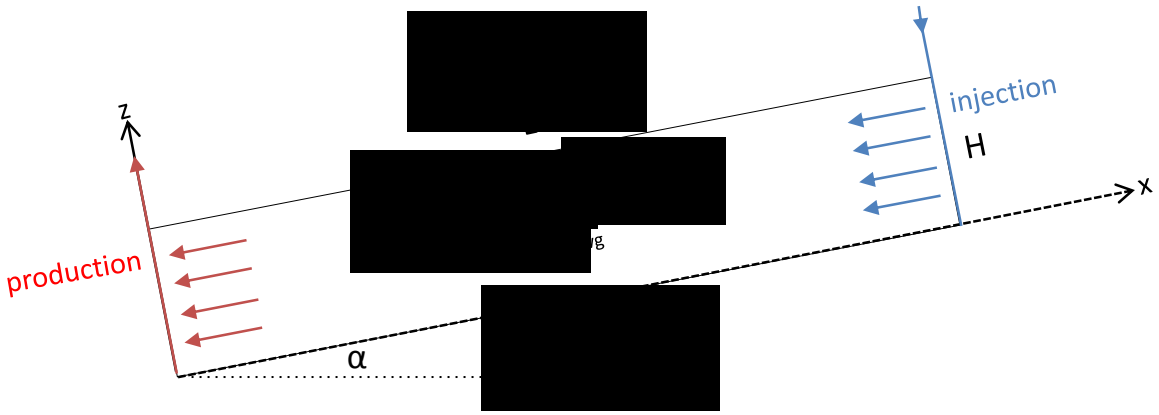

Figure 3.1: Regular heat extraction design. Similar design is used in studies such as waterflooding and CO_2 flooding (Shook et al., 1992; Wood et al., 2008).

3.1 Regular design model

- Continuity equation

For the system shown in Figure 3.1, the general continuity equation for single phase flow in porous media reduces to Eq. 3.1 (see Eq. A.12 in Appendix A).

$$\phi(c_t\frac{\partial p}{\partial t}-\beta_t\frac{\partial T}{\partial t})+u_x(c_f\frac{\partial p}{\partial x}-\beta_f\frac{\partial T}{\partial x})+u_z(c_f\frac{\partial p}{\partial z}-\beta_f\frac{\partial T}{\partial z})+\frac{\partial u_x}{\partial x}+\frac{\partial u_z}{\partial z}=0 \tag{3.1}$$

- Darcy equation

For writing the Darcy equation along the new coordinates, the gravity vector follows along the x and z axes.

$$u_x=-k_x(\frac{\partial p}{\partial x}-\rho g\sin\alpha) \tag{3.2}$$

$$u_z=-k_z(\frac{\partial p}{\partial z}-\rho g\cos\alpha) \tag{3.3}$$

- Energy equation

The energy equation (see Appendix A) can be written for two-dimensions as:

$$M\frac{\partial T}{\partial t}+u_x\frac{\partial T}{\partial x}+u_z\frac{\partial T}{\partial z}-T\phi(c_t\frac{\partial p}{\partial t}-\beta_t\frac{\partial T}{\partial t})-\kappa(\frac{\partial^2 T}{\partial x^2}+\frac{\partial^2 T}{\partial z^2})=0 \tag{3.4}$$

- Reservoir boundary condition

For the overburden and underburden heat conduction, Eqs. A.18 and A.19 yield Eqs. 3.5 and 3.6, in which $\kappa'_{ob}=\lambda_{ob}/(\rho_{ob}C_{p,ob})$ and $\kappa'_{ub}=\lambda_{ub}/(\rho_{ub}C_{p,ub})$. Overburden and underburden layers are assumed impermeable, thus there is no flow across them (Eqs. 3.7-3.8). The length of reservoir is larger than it's thickness and it can be assumed that there is no heat conduction across the model laterals (Eqs. 3.9-3.10).

$$\frac{\partial T}{\partial t}=\kappa'_{ob}(\frac{\partial^2 T}{\partial x^2}+\frac{\partial^2 T}{\partial z^2}) \tag{3.5}$$

$$\frac{\partial T}{\partial t}=\kappa'_{ub}(\frac{\partial^2 T}{\partial x^2}+\frac{\partial^2 T}{\partial z^2}) \tag{3.6}$$

$$u_z = 0 \qquad at\ z = 0, \forall x, t \tag{3.7}$$

$$u_z = 0 \qquad at\ z = H, \forall x, t \tag{3.8}$$

$$\frac{\partial T}{\partial x} = 0 \qquad At\ x = 0, \forall z, t \tag{3.9}$$

$$\frac{\partial T}{\partial x} = 0 \qquad At\ x = L, \forall\ z, t \tag{3.10}$$

T_{avg} indicates the average temperature of the reservoir. This temperature can be calculated by performing temperature buildup tests on the wells or using statistical methods (Grant, 2013). Well temperature and average reservoir temperature have been reported in the legacy data (John et al., 1998; Bassiouni, 1980). Temperature gradient normal to the ground (i.e. $\tau = \frac{\partial T}{\partial Z}$) can also be calculated using well data. Geothermal gradient increases linearly with depth (within a zone), thus average reservoir temperature (T_{avg}) is assigned to the middle of the reservoir. Rotating similarly sized models around the middle point yields almost equal energy density (total energy in place divided by the total reservoir volume) regardless of the dip angle, geothermal gradient, length, width or thickness (see Novakovic (2002)).

$$T_{ub,t=0} = T_{avg} + \frac{H}{2}(\tau \cos\alpha) + (\tau \sin\alpha)(\frac{L}{2} - x) \qquad At\ z = 0, t = 0, \forall x \tag{3.11}$$

$$T_{ob,t=0} = T_{avg} - \frac{H}{2}(\tau \cos\alpha) + (\tau \sin\alpha)(\frac{L}{2} - x) \qquad At\ z = H, t = 0, \forall x \tag{3.12}$$

$$T_{ob,z=\infty} = T_{ob,t=0} \qquad At\ z = \infty, \forall x, t \tag{3.13}$$

$$T_{ub,z=-\infty} = T_{ub,t=0} \qquad At\ z = -\infty, \forall x, t \tag{3.14}$$

In practice, a semi-analytical thermal boundary condition is used for numerically modeling Eqs. 3.5 and 3.6 (Vinsome and Westerveld, 1980). For applying IA to the boundary heat gain/loss process, only a description of the boundary condition at the interface is

important. The tail of the temperature distribution does not transfer energy to the system (Vinsome and Westerveld, 1980). Thus having $z = \pm\infty$ in Eqs. 3.13 and 3.14 does not affect the inspectional analysis. Boundary equations 3.11 and 3.12 do not provide additional information about the system because the initial condition of the reservoir contains this information so Eqs. 3.11, 3.12, 3.13 and 3.14 can be ignored, only addressing Eqs. 3.5 and 3.6.

- Injection

  For the injection completion, the boundary conditions are:

$$u_x = -u_T \quad At\ x = L, \forall z, \forall t \tag{3.15}$$

$$T = T_{inj} \quad At\ x = L, \forall z, \forall t \tag{3.16}$$

$$q_{inj} = \int_0^H u_T W\, dz = -q_{prod} \tag{3.17}$$

in which W is reservoir's width. The sign of u_T is the same for both injection and production but the sign of q differs. A negative sign for u_T is chosen because the velocity vector is in the $-x$ direction.

- Production

  For the production completion, the boundary conditions are:

$$u_x = -u_T \quad At\ x = 0, \forall z, \forall t \tag{3.18}$$

$$q_{prod} = -\int_0^H u_T W\, dz \tag{3.19}$$

- Initial conditions

  The initial conditions for the system are:

$$p = p_i \qquad At\ t = 0, \forall x, z \tag{3.20}$$

$$T = T_{avg} + (\tau \cos\alpha)(\frac{H}{2} - z) + (\tau \sin\alpha)(\frac{L}{2} - x) \qquad At\ t = 0, \forall x, z \tag{3.21}$$

3.2 Dimensionless groups

The dimensionless groups using inspectional analysis (Appendix B) are:

$$\pi_1 = \frac{\phi c_t}{c_f} \qquad \pi_2 = \frac{\phi \beta_t}{\beta_f}$$

$$\pi_3 = M = \frac{\rho_m C_{pm}}{\rho_f C_{pf}} \qquad \pi_4 = c_f p_1^* = \frac{c_f \mu q L}{k_x W H}$$

$$\pi_5 = \beta_f T_1^* = \beta_f T_{avg} \qquad \pi_6 = R_L = \frac{L}{H}\sqrt{\frac{k_z}{k_x}}$$

$$\pi_7 = \frac{L}{H}\tan\alpha \qquad \pi_8 = \frac{L}{H}$$

$$\pi_9 = N_\alpha = \frac{k_x \rho_f\, g \sin\alpha\, W H}{q\mu} \qquad \pi_{10} = Pe = \frac{u_T H}{\kappa} = \frac{q}{\kappa W}$$

$$\pi_{11} = \frac{\kappa'_{ob}}{\kappa} \qquad \pi_{12} = \frac{\kappa'_{ub}}{\kappa}$$

$$\pi_{13} = c_f p_i \qquad \pi_{14} = \frac{T_{inj}}{T_{avg}}$$

$$\pi_{15} = \frac{\tau \sin\alpha\, L}{T_{avg}}$$

Because the focus of the study is to model thermal recovery factor and production temperature, the energy equation is used for scaling the time (Appendix B). The dimensionless time for this system is then:

$$t_D = \frac{1}{M}\frac{qt}{LWH} \tag{3.22}$$

in which $M = (\rho_m C_{pm})/(\rho_f C_{pf})$. Note that if the dimensionless time was defined based on the momentum equation, it would be $t_{D_{hyd}} = \frac{\phi C_f}{C_t}\frac{qt}{LWH}$.

All of these dimensionless groups are needed for transforming the dimensional model into dimensionless representation; however, their form can be heuristically manipulated (multiplied or divided) to get other desirable dimensionless groups.

3.3 Explaining dimensionless groups

Five dimensionless groups are identical to those published by previous researchers. They are: π_3 representing matrix to fluid heat capacity ratio (Phillips, 2009), π_6 representing an effective aspect ratio (Shook et al., 1992; Wood et al., 2008), π_7 representing a dip angle group (Shook et al., 1992; Wood et al., 2008), $\frac{\pi_4\pi_9\pi_{15}}{\pi_7}$ representing the Buoyancy number (Shook et al., 1992; Wood et al., 2008) and π_{10} representing the thermal Peclet number (Phillips, 2009).

The meaning of other dimensionless groups can be discerned from their derivation or their format: π_1 is the ratio of total compressibility to fluid compressibility, π_2 is the ratio of total expansivity to fluid expansivity and π_5 is fluid expansion due to average reservoir temperature. The π_{11} and π_{12} terms show the ratio of heat conduction across the boundary to heat conduction within the reservoir. The π_{13} term describes fluid compression as a result of reservoir pressure. The π_{14} term scales the injection temperature to the average reservoir temperature and π_{15} scales the temperature difference across the reservoir to the average reservoir temperature and represents the temperature distribution in the reservoir.

3.3.1 Effective aspect ratio

$$\pi_6 = R_L = \frac{L}{H}\sqrt{\frac{k_z}{k_x}} \tag{3.23}$$

The effective aspect ratio controls the cross flow within the reservoir and indicates the ratio of the rate of communication between the fluids in the horizontal direction to the rate of communication between the fluids in the vertical direction. This number is purely a reservoir characteristic showing anisotropy and has been reported for reservoir water-flooding, CO_2 injection, surfactant-polymer as well as surfactant enhanced CO_2 flooding.

(Shook et al., 1992; Novakovic, 2002; Rai, 2008; Wood et al., 2008; Afonja, 2013). Smaller aspect ratios mean that the fluid communication in the horizontal direction is more than the fluid communication along the vertical direction. Novakovic (2002) gives several other interpretations for effective aspect ratio. For homogeneous and isotropic reservoirs, effective aspect ratio reduces to the aspect ratio; thus this ratio can be seen as a heterogeneity scaled aspect ratio. This number can also be interpreted as relative flow capacity of the reservoir in the vertical and horizontal directions (Novakovic, 2002).

3.3.2 Dip angle group

$$\pi_7 = N_\alpha = \frac{L}{H}\tan\alpha \tag{3.24}$$

This dimensionless number has no fluid or rock property and is an entirely geometrical parameter. It has been noted in water and CO_2 injection scenarios (Shook et al., 1992; Wood et al., 2008). This number is also known as the tilt number and interpreted as the measure of the rotation of the system. If this number is multiplied by another dimensionless group, it transforms the dimensionless group from a horizontal-vertical system to a longitudinal-transverse system accounting for the tilt (Novakovic, 2002).

3.3.3 Buoyancy number

$$\begin{aligned} N_g &= \frac{\pi_4\pi_9\pi_{15}}{\pi_7} = \frac{k_x(\beta_f\tau\sin\alpha L\rho_f)g\sin\alpha}{u_T\mu}\frac{H\cos\alpha}{L\sin\alpha} \\ &= \frac{k_x(\beta_f\,\rho_f\Delta T)g\cos\alpha\,H}{u_T\mu L} = \frac{k_x\Delta\rho g\cos\alpha\,WH^2}{q\mu L} \end{aligned} \tag{3.25}$$

Buoyancy number has also been published by previous authors (Shook et al., 1992; Novakovic, 2002; Wood et al., 2008; Rai, 2008; Afonja, 2013). The buoyancy number is the ratio of the gravity forces to the viscous forces and is sometimes called gravity number. In petroleum engineering, the density difference between injection and production fluid

creates this number. In geothermal reservoirs, the difference in the temperature of the geofluid across the reservoir creates density differences in the fluid (Eq. 3.25).

3.3.4 Thermal Peclet Number

$$\pi_{10} = Pe = \frac{u_T H}{\kappa} = \frac{q}{\kappa W} \tag{3.26}$$

The Thermal Peclet number is the ratio of the rate of heat advection to the rate of heat diffusion in the porous media (Phillips, 2009). In aquifers with higher thickness and higher flow velocity (e.g. higher permeability), heat convection overwhelms heat diffusion and thermal Peclet number is large. When the aquifer thickness is small compared with its width, thermal Peclet number is also small and heat only transfers by conduction (Phillips, 2009). A decrease in thermal diffusion also increases thermal Peclet number.

3.3.5 Thermal diffusivity ratio

These numbers show the ratio of the conductive heat transfer across the boundary to the conductive heat transfer in the aquifer. These numbers are purely material characteristics. The higher the thermal diffusivity ratio, the greater the heat transfer across the reservoir and the higher thermal recovery.

$$\pi_{11} = (N_{th})_{ob} = \frac{\kappa'_{ob}}{\kappa} \tag{3.27}$$

$$\pi_{12} = (N_{th})_{ub} = \frac{\kappa'_{ub}}{\kappa} \tag{3.28}$$

3.3.6 Temperature ratio

$$\pi_{14} = \frac{T_{inj}}{T_{avg}} \tag{3.29}$$

This number is the ratio of injected energy (corresponding to the injection temperature) to the total energy in place. These numbers are operational and are set by the heat exchanger

design. Temperature ratio inversely affects thermal recovery. If the injection temperature is high, this temperature ratio will also be high. The larger this number, the lower or slower the energy recovery from the reservoir.

3.3.7 Temperature distribution

$$\pi_{15} = \frac{\tau \sin\alpha \, L}{T_{avg}} \tag{3.30}$$

Geothermal gradient creates temperature distributions in the reservoir. Because reservoir length is typically more than its thickness, π_{15} considers temperature differences across the reservoir length. The tilt number (i.e. dip angle number) can be used for rotating this number (π_{15}/N_α) to account for the temperature distribution along the thickness of the reservoir.

3.3.8 Rock and fluid numbers

$$\begin{aligned} \pi_1 &= \frac{\phi c_t}{c_f} & \pi_2 &= \frac{\phi \beta_t}{\beta_f} \\ \pi_3 &= M & \pi_5 &= \beta_f T_1^* = \beta_f T_{avg} \\ \pi_{13} &= c_f p_i \end{aligned} \tag{3.31}$$

All of the 3.31 numbers consist of rock and fluid characteristics. For this work, available tables are used for obtaining the range in which the fluid properties change. In the above dimensionless numbers, $M = (\rho_m C_{pm})/(\rho_f C_{pf})$ is the matrix/fluid thermal capacity and $\rho_m C_{pm} = \phi \rho_f C_{pf} + (1-\phi)\rho_r C_{pr}$.

3.4 Fluid properties

The software package *REFPROP* (Lemmon et al., 2007) is used for obtaining water (pure H_2O) thermodynamic properties . The output tables are interpolated linearly. These

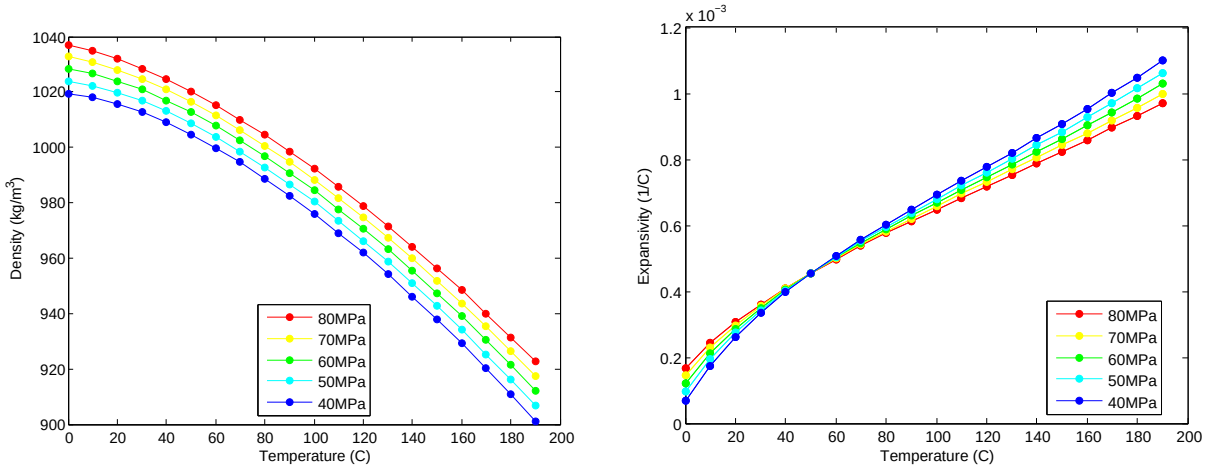

Figure 3.2: Water density (left) and thermal expansivity (right).

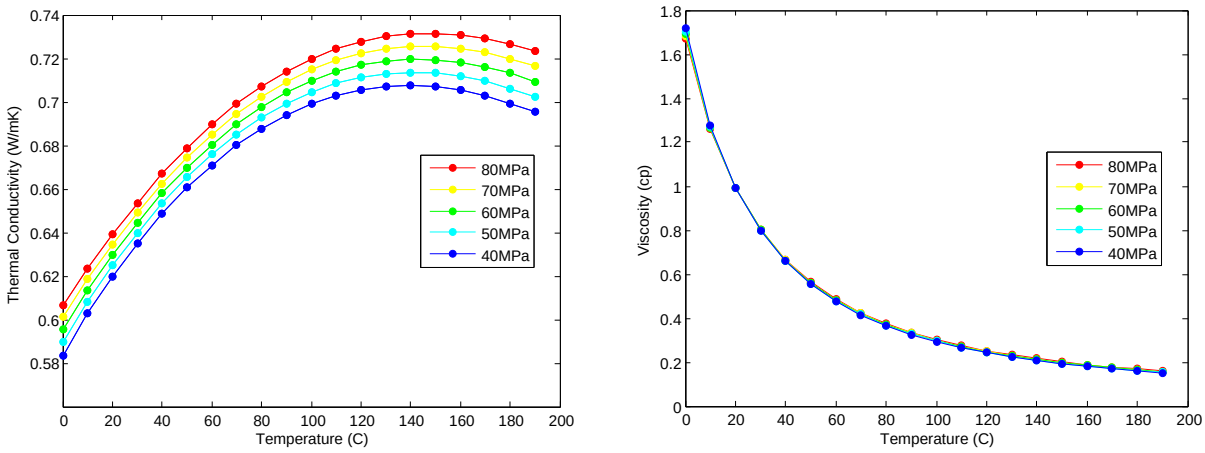

Figure 3.3: Water thermal conductivity (left) and viscosity (right)

properties include density and thermal expansivity (Figure 3.2), thermal conductivity and viscosity (Figure 3.3) and compressibility (Figure 3.4).

3.5 Numerical modeling

Figure 3.5 shows a typical two-dimensional line drive model. The model has $25 \times 1 \times 10$ grid blocks with each grid block being $120\,m \times 100\,m \times 10.5\,m$ in the x, y and z directions, respectively. The number of grid blocks are always fixed and gird sizes are calculated based on the distance between wells (this distance is varied in the next chapters and the case presented here is the bases case). The reservoir has a dip angle of 5° with an average reservoir temperature of $115\,^\circ C$ assigned to the middle of the reservoir. Thermal gradient

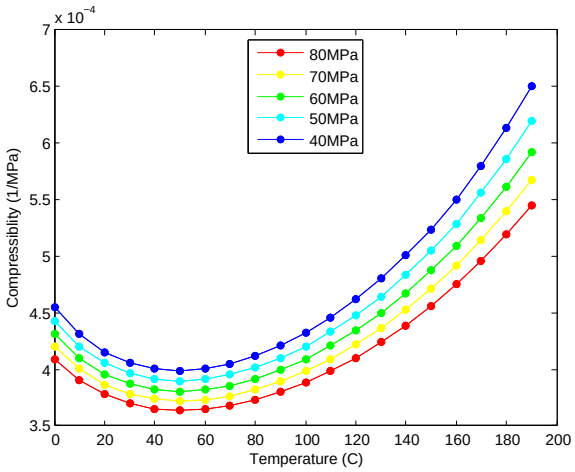

Figure 3.4: Water compressibility.

is $24\,°C/km$. The injection temperature is 30 $°C$ and the injection and production rates are $1,250\,m^3/day$. The reservoir rock cools down as the front slowly propagates in the reservoir and moves towards the production well. Figure 3.6 shows the thermal front at $t_D = 0.2$ (8.5 years) when no breakthrough has occurred. Thermal breakthrough happens around $t_D = 0.6$ (ca. 25 years, Figure 3.7). Figures 3.8 and 3.9 show reservoir temperature at $t_D = 1$ (41.5 years) and $t_D = 3$ (124 years) respectively.

At the start of the simulation, the temperature drop in the production well is due to the geothermal gradient in the model. When breakthrough happens, there is a sharp decrease in the production temperature and finally at late times, the model temperature asymptotically approaches the injection temperature. This numerical model is used in the next chapter to develop a predictive model for dimensionless production temperature and thermal recovery factor.

In this chapter, the dimensionless numbers for a line drive system were derived and explained. In the next chapter, these dimensionless numbers will be used to create response models for evaluating energy extraction from geopressured-geothermal reservoirs developed using a line drive pattern.

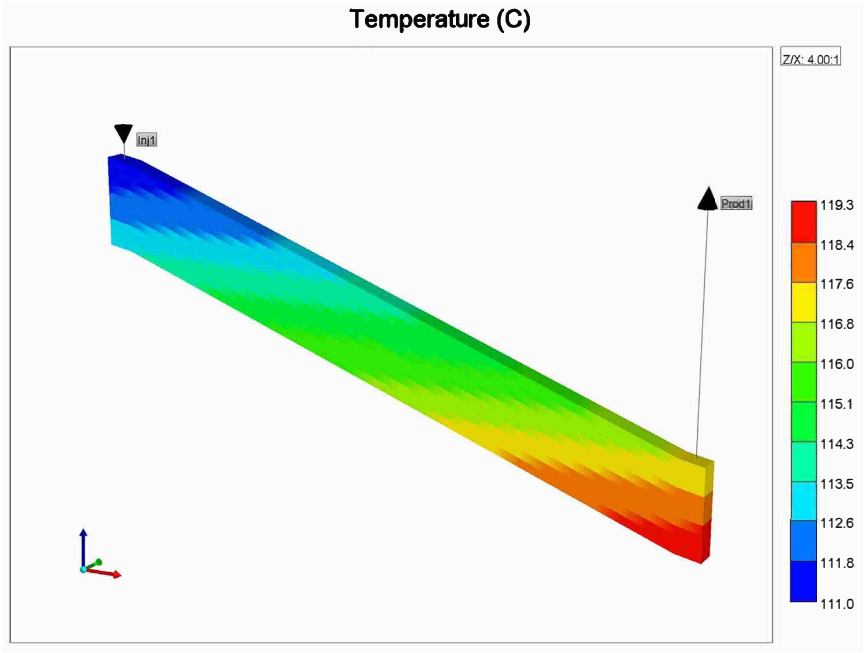

Figure 3.5: Reservoir temperature at initial condition ($t_D = 0$) with an average temperature of 115 $°C$ assigned to the middle of the reservoir. Temperature gradient is 24 $°C/m$ and dip angle is 5°. Vertical axis is exaggerated four times.

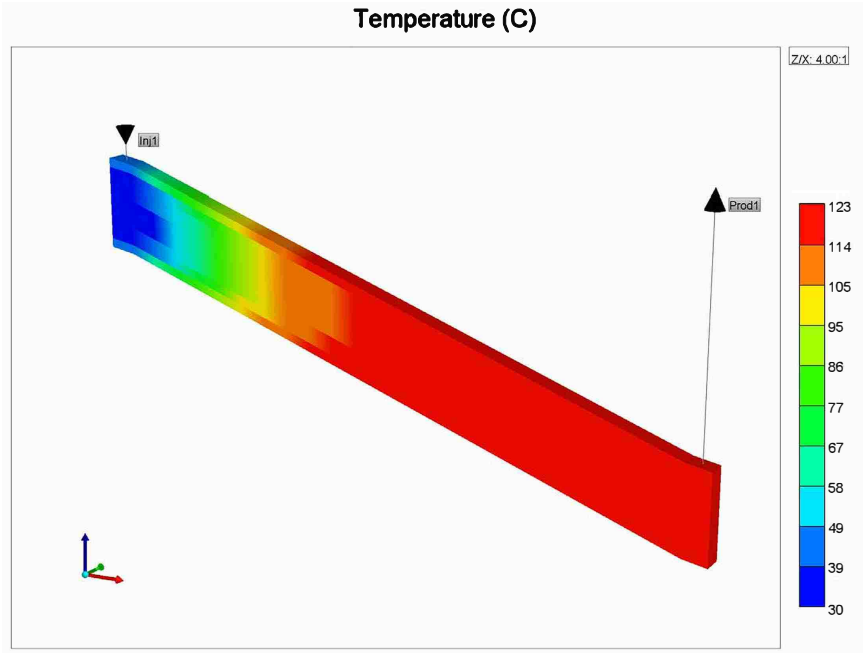

Figure 3.6: Thermal front at $t_D = 0.2$ (ca. 8.3 years). Vertical axis is exaggerated four times.

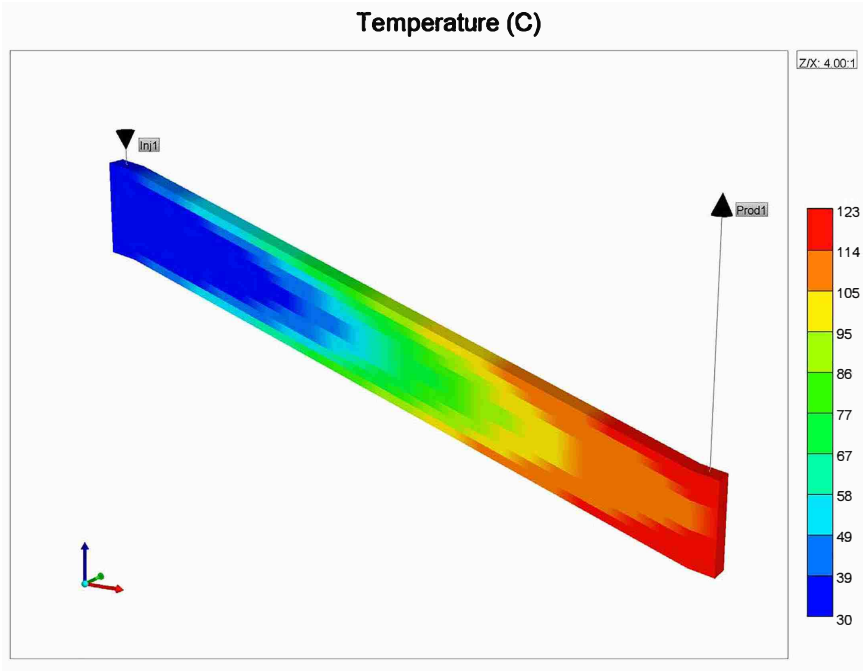

Figure 3.7: Thermal front at breakthrough $t_D = 0.6$ (ca. 25 years). Vertical axis is exaggerated four times.

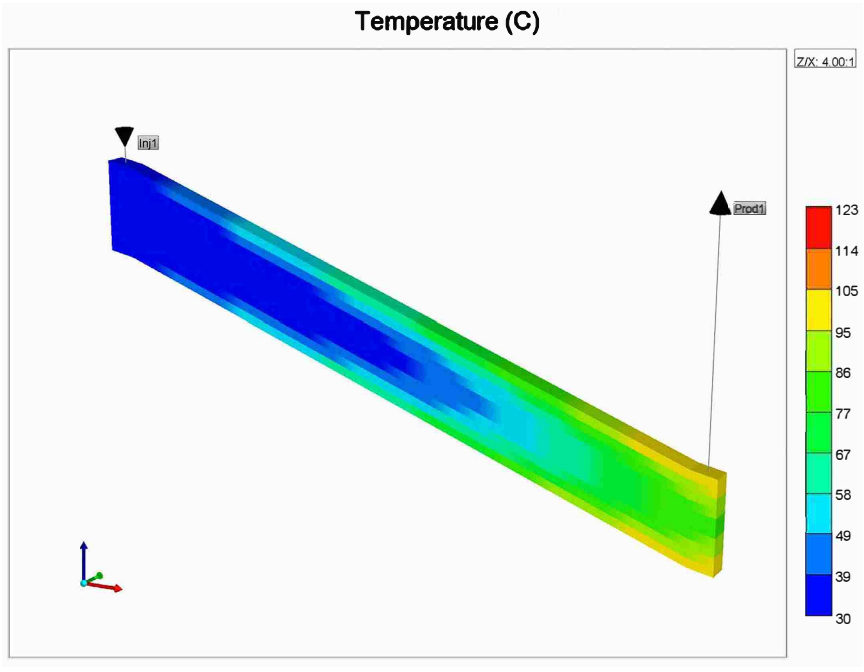

Figure 3.8: Thermal front at $t_D = 1$ (ca. 41.5 years). Vertical axis is exaggerated four times.

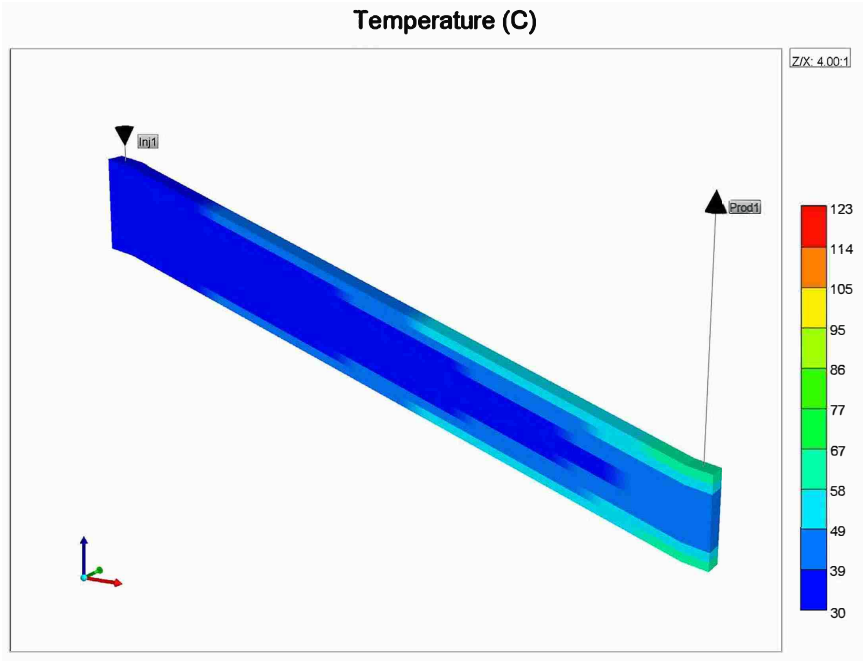

Figure 3.9: Thermal front at $t_D = 3$ (ca. 124 years). Vertical axis is exaggerated four times.

Chapter 4

A simplified model for regular line drive

To calculate the energy production rate, a model to predict the temperature of the production fluid versus time is needed and to assess the net energy that a system can produce, a model for predicting the thermal recovery factor is needed. In this chapter, the derived dimensionless numbers from Chapter 3 and Appendix B are confirmed and used to create predictive models for dimensionless production temperature and heat recovery factor. For doing this, important dimensionless numbers for different models are matched to validate that the models with the same dimensionless numbers would give identical dimensionless results. A Box-Bhenken design is then used to sample the parameter space and create the dimensionless numbers. A violin plot is created from the data for assessing uncertainty in the production temperature and energy recovery factor. A procedure known as all subset regression is used to compare possible models and select the optimum one. These simplified final models are then presented and assessed. This chapter first discusses a model developed for the dimensionless production temperature and then presents a model for thermal recovery factor.

4.1 A predictive model in dimensionless time

A major shortcoming of all previous published works is that they are only useful for specific dimensionless time. Some of these works model their response at specific times such as oil breakthrough (Wood et al., 2008). However, dimensionless time can be inserted inside the model according to the following: assume predictor variables $(x_1, x_2, \ldots, x_m)$ and regression coefficients $(\beta_0, \beta_1, ..., \beta_m)$ can model response Y (Eq. 4.1) with error ϵ.

$$Y = \beta_0 + \beta_1 x_1 + \cdots + \beta_m x_m + \epsilon. \tag{4.1}$$

Now, assume that the regression coefficients $\beta_0, \beta_1, \ldots, \beta_m$ are linear functions of dimensionless time and can be regressed independently.

$$\begin{aligned}
\beta_0 &= \alpha_{0_0} + \alpha_{0_1} t_D \\
\beta_1 &= \alpha_{1_0} + \alpha_{1_1} t_D \\
&\cdots \\
\beta_m &= \alpha_{m_0} + \alpha_{m_1} t_D
\end{aligned}$$

Substituting the regressed coefficients into the multiple regression formulation (Eq. 4.1) yields (Eq. 4.2):

$$\begin{aligned}
Y =& (\alpha_{0_0}\beta_0 + \alpha_{0_1}\beta_0 t_D) + \alpha_{1_0}\beta_1 x_1 + \alpha_{2_0}\beta_2 x_2 + \cdots + \alpha_{m_0}\beta_m x_m \\
&+ \alpha_{1_1}\beta_1 x_1 * t_D + \alpha_{2_1}\beta_2 x_2 * t_D + \cdots + \alpha_{m_1}\beta_m x_m * t_D
\end{aligned} \tag{4.2}$$

Eq. 4.2 means that dimensionless time can be added as a predictor for Y if the dimensionless time's interaction with other dimensionless numbers is retained.

4.2 Defining the response

A model for dimensionless production temperature can be used to calculate the rate of energy production versus time. The dimensionless production temperature is the ratio of the producing fluid temperature to the initial average reservoir temperature.

$$T_D = \frac{\text{production temperature}}{\text{initial average temperature}} \tag{4.3}$$

The energy recovery factor is defined as the ratio of the produced energy to the total energy in place before exploiting the reservoir (Muffler and Cataldi, 1978; Nathenson, 1975; Williams et al., 2008). Cumulative produced energy can be directly calculated using the energy recovery factor.

After testing and validating the dimensionless numbers, a model for dimensionless production temperature will be selected, presented and assessed and then the same systematic procedure will be used to develop a model for the thermal recovery factor.

4.3 Validating the scaling groups

For any given similar flow problem (i.e. same configuration and boundary conditions), matching the dimensionless numbers will yield similar dimensionless results (e.g. thermal recovery factor or dimensionless temperature) between scales. For validating the dimensionless numbers, the parameters in the groups are varied but the groups are held constant. Fifteen different reservoir models are considered such that their geometrical dimensional properties are different but their dimensionless groups are identical (for details see Appendix D and section 3.5). The energy recovery factor was then plotted versus dimensionless time. Matching the cases where the parameters have been changed but their group values remain the same would suggest that the dimensionless numbers adequately scale the system. The dimensional results vs. time for these fifteen models do not show any pattern (Figures 4.1a and 4.2a). The dimensionless results are plotted versus dimensionless time for the same set of models (Figures 4.1b and 4.2b). The models with identical dimensionless numbers (same color) show the same dimensionless temperature and thermal energy recovery factor.

4.4 Modeling production temperature

4.4.1 Box-Behnken design

Twenty parameters were used in the Box-Behnken design to sample the parameter space and model the thermal recovery factor (Table D.3). The models and parameters

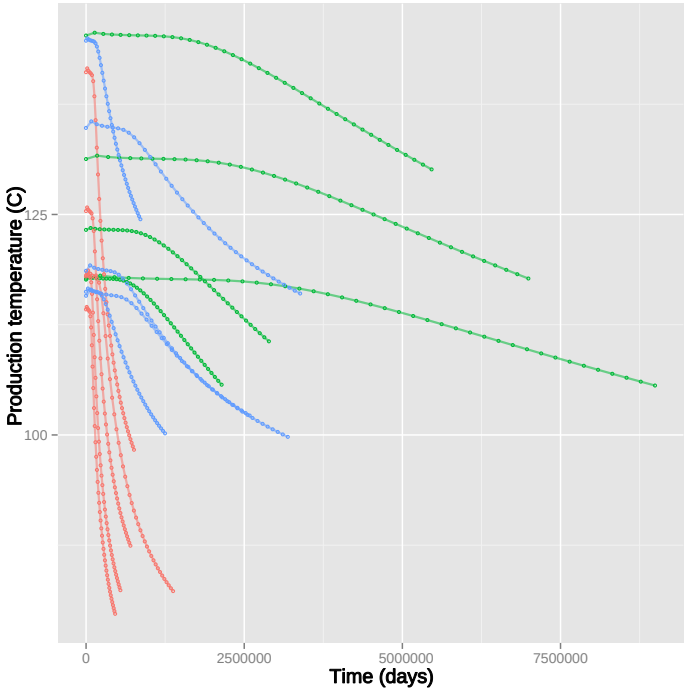

(a) Production temperature vs. time

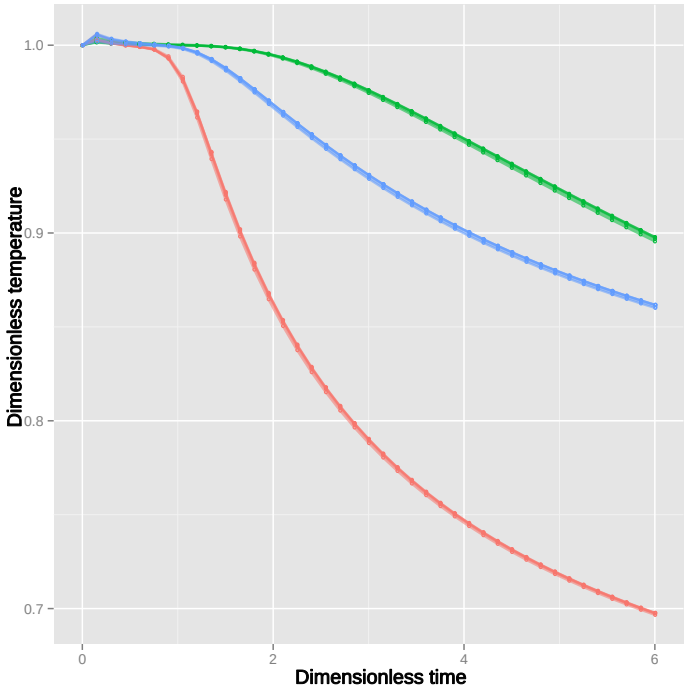

(b) Dimensionless production temperature vs. dimensionless time

Figure 4.1: Validating the dimensionless numbers. (A) shows production temperature versus time. Reservoirs with the same dimensionless numbers (i.e. same color) show different production temperature in dimensional space. These reservoirs are mapped to the dimensionless space. (B) shows dimensionless production temperature versus dimensionless time. Reservoirs with the same dimensionless numbers (same color) show similar dimensionless production temperature.

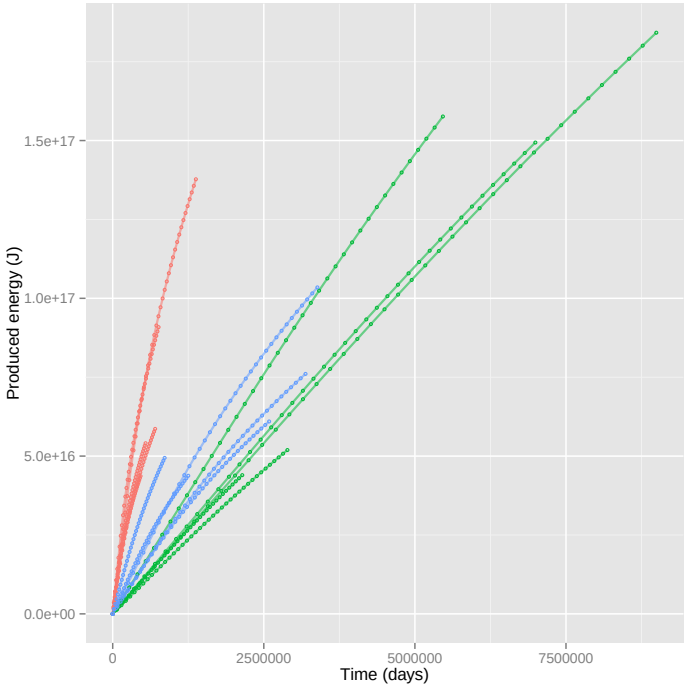

(a) Produced energy vs. time

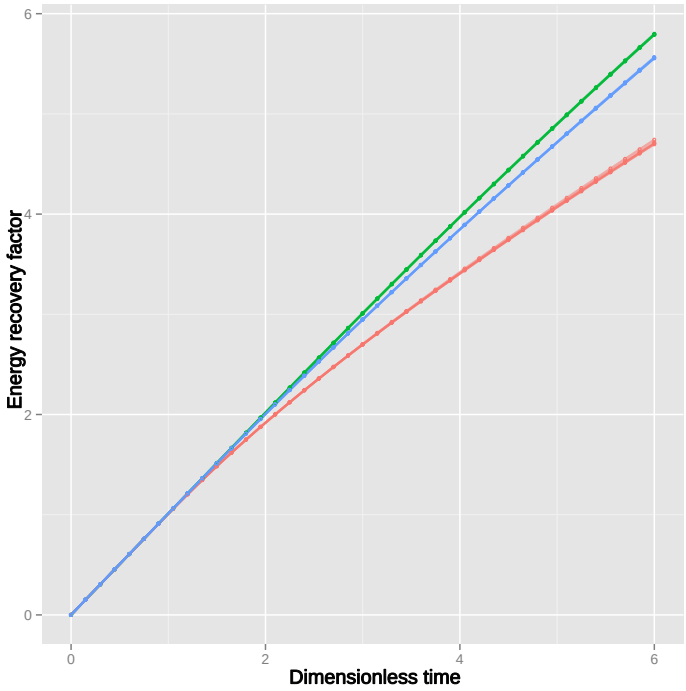

(b) Thermal recovery factor vs. dimensionless time

Figure 4.2: Validating the dimensionless numbers. (A) shows cumulative produced energy versus time. Reservoirs with the same dimensionless numbers (i.e. same color) show different produced energy in the dimensional space. These reservoirs are mapped to the dimensionless space. (B) shows thermal recovery factor versus dimensionless time. Reservoirs with the same dimensionless numbers (same color) show similar thermal recovery factor.

were discussed in Chapter 2 and Chapter 3. These runs were divided into 20 parallel runs per batch submission and required ca. 8 minutes to complete.

4.4.2 Uncertainty analysis

Once the thermal recovery factor curves corresponding to similar dimensionless numbers were matched (Figure 4.1b), violin plots can be created directly from the typical data (Figure 4.3, Table 4.1). Violin plots are useful for answering generic uncertain questions with minimum data (White, 2013). A violin plot shows a combination of the box plot and a rotated kernel density plot (i.e. an estimation for probability density function). In the violin plot, the middle dot shows the median (which is identical to the mode and maximum likelihood estimator of the mean in a normal distribution), the white boxes indicate the lower to upper quartile and the thin black lines are whiskers. Edges of the vertical lines show the minimum and maximum values. These plots can also be updated when additional certain data are available. Violin plots are used to show the statistical spread of the response variable as a function of time. For this work, they are also used to determine how many piecewise regression models are needed and to specify their dimensionless time ranges because it will be shown that dimensionless time is the key parameter in the modeled system. As Figure 4.4 indicates three regression models can predict the median points (i.e. red points): $0 < t_D \leq 0.5$, $0.5 < t_D \leq 1.5$ and $1.5 < t_D \leq 4$. Each segment can be considered as a line which goes through the median points. Section 4.5.1 presents an application of the violin plot. Note that for the system under consideration, $t_D > 4$ is well past the effective life of a geothermal power plant.

4.4.3 Relative importance analysis

Inspectional analysis quickly becomes overwhelming and performing a relative importance analysis is a good way to make it manageable. ANOVA is traditionally used to identify the factor significance of uncorrelated variables (White and Royer, 2003). The dimensionless numbers are algebraically independent but statistically dependent because they are functions of random parameters (Rice, 2006; Soong, 2004). Experimental design

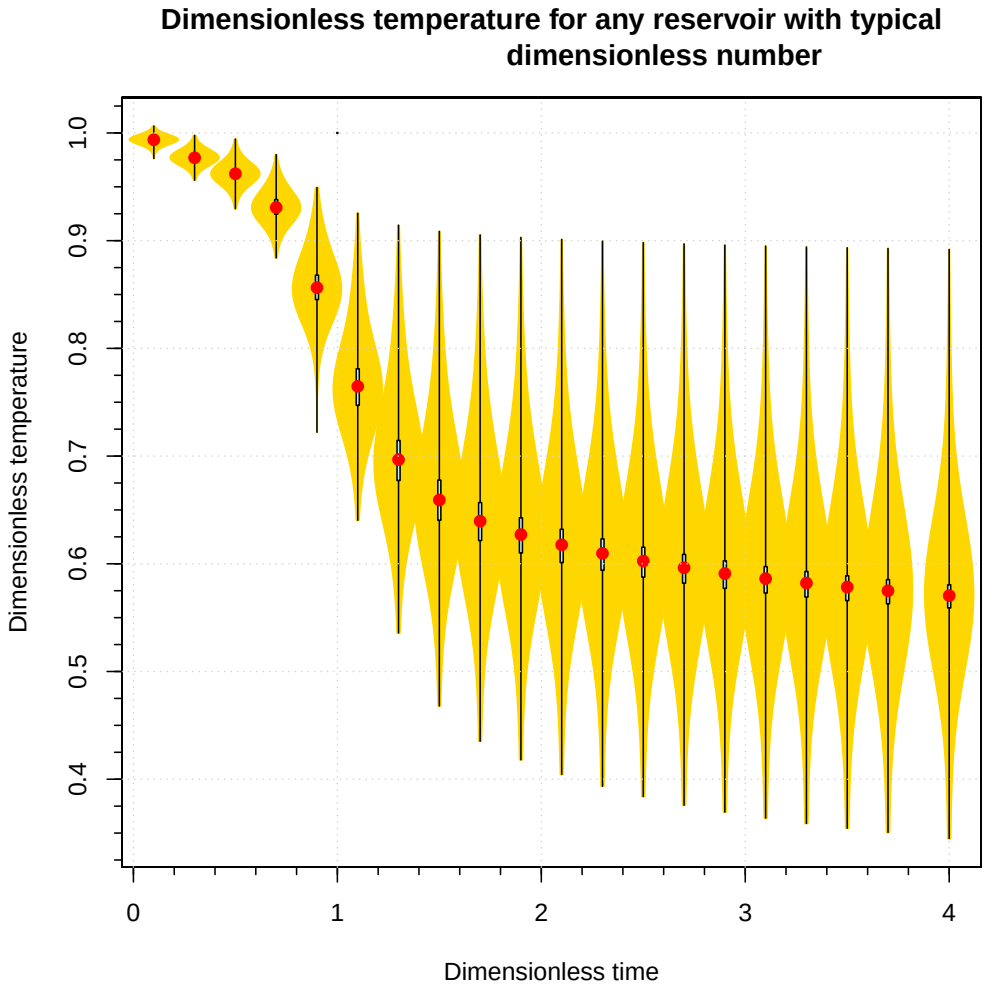

Figure 4.3: Violin plot for fining dimensionless temperature of uncertain reservoirs. This violin plot can be used as a rule of thumb for answering uncertain questions with minimum data.

is difficult when factors are correlated with each other (White and Royer, 2003). Another complication is that the relative importance of dimensionless numbers varies with dimensionless time. This change in relative importance is smooth and modeling every dimensionless time is redundant. Segmented (piecewise) regression is used for creating models with time-varying coefficients. The segmentation range can be chosen heuristically using violin plots and then be tested using trial and error to obtain the best segmented model. In order to determine the relative importance of the predictors, a robust tree-based algorithm, known as Boosting is used. The Boosting method creates an ensemble of independent re-

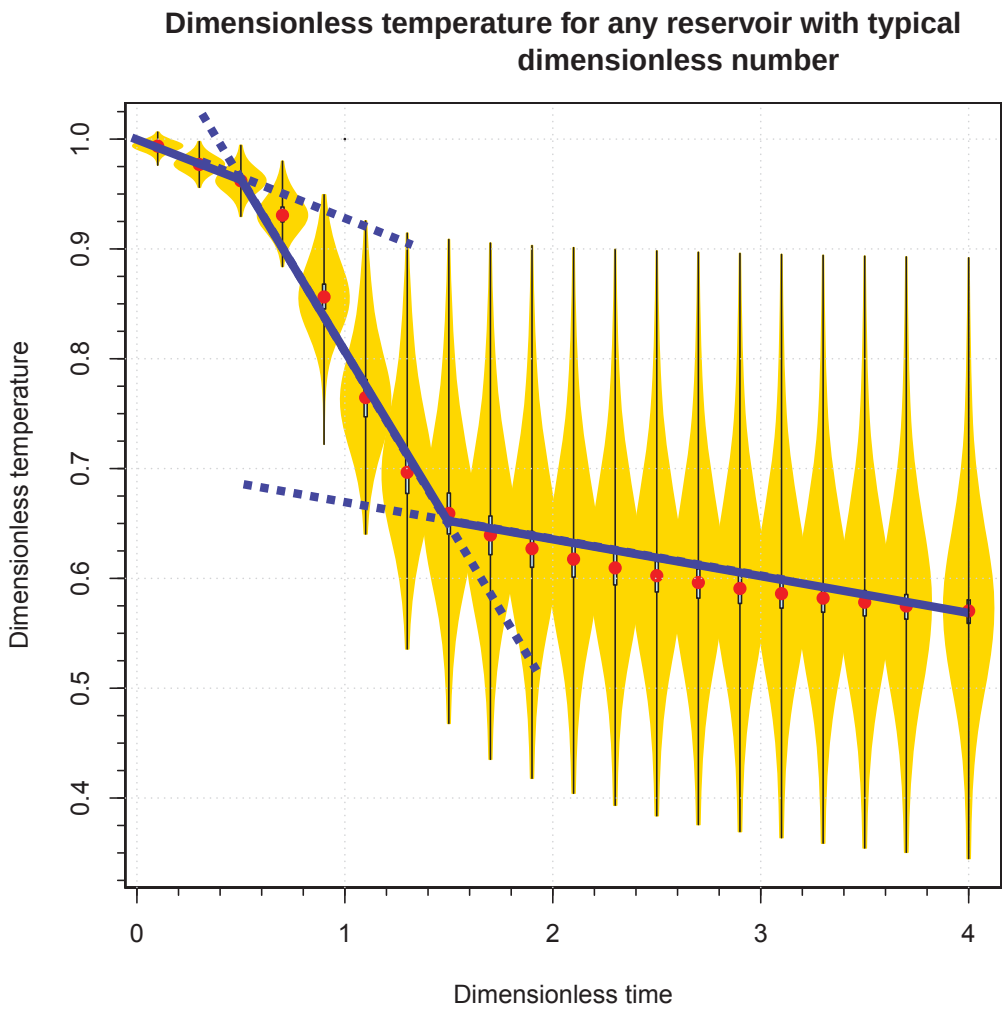

Figure 4.4: Three ranges for segmenting the model are considered: $0 < t_D \leq 0.5$, $0.5 < t_D \leq 1.5$ and $1.5 < t_D \leq 4$. The blue lines are sketched manually.

gression trees and updates them sequentially. Each tree is fit to the current step residual and the final model is the average of all the trees weighted by a shrinkage parameter which controls the rate at which boosting learns (James et al., 2013; Hastie et al., 2009; Kuhn and Johnson, 2013). There were 10,000 trees with an interaction depth of 4 and shrinkage parameter of 0.01 in the Boosting algorithm for this work.

Table 4.1 shows the ranges of the dimensionless numbers used in the sensitivity analysis of the dimensionless thermal recovery response. Dimensionless numbers can be rank-ordered based on their relative importance in predicting the response. Figure 4.5 shows important dimensionless numbers for each range of the dimensionless time. These dimen-

Table 4.1: Ranges of the dimensionless numbers used in the sensitivity analysis.

Group	π_1	π_2	π_3	π_4	π_5	π_6	π_7	π_8	π_9
Low	0.204	0.142	0.463	0.00163	0.0602	5.46	0.000	11.51	0
High	0.967	0.305	0.738	0.0598	0.1738	90.63	15.98	120.85	0.724

Group	π_{10}	π_{11}	π_{12}	π_{13}	π_{14}	π_{15}
Low	96.16	0.264	0.264	0.028	0.173	0
High	615.48	0.482	0.482	0.044	0.897	0.1325

sionless numbers change smoothly and continuously during dimensionless time. Dimensionless time is the most important factor in determining dimensionless temperature for the first two segments, $0 < t_D \leq 1.5$, while temperature ratio (π_{14}) is more important for $1.5 < t_D \leq 4$. Peclet number (π_{10}) and aspect ratio (π_8) are other important dimensionless numbers in predicting the response. The dimensionless numbers which do not affect the response can be safely disregarded for prediction. Dimensionless numbers with less than 1% relative importance were ignored. Finding the important dimensionless numbers is also very useful in the validation process (previous section). Reservoirs with identical important dimensionless numbers show similar behavior in the dimensionless space.

4.4.4 Model selection

The model was fit at eighty values for dimensionless time with step size of $t_D = 0.05$ (i.e. 0, 0.05, 0.1, ..., 4). Segmented (piecewise) regression was used to model dimensionless production temperature using 761 numerical simulation models. The violin plot is used for segmenting the model. The segments can then be tested using trial and error to find the best ranges for segmenting. As the violin plot shows, three lines can go through the median points (i.e. red points) and can sufficiently model the entire violin. The first segment ($0 \leq t_D \leq 0.5$) has 11 values for dimensionless time (761×11 samples points), the second segment ($0.5 < t_D \leq 1.5$) has twenty values (761×20 points) and the third segment ($1.5 < t_D \leq 4$) has fifty values for dimensionless time (761×50 points). A procedure known as "all subset regression" is used to assess possible sub-models (Figure 4.6). In this figure, the black area shows the presence of a predictor and the white area shows its absence. The

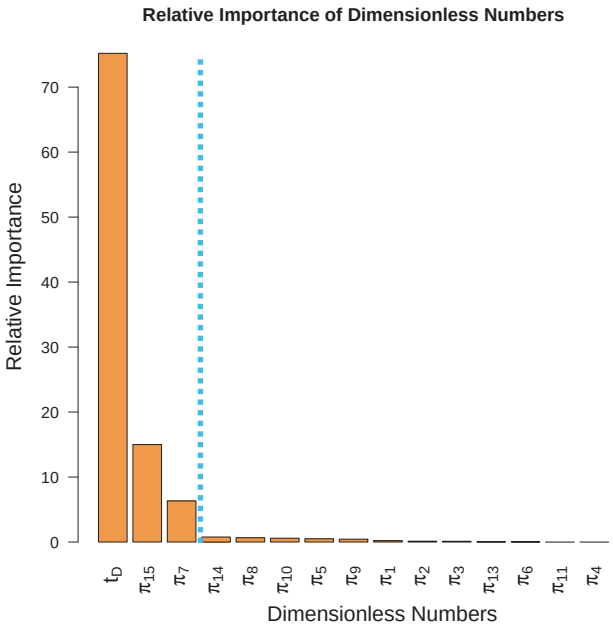

(a) Finding important dimensionless numbers for the range $0 < t_D \leq 0.5$

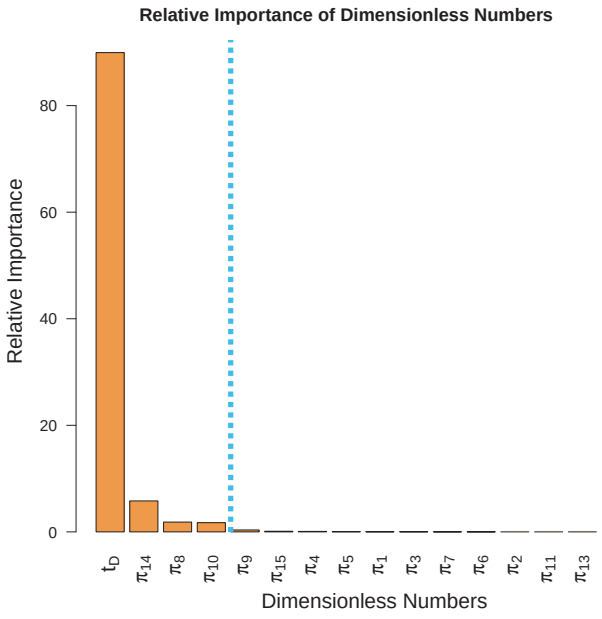

(b) Finding important dimensionless numbers for the range $0.5 < t_D \leq 1.5$

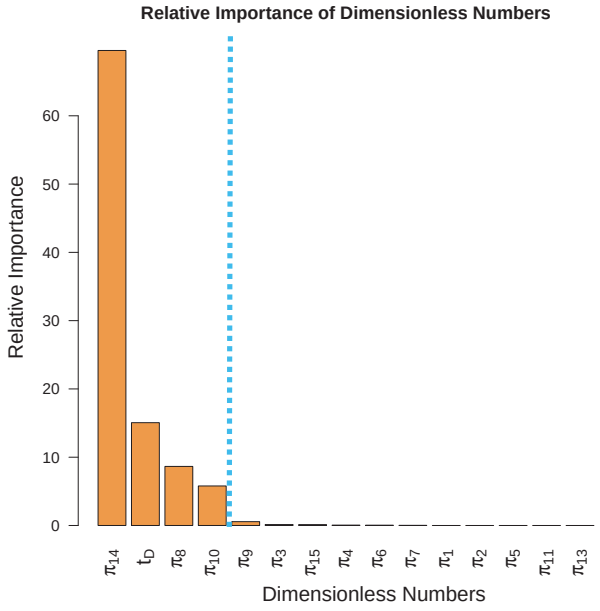

(c) Finding important dimensionless numbers for the range $1.5 < t_D \leq 4$

Figure 4.5: Important dimensionless numbers for each range of the dimensionless time. These dimensionless numbers change smoothly and continuously during dimensionless time. Because modeling every dimensionless time is redundant, the sensitivity analysis is performed over a range of dimensionless time. The cyan line shows the cut off for the dimensionless numbers with less than 1% importance.

purpose of the model selection for this work is to obtain a simple model with a smaller number of predictors and interactions than the full regression model. Choosing a simpler model trades off a small increase in the model bias. Introducing more predictors improves the R^2. The optimum model is both simple (i.e. has fewer terms) and representative (i.e. close to the best model). The choice of the final model is based on the modeler's selection and how the person trades off increasing terms with increasing R^2 value. The model with the largest R^2 value was found by the "all subset regression" algorithm and was selected as the best model (Figure 4.6). Thus, the best model for segment (a) has an R^2 value of 0.8853, the best model for segment (b) has an R^2 value of 0.9651 and the best model for segment (c) has an R^2 value of 0.9558. These selected models for dimensionless production temperature are presented in Box 1.

Box 1: Proposed model for dimensionless production temperature

For $0 \leq t_D \leq 0.5$, we have:

$$\begin{aligned} T_D =& 0.9936 - 0.0267 t_D - 0.0516 \pi_{15} + 0.0002 \pi_7 \\ & - 0.8434 t_D \pi_{15} + 0.0029 t_D \pi_7 + 0.0045 \pi_{15} \pi_7 \end{aligned} \tag{4.4}$$

for $0.5 < t_D \leq 1.5$, we have:

$$\begin{aligned} T_D =& 1.3429 - 0.6041 t_D - 0.4467 \pi_{14} - 0.001 \pi_8 + 0.6101 t_D \pi_{14} \\ & + 0.0022 t_D \pi_8 - 0.0003 t_D \pi_{10} + 0.0003 \pi_{10} \pi_{14} - 0.0001 \pi_8 \pi_{10} \end{aligned} \tag{4.5}$$

and for $1.5 < t_D \leq 4$, we have:

$$\begin{aligned} T_D =& 0.4528 - 0.0587 t_D + 0.4880 \pi_{14} - 0.0004 \pi_{10} + 0.0037 \pi_8 \\ & + 0.0729 t_D \pi_{14} - 0.003 \pi_{14} \pi_8 - 0.0003 t_D \pi_8 + 0.0004 \pi_{14} \pi_{10} \end{aligned} \tag{4.6}$$

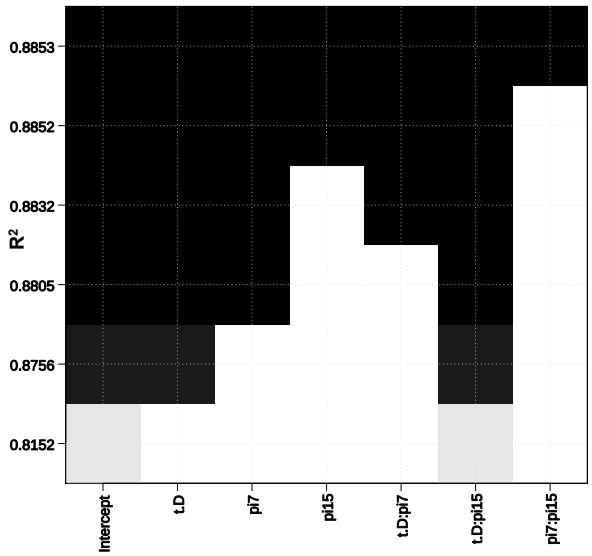

(a) $0 < t_D \leq 0.5$.

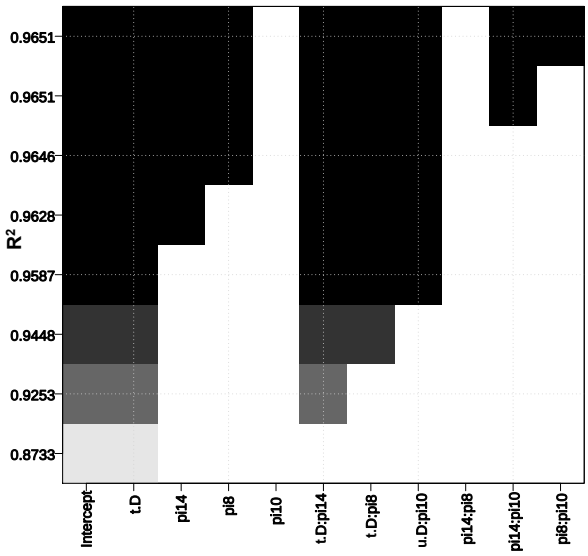

(b) $0.5 < t_D \leq 1.5$

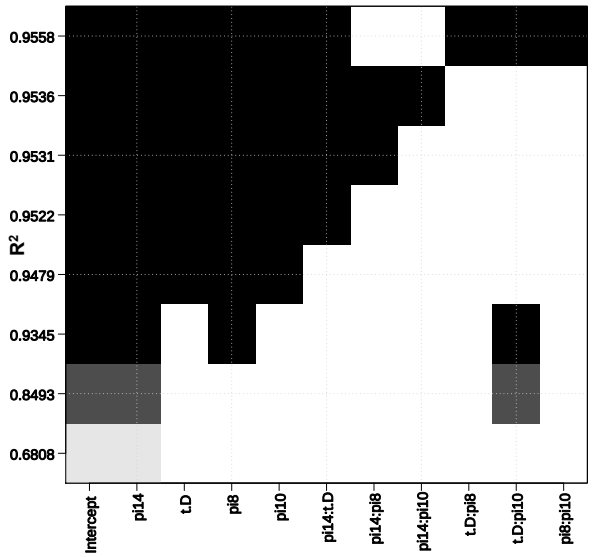

(c) $1.5 < t_D \leq 4$.

Figure 4.6: Reducing the models for production temperature at each range of dimensionless time.

4.4.5 Model assessment

Figure 4.7 shows the assessment of the reduced final model (Box 1). In each sub-figure 711 runs were used for training and 50 runs for testing. This means that 7,821 (i.e. 711×11) training samples (blue points) and 550 (i.e. 50×11) testing samples (red points) were used for the first segment, 14,220 training samples and 1,000 testing samples were used for the second segment and 35,550 training samples and 2,500 testing samples were used for the third segment.

4.5 Modeling thermal Recovery factor

The same procedure that was used to model dimensionless production temperature was used to develop a thermal recovery factor model. First, the violin plots are presented and the segmentation ranges for the dimensionless time are heuristically found. The important dimensionless numbers in each range of the dimensionless time are found and then the optimum models consisting of these important dimensionless numbers are selected. Finally, the simplified models are presented and assessed.

Again, violin plots are used to determine the number of segments and their ranges (Figure 4.9). Figure 4.9 indicates two piecewise regression models can predict the maximum likelihood points (i.e. red points). The ranges of the first and second model are $0 < t_D \leq 1$ and $1 < t_D \leq 4$. Each of these segments can be considered as a line which goes through the maximum likelihood points.

Finally, the reduced models (Box 2) are assessed using testing runs (Figure 4.12). Similar to dimensionless temperature, in each sub-figure 711 runs are used for training and 50 runs for testing. The assessment plots show a good match between the prediction and observation values and indicate that the fitted models are adequate for predicting thermal recovery factor. A sensitivity analysis is performed to find the important dimensionless numbers in predicting the response (Figure 4.10). For $0 \leq t_D \leq 1$, dimensionless time is the only predictor that is needed and for $1 < t_D \leq 4$, dimensionless time, temperature ratio (π_{14}) and Peclet number (π_{10}) are needed for predicting the recovery factor. Note

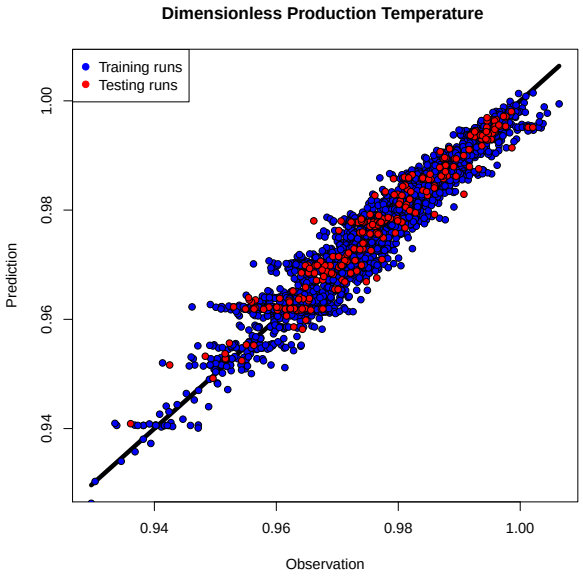

(a) $0 \leq t_D \leq 0.5$

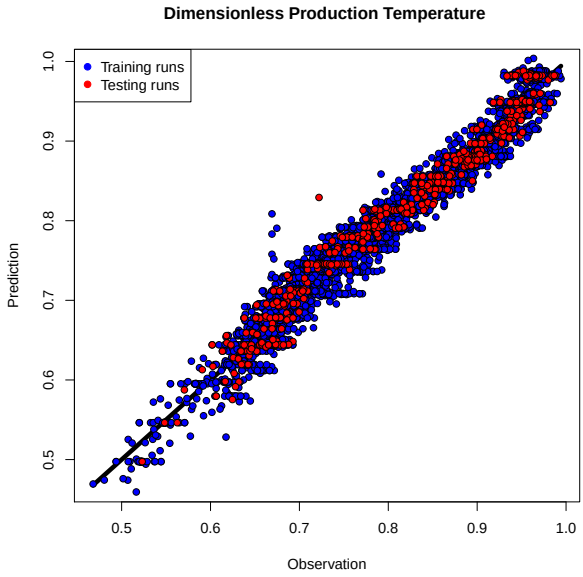

(b) $0.5 < t_D \leq 1.5$

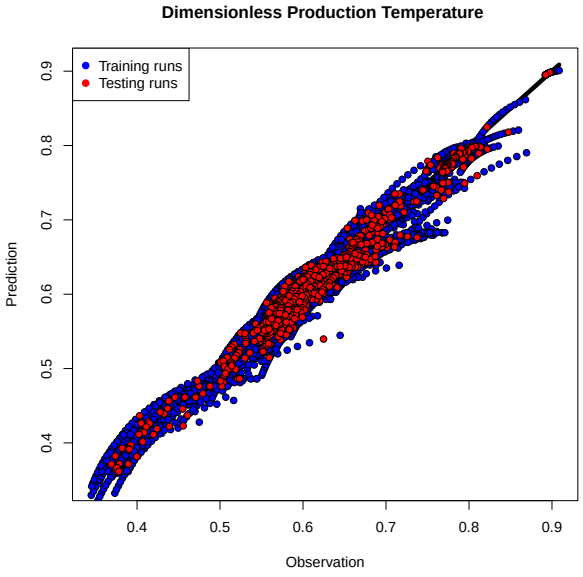

(c) $1.5 < t_D \leq 4$

Figure 4.7: Assessing the models for the dimensionless production temperature

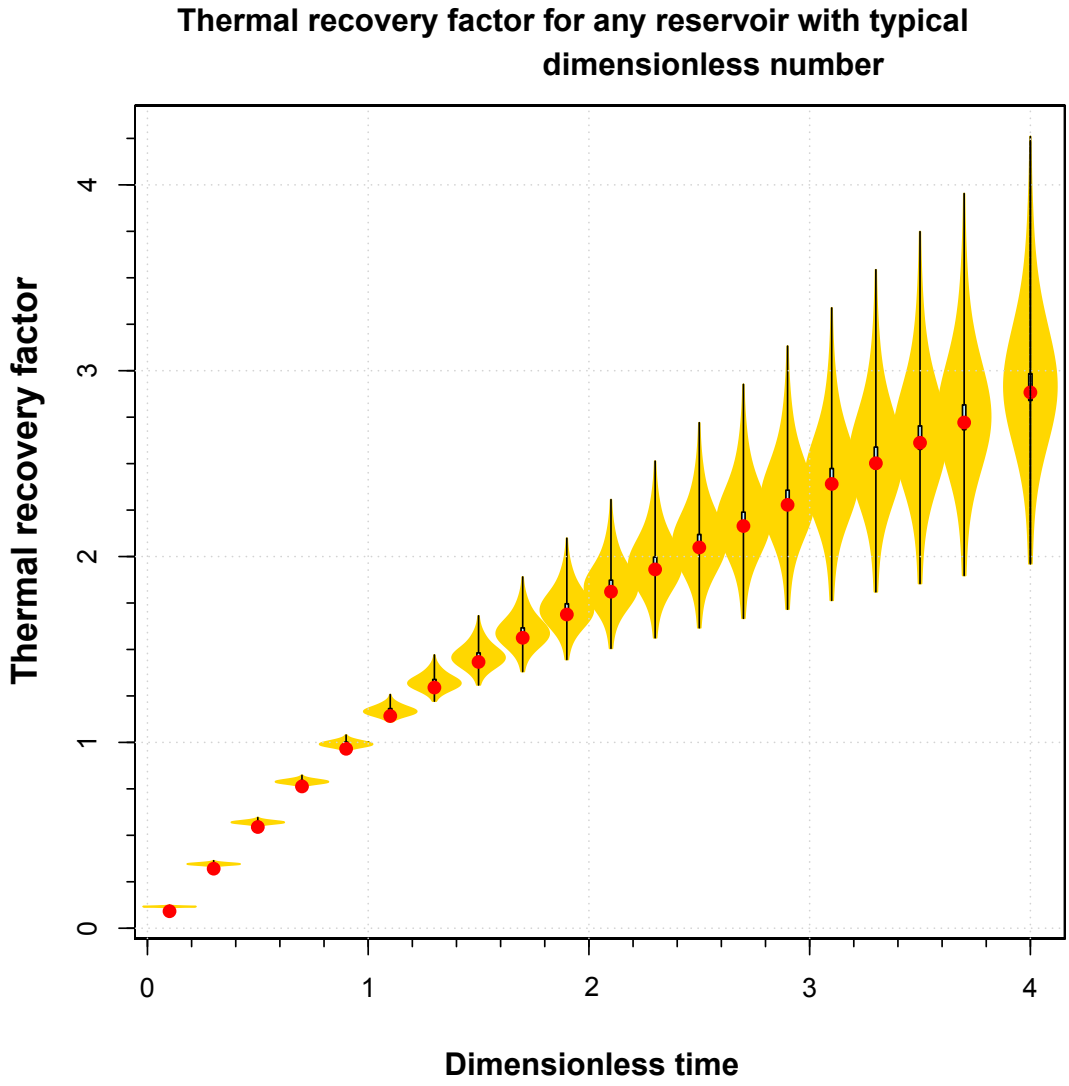

Figure 4.8: Violin plot for calculating thermal recovery factor of uncertain reservoirs.

that thermal recovery factor can have values greater than one because the reservoir gets heat from its cap/base rock.

These important dimensionless numbers were used for developing a model for the thermal recovery factor. Figure 4.11 compares the R^2 values of all subset regression models. An R^2 value of 0.9876 was chosen for the best model. The simplified models for energy recovery factor are highlighted in Box 2. Finally, the reduced models (Box 2) are assessed using testing runs.

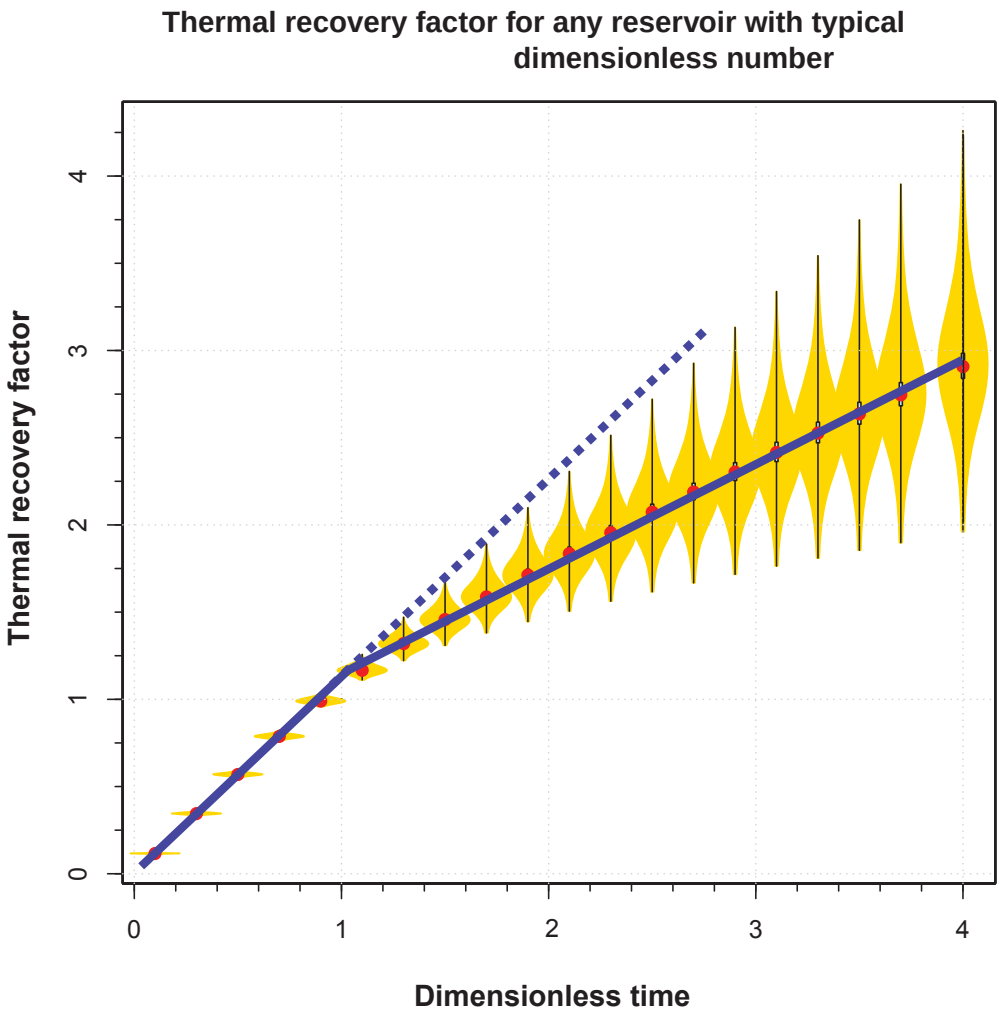

Figure 4.9: Thermal recovery factor vs. dimensionless time. Two ranges for segmenting the model are considered: $0 < t_D \leq 1$ and $1 < t_D \leq 4$. The blue lines are sketched manually.

Box 2: Proposed model for thermal recovery factor

For $0 \leq t_D \leq 1$, we have:

$$RF = 1.083 t_D \tag{4.7}$$

and for $1 < t_D \leq 4$, we have:

$$\begin{aligned} RF =& 1.01 + 0.0405 t_D - 0.829 \pi_{14} - 0.002 \pi_8 \\ &+ 1.01 t_D \pi_{14} + 0.0022 t_D \pi_8 - 0.0071 \pi_{14} \pi_8 \end{aligned} \tag{4.8}$$

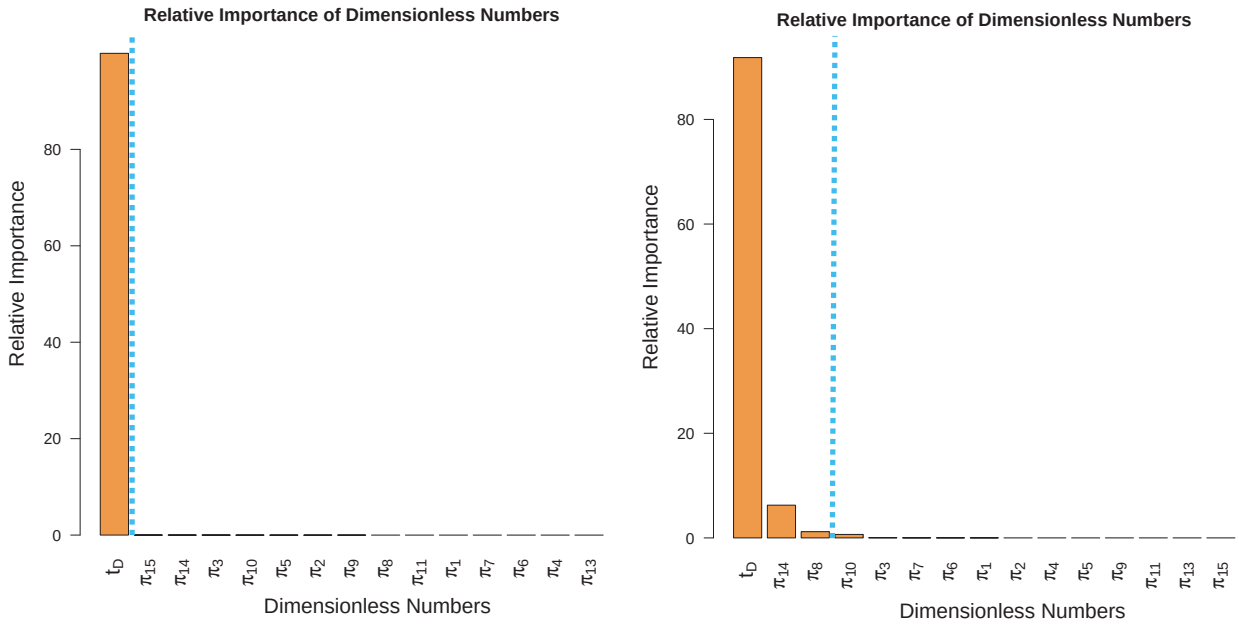

(a) $0 \leq t_D \leq 1$ (b) $1 < t_D \leq 4$

Figure 4.10: Finding the important dimensionless numbers for predicting thermal recovery factor for each range of the dimensionless time. The cyan line shows the cut off for the dimensionless numbers with less than 1% importance.

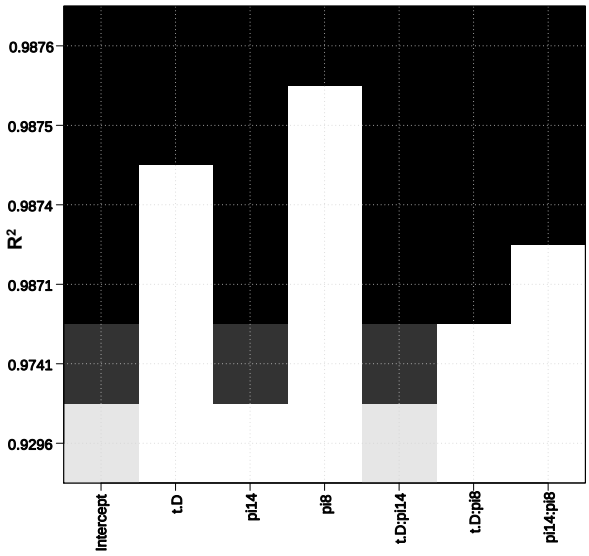

Figure 4.11: Comparing the R^2 values of the models for thermal recovery factor for the range $1 < t_D \leq 4$.

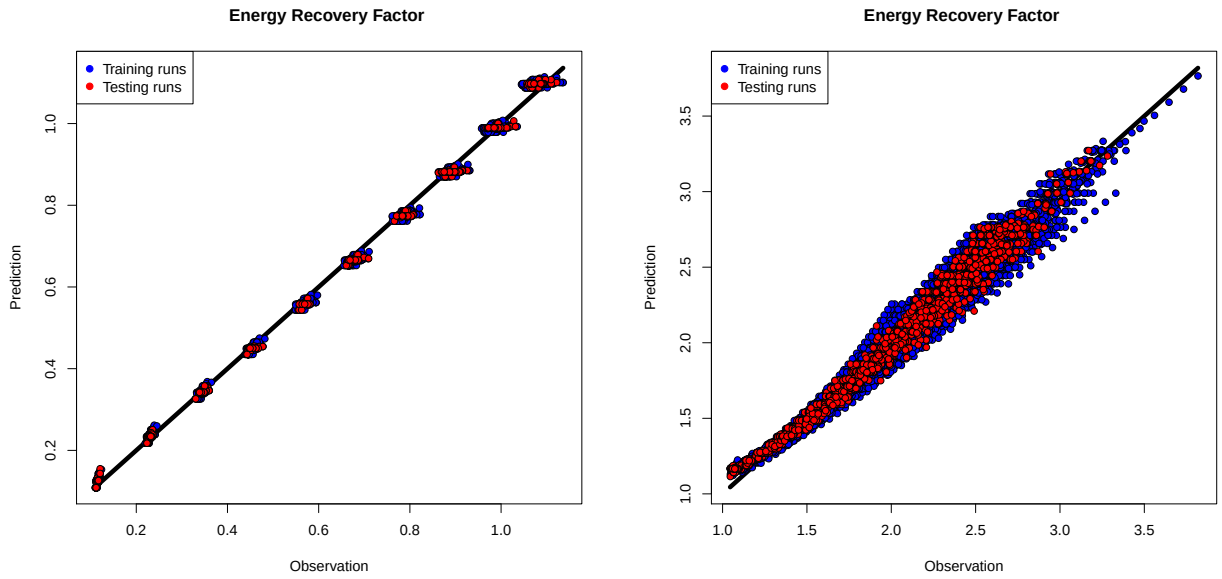

(a) $0 \leq t_D \leq 1$ (b) $1 \leq t_D \leq 4$

Figure 4.12: Assessing the models for the thermal recovery factor

4.5.1 Applications

In the following some applications of the developed models are discussed. A reservoir with some unknown data is described in Question 1 and the uncertainty in its temperature and produced energy is evaluated. Questions 2 and 3 use the developed models to calculate these values for the same reservoir.

Question 1) Ten wells (five injectors and five producers) are completed uniformly using line drive patterns in a geopressured-geothermal zone. The producers can provide a rate of 1,000 m^3/day, all of which is injected back into the reservoir. Only the area, thickness and porosity are known to be ca. 25 km^2 (12,500 m $\times$ 2,000 m), 30 m and 0.2 respectively. Other information about the reservoir (e.g average temperature, dip angle, temperature gradient, etc.) are unknown but they are within the statistics of the data in the area (Table 4.1). The goal is to obtain the dimensionless temperature and thermal recovery factor after 30 years of production.

Answer) Typical values for rock and water volumetric heat capacities are 2×10^6 and 4×10^6 J/m^3C and the drainage area available for a single line drive pattern is 60 acres (242,811 m^2):

$$\begin{aligned}\rho_m\, C_{pm} &= \phi\, \rho_w\, C_{pw} + (1-\phi)\, \rho_r\, C_{pr} \\ &= 0.2 \times 4 \times 10^6 + 0.8 \times 2 \times 10^6 = 2.4 \times 10^6\, J/m^3\,{}^\circ C\end{aligned}$$

$$M = \frac{\rho_m C_{pm}}{\rho_f C_{pf}} = \frac{2.4 \times 10^6}{4 \times 10^6} = 0.6 \tag{4.9}$$

$$t_D = \frac{1}{M}\frac{qt}{LWH} = \frac{1}{0.6}\frac{1000\,\frac{m^3}{day} \times 30 \times 365 days}{60 \times 4046.86 \times 30\, m^3} = 2.5 \tag{4.10}$$

Using Figure 4.3, maximum, median and minimum dimensionless temperature values for this reservoir after 30 years of production are ca. 0.39, 0.61 and 0.9 respectively.

Using Figure 4.8, the maximum, median and minimum thermal recovery factor values for this reservoir after 30 years of production are ca. 2.6, 2.1 and 1.6 respectively. The recovery factor can be multiplied by the initial energy in the system to obtain the energy that can be generated over the life of a plant. If this value is within the bounds of an economic project, detailed modeling and simulation could be used to assess the reservoir; if not, the area could be eliminated from consideration.

Question 2) For the reservoir in Question 1, if the average temperature, injection temperature and the rock's thermal capacity are $120\,^\circ C$, $40\,^\circ C$ and $2 \times 10^6 J/m^3\,^\circ C$ respectively; find the rate of energy production and net cumulative energy that could be produced from this system in 30 years.

Answer)

The maximum, median and minimum production temperature after 30 years of production are: 108, 73.2 and 46.8 C and water heat capacity at these temperatures is ca. $4.1 \times 10^6\ J/m^3\,°C$. Thus using Eq. 4.11, the rate of energy production would be 2.79×10^{11} (3.2 MW), 1.36×10^{11} (1.57 MW) and $2.79 \times 10^{10}\ J/day$ (0.32 MW) respectively .

$$\dot{H} = q\rho_f\, C_{pf}\, (T_{prod} - T_{inj}) \tag{4.11}$$

Now that we have temperature, we can find accurate water thermal capacity values at 120 $°C$ and 40 $°C$ are $3.99 \times 10^6\ J/m^3\,°C$ and $4.12 \times 10^6\ J/m^3\,°C$. The energy in place is:

$$\begin{aligned}\rho_m\, C_{pm} &= \phi\, \rho_w\, C_{pw} + (1-\phi)\, \rho_r\, C_{pr} \\ &= 0.2 \times 3.99 \times 10^6 + 0.8 \times 2 \times 10^6 = 2.398 \times 10^6\ J/m^3\,°C\end{aligned}$$

$$\begin{aligned}H_{in\,place} &= \rho_m\, C_{pm}\, V\, (T_p - T_{ref}) \\ &= 2.398 \times 10^6 \times 60 \times 4047 \times 30 \times (120 - 25) = 1.66 \times 10^{15}\ J\end{aligned}$$

The produced enthalpy is:

$$H_{pord} = RF \times H_{in\,place}$$

Thus the maximum, median and minimum produced energy values are 4.3×10^{15}, 3.49×10^{15}, 2.66×10^{15} J:

The enthalpy that is reinjected back into the reservoir during 30 years is:

$$H_{inj} = q_i t \rho_m\, C_{pm}\, (T_i - T_{ref})$$

$$= 1000 \times 4.12 \times 10^6 \times 30 \times 365.24 \times (40 - 25) = 6.77 \times 10^{14}\, J$$

The net produced energy is then:

$$H_{net} = H_{prod} - H_{inj}$$

The maximum, median and minimum net produced energy values from a single line drive pattern would be 3.62×10^{15}, 2.81×10^{15} and 1.98×10^{15} J.

Question 3) For the reservoir in the Question 1, assume a length and width of 1215 m and 200 m and a thermal conductivity of 2.5×10^5 for the reservoir rock. Calculate the dimensionless production temperature and energy recovery factor using the developed models.

Answer)

$$\kappa = \frac{\lambda_m}{\rho_f C_{pf}} = \frac{2.5 \times 10^5}{4 \times 10^6} = 0.0625 \tag{4.12}$$

$$\pi_{10} = Pe = \frac{u_T H}{\kappa} = \frac{q}{\kappa W} = \frac{1000}{0.0625 \times 200} = 80 \tag{4.13}$$

$$\pi_{14} = \frac{40}{120} = 0.333 \tag{4.14}$$

$$\pi_8 = \frac{L}{H} = \frac{1215}{30} = 40.5 \tag{4.15}$$

$$\begin{aligned} T_D =& 0.4528 - 0.0587 t_D + 0.4880 \pi_{14} - 0.0004 \pi_{10} + 0.0037 \pi_8 \\ &+ 0.0729 t_D \pi_{14} - 0.003 \pi_{14} \pi_8 - 0.0003 t_D \pi_8 + 0.0004 \pi_{14} \pi_{10} = 0.587 \end{aligned}$$

$$RF = 1.01 + 0.0405t_D - 0.829\pi_{14} - 0.002\pi_8 + 1.01t_D\pi_{14} + 0.0022t_D\pi_8 - 0.0071\pi_{14}\pi_8 = 1.72$$

Thus, the estimated production temperature after 30 years is 70.4 $^\circ C$ and the total produced energy and net produced energy after 30 years are 2.86×10^{15} and 2.18×10^{15}, respectively.

In this chapter, a heat extraction model was developed based on a regular line drive design. Similar design is used in studies such as waterflooding and CO_2 flooding (Shook et al., 1992; Wood et al., 2008). In the next chapter, another design known as Zero Mass Withdrawal will be discussed which requires one horizontal wellbore. In this design, the geofluid is not brought to the surface and is injected back into the reservoir after its energy content is extracted using a heat exchanger installed inside the wellbore.

Chapter 5

Zero Mass Withdrawal (ZMW) design

In this chapter, the governing equations describing a Zero Mass Withdrawal system (Figure 5.1) are derived from the fundamental partial differential equations (Appendix A). The spatial dimensions of the problem are scaled using available analytical solutions. Then, the dimensionless numbers are derived using inspectional analysis (Appendix C) and explained.

5.1 Zero Mass Withdrawal (ZMW) model

- Continuity equation

For the three-dimensional system shown in Figure 5.1, the continuity equation (see Eq. A.12 in Appendix A) reduces to Eq. 5.1.

$$\begin{aligned}\phi(c_t\frac{\partial p}{\partial t}-\beta_t\frac{\partial T}{\partial t})+u_x(c_f\frac{\partial p}{\partial x}-\beta_f\frac{\partial T}{\partial x})+u_y(c_f\frac{\partial p}{\partial y}-\beta_f\frac{\partial T}{\partial y})\\ +u_z(c_f\frac{\partial p}{\partial z}-\beta_f\frac{\partial T}{\partial z})+\frac{\partial u_x}{\partial x}+\frac{\partial u_y}{\partial y}+\frac{\partial u_z}{\partial z}=0\end{aligned} \tag{5.1}$$

- Darcy equation

For writing the Darcy equation along the new coordinates, the gravity vector in is broken down along the axes (see also Eq. A.13).

$$\begin{aligned}u_x&=-k_x(\frac{\partial p}{\partial x}-\rho g\sin\alpha_x\cos\alpha_y)\\ u_y&=-k_y(\frac{\partial p}{\partial y}-\rho g\cos\alpha_x\sin\alpha_y)\\ u_z&=-k_z(\frac{\partial p}{\partial z}-\rho g\cos\alpha_x\cos\alpha_y)\end{aligned} \tag{5.2}$$

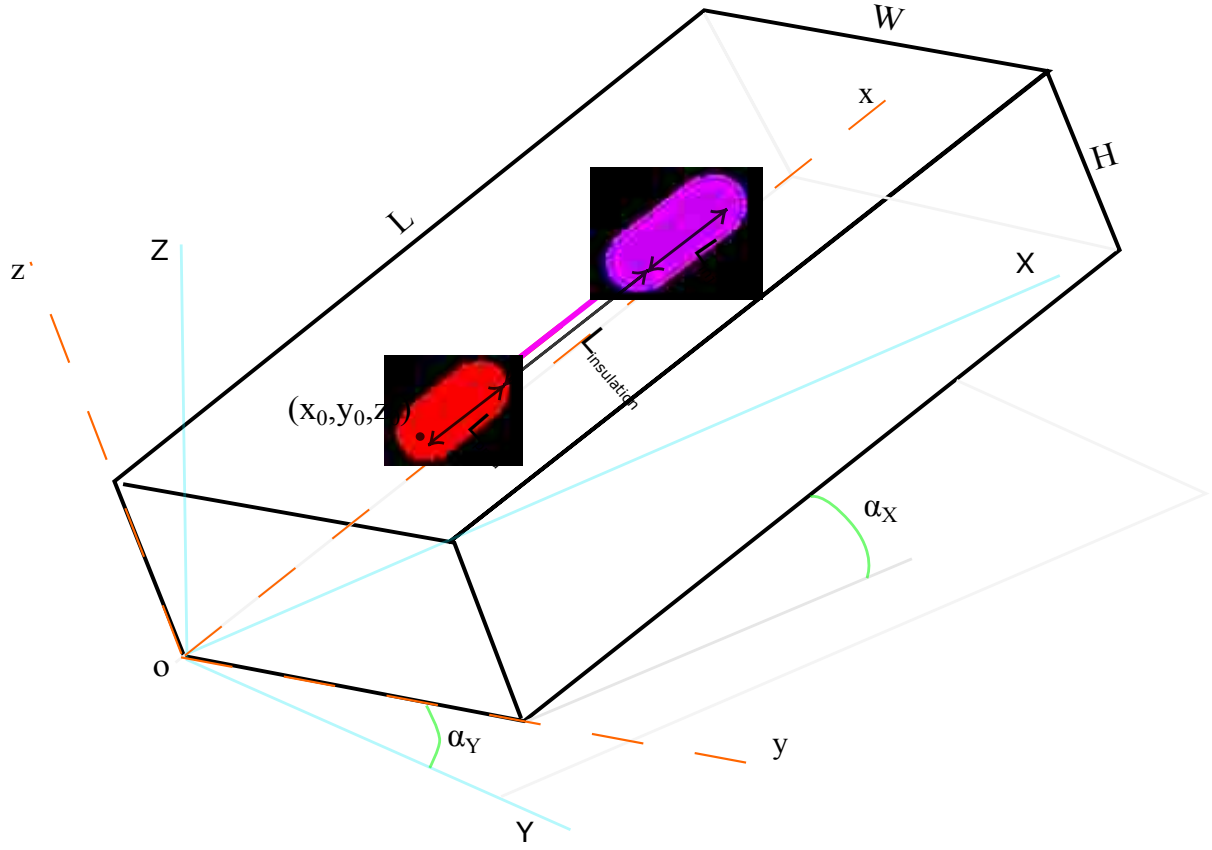

Figure 5.1: Zero Mass Withdrawal (ZMW) design.This design is based on Feng et al. (2014) and Novakovic (2002) work for studying the effect of downhole heat exchangers on the geopressured geothermal reservoirs using a single horizontal wellbore. For Gulf coast geothermal reservoirs W/H is more than ca. 120, , assuming $L = W = Area^{0.5}$.

- Energy equation

  The energy equation can be written by expanding Eq. A.17 in three-dimensions:

$$M\frac{\partial T}{\partial t} + u_x\frac{\partial T}{\partial x} + u_y\frac{\partial T}{\partial y} + u_z\frac{\partial T}{\partial z} - T\phi(c_t\frac{\partial p}{\partial t} - \beta_t\frac{\partial T}{\partial t}) - \kappa(\frac{\partial^2 T}{\partial x^2} + \frac{\partial^2 T}{\partial y^2} + \frac{\partial^2 T}{\partial z^2}) = 0 \quad (5.3)$$

- Reservoir boundary condition

  For the overburden and underburden heat conduction, Eq. A.18 yields Eq. 5.4 and Eq. 5.5, in which $\kappa'_{ob} = \lambda_{ob}/(\rho_{ob}C_{p,ob})$ and $\kappa'_{ub} = \lambda_{ub}/(\rho_{ub}C_{p,ub})$.

$$\frac{\partial T}{\partial t} = \kappa'_{ob}(\frac{\partial^2 T}{\partial x^2} + \frac{\partial^2 T}{\partial y^2} + \frac{\partial^2 T}{\partial z^2}) \quad (5.4)$$

$$\frac{\partial T}{\partial t} = \kappa'_{ub}\left(\frac{\partial^2 T}{\partial x^2} + \frac{\partial^2 T}{\partial y^2} + \frac{\partial^2 T}{\partial z^2}\right) \tag{5.5}$$

$$T_{ob,z=\infty} = T_{ob,t=0} \qquad At\ z = \infty, \forall x, y, t \tag{5.6}$$

$$T_{ub,z=-\infty} = T_{ub,t=0} \qquad At\ z = -\infty, \forall x, y, t \tag{5.7}$$

In practice, a semi-analytical thermal boundary condition is used for numerically modeling Eqs. 5.4 and 5.5 (Vinsome and Westerveld, 1980). For applying IA to the boundary heat gain/loss process, only a description of the boundary condition at the interface is important. The tail of the temperature distribution does not transfer energy to the system (Vinsome and Westerveld, 1980). Thus having $z = \infty$ in Eqs. 5.6, 5.7 does not affect the inspectional analysis. Boundary equations 5.9 and 5.10 do not provide additional information about the system because the initial condition of the reservoir contains this informations so Eqs. 5.9, 5.10, 5.6 and 5.7 can be ignored only addressing Eqs. 5.4 and 5.5.

$$\begin{aligned}
u_x = 0, \frac{\partial T}{\partial x} = 0 \qquad & At\ x = 0, \forall y, z, t \\
u_x = 0, \frac{\partial T}{\partial x} = 0 \qquad & At\ x = L, \forall y, z, t \\
u_y = 0, \frac{\partial T}{\partial y} = 0 \qquad & At\ y = 0, \forall x, z, t \\
u_y = 0, \frac{\partial T}{\partial y} = 0 \qquad & At\ y = W, \forall x, z, t \\
u_z = 0 \qquad & At\ z = 0, \forall x, y, t \\
u_z = 0 \qquad & At\ z = H, \forall x, y, t
\end{aligned} \tag{5.8}$$

T_{avg} indicates the average initial temperature of the reservoir. This temperature can be calculated by performing temperature buildup tests on the wells or using statistical methods (Grant, 2013). Well temperature and average reservoir temperature normally

exist in legacy data (John et al., 1998; Bassiouni, 1980).

$$T_{ob,t=0} = T_{avg} + (\tau \sin\alpha_X \cos\alpha_Y)(\frac{L}{2} - x) + (\tau \sin\alpha_Y \cos\alpha_X)(\frac{W}{2} - y) + (\tau \cos\alpha_X \cos\alpha_Y)(\frac{H}{2}) \qquad At\ z = H, t = 0, \forall x, y \tag{5.9}$$

$$T_{un,t=0} = T_{avg} + (\tau \sin\alpha_X \cos\alpha_Y)(\frac{L}{2} - x) + (\tau \sin\alpha_Y \cos\alpha_X)(\frac{W}{2} - y) - (\tau \cos\alpha_X \cos\alpha_Y)(\frac{H}{2}) \qquad At\ z = H, t = 0, \forall x, y \tag{5.10}$$

- Well boundary condition

  The boundary condition for the horizontal injector and producer can be described as:

- Producer

$$q_{inj} = \int_0^{L_{inj}} u_{inj}(2\pi r_w) dL \tag{5.11}$$

- Injector

$$q_{prod} = \int_0^{L_{prod}} u_{prod}(2\pi r_w) dL \tag{5.12}$$

For a zero mass withdrawal system, we have:

$$q_{inj} = -q_{prod} = q \tag{5.13}$$

- Initial condition

The initial pressure of the reservoir is assumed to be uniform and the temperature in the reservoir is distributed according to the geothermal gradient:

$$p = p_i \qquad At\ t = 0, \forall x, y, z \tag{5.14}$$

$$\begin{aligned} T = T_{avg} &+ (\tau \sin\alpha_X \cos\alpha_Y)(\frac{L}{2} - x) + (\tau \sin\alpha_Y \cos\alpha_X)(\frac{W}{2} - y) \\ &+ (\tau \cos\alpha_X \cos\alpha_Y)(\frac{H}{2} - z) \end{aligned} \tag{5.15}$$

5.2 Numerical modeling

Figure 5.2 shows a ZMW model with a $50 \times 50 \times 10$ Cartesian grid system (each grid cell is $75 \times 75 \times 10\ m$) with an injection temperature of $30\,C$ and an average reservoir temperature of $130\,C$. The injection, insulation and production lengths are 650, 650 and 510 m, respectively and the injection and production rates are $1000\,m^3/day$. This model is a simulation equivalent of an infinite system. The flow rate is kept low and the temperature change is kept moderate to prevent completion problems and seismic activities. The reservoir rock cools down as the front slowly propagates in the reservoir and moves towards the production section. Figure 5.2 shows thermal front at $t_D = 0.1$ (ca. 30 years) when still no breakthrough has occurred. In this figure, red and blue colors indicate hot and cold (i.e. less hot) water, respectively. Thermal breakthrough happens around $t_D = 0.5$ (ca. 160 years, Figure 5.3). After breakthrough, production of the arrived fluid and an increase in the radius of thermal propagation slows down the front speed (Figures 5.4 and 5.5). The same model setup is used in the experimental design in Chapter 6.

5.3 Scaling dimensions

For doing scale analysis, the spatial extent of the region in which phenomenon happens should be specified and the dimensionless groups should be defined using these spatial dimensions. For the line drive design, the spatial extent of the streamlines are from the injector to the producer (i.e. the entire reservoir). When the size of the region and the

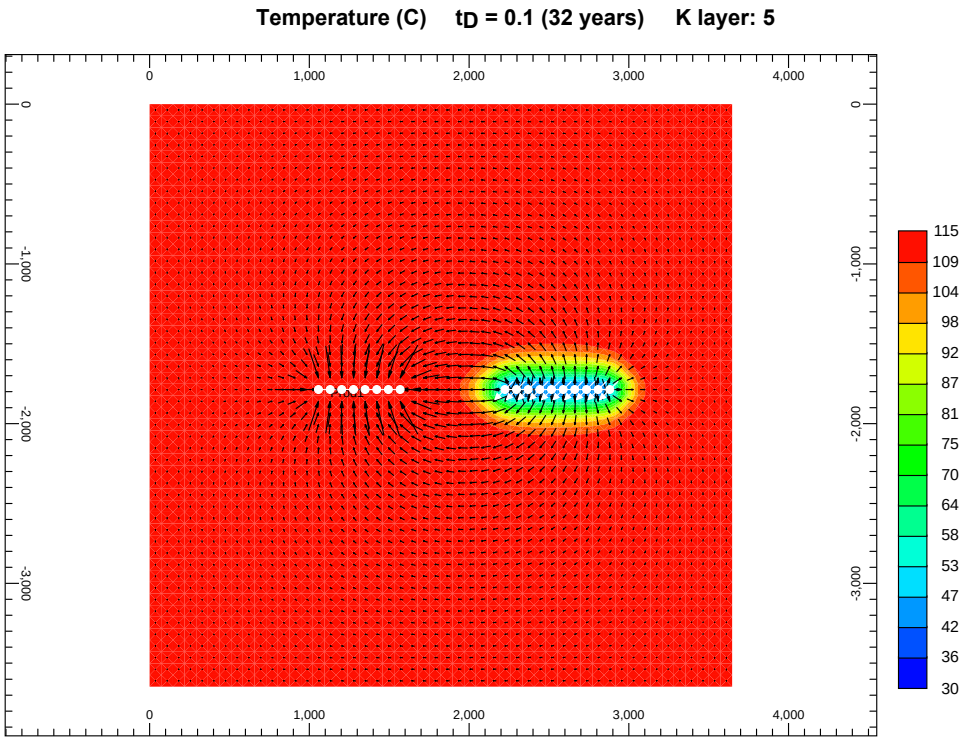

Figure 5.2: Thermal front at $t_D = 0.1$ (ca. 32 years)

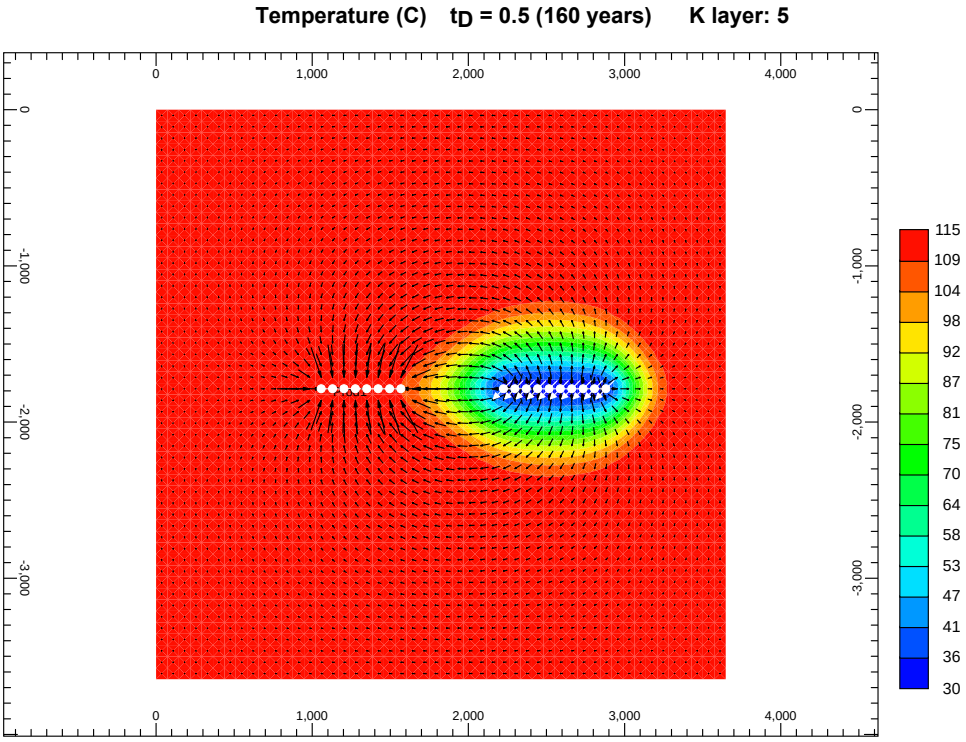

Figure 5.3: Thermal front at breakthrough $t_D = 0.5$ (ca. 160 years).

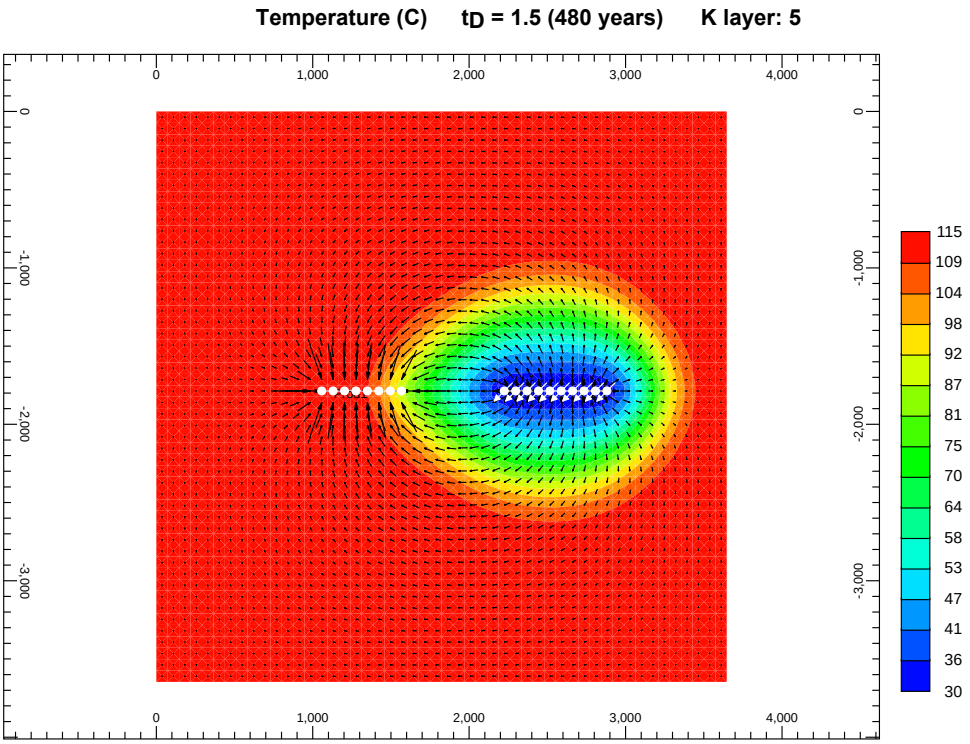

Figure 5.4: Thermal front at $t_D = 1.5$ (ca. 480 years)

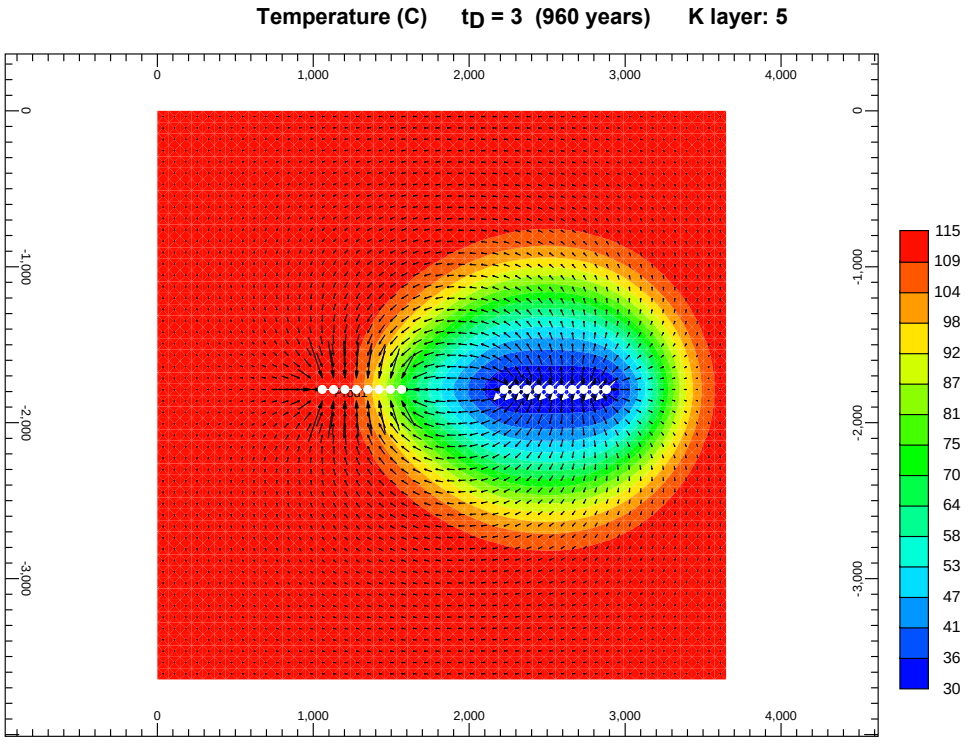

Figure 5.5: Thermal front at $t_D = 3$ (ca. 960 years).

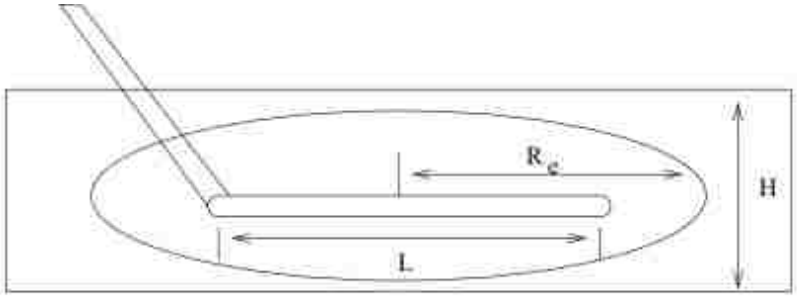

Figure 5.6: Schematic of a horizontal well with length L and drainage radius of R_e. Figure from Lu (1998).

configuration of the streamlines are not known, the scale analysis can start by specifying the dimensions of this spatial region suggested by analytical solutions. Bejan (2013) gives examples on how scaling gives the same order of magnitude results as analytical solutions but with less intellectual effort. Tan (2014) provides examples on how dimensional analysis may seem to be right but give incorrect results if the scaled dimensions are not properly selected.

For the ZMW case, the extent of the scaling region in the x direction is found by investigating the analytical solutions available for horizontal wells. The extent of the scaling region in the y direction is found by investigating the analytical solutions available for a doublet geothermal system. The extent of the scaling region in the z direction is the thickness of the system similar to the line drive system.

Lu (1998) describes scaling a horizontal well by its length, for calculating productivity and well testing of horizontal wells (Figure 5.6). For a homogeneous case, the x and y and z dimensions of a horizontal well are scaled by its length (L_{well}) as follows:

$$x_D = \frac{x}{L_{well}}$$
$$y_D = \frac{y}{L_{well}}$$

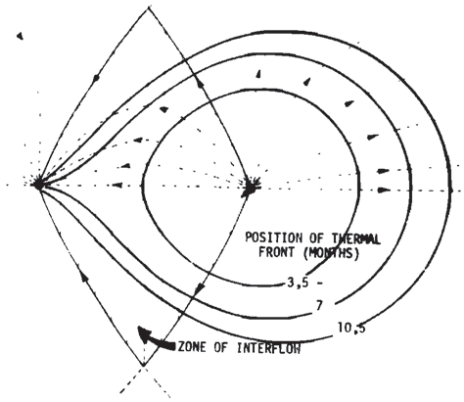

Figure 5.7: Schematic of a doublet system. Thermal front and hyraulic streamlines are shown in this figure. Figure from Gringarten and Sauty (1975).

$$z_D = \frac{z}{L_{well}}$$
$$t_D = \frac{k_x t}{\phi \mu C_t \, L_{well}^2} \tag{5.16}$$

Gringarten and Sauty (1975) develop a mathematical model for a doublet in a two dimensional horizontal infinite aquifer with uniform thickness H. The injection and production wells produce from the entire aquifer with rate q and the distance between the two wells is D (Figure 5.7). Their model considers heat conduction between the reservoir and the cap and bed rock but thermal conductivity inside the reservoir is neglected. They transform the convection equation inside the reservoir coupled with conduction with the cap and base rocks using Laplace transformation and use potential theory and streamline functions to develop the following dimensionless time (t_D):

$$t_D = \frac{\rho_f C_f}{\rho_t C_t} \frac{q\, t}{D^2\, H} \tag{5.17}$$

By inspecting the spatial scaling of a horizontal well (Eq. 5.16) and comparing the hydraulic dimensionless time of the line drive system, $t_{D_{hyd}} = \frac{\phi C_f}{C_t} \frac{qt}{LWH}$, with the horizontal well dimensionless time, the scaling in the x direction for a ZMW system appears to be

the length of the horizontal well (which is used for x_1^* in Appendix C). By comparing the thermal dimensionless time of a doublet system (Eq. 5.17) with that of the line drive system ($t_{D_{th}} = \frac{\rho_f C_f}{\rho_t C_t} \frac{q\,t}{LWH}$), the scaling in the y direction for a ZMW system appears to be the distance between the production and injection sections of the well (L_{ins} which is used for y_1^* in Appendix C).

5.4 Dimensionless groups

Appendix C shows how to apply scaling and inspectional analysis to obtain the following dimensionless numbers for the ZMW system:

$$\pi_1 = \frac{\phi c_t}{c_f} \qquad \pi_2 = \frac{\phi \beta_t}{\beta_f}$$

$$\pi_3 = M \qquad \pi_4 = c_f p_1^* = \frac{c_f \mu q (L_{prod} + L_{ins} + L_{inj})}{H L_{ins}}$$

$$\pi_5 = \beta_f T_1^* = \beta_f T_{avg} \qquad \pi_6 = \frac{(L_{prod} + L_{ins} + L_{inj})}{H} \sqrt{\frac{k_z}{k_x}}$$

$$\pi_7 = \frac{L_{ins}}{H} \sqrt{\frac{k_z}{k_y}} \qquad \pi_8 = \frac{(L_{prod} + L_{ins} + L_{inj})}{H} \tan(\alpha_X)$$

$$\pi_9 = \frac{L_{ins}}{H} \tan(\alpha_Y) \qquad \pi_{10} = \frac{L_{prod}}{H}$$

$$\pi_{11} = \frac{L_{inj}}{H} \qquad \pi_{12} = \frac{L_{ins}}{H}$$

$$\pi_{13} = \frac{k_x}{\mu} \frac{\rho_f g \sin\alpha_X \cos\alpha_Y L_{ins} H}{q} \qquad \pi_{14} = \frac{u_{x1}^* z_1^*}{\kappa} = \frac{q}{\kappa L_{ins}}$$

$$\pi_{15} = \frac{\kappa'_{ob}}{\kappa} \qquad \pi_{16} = \frac{\kappa'_{ub}}{\kappa}$$

$$\pi_{17} = c_f\, p_i \qquad \pi_{18} = \frac{T_{inj}}{T_{avg}}$$

$$\pi_{19} = \frac{\tau \sin\alpha_X \cos\alpha_Y (L_{prod} + L_{ins} + L_{inj})}{T_{avg}}$$

and the thermal dimensionless time based on the energy equation is:

$$t_D = \frac{\rho_f C_f}{(\phi \rho_f C_f + (1-\phi)\rho_r C_r)} \frac{q\,t}{(L_{prod} + L_{ins} + L_{inj}) L_{ins} H} \tag{5.18}$$

All of these dimensionless numbers are necessary for making the ZMW partial differential equations dimensionless; however their form can be heuristically manipulated to obtain desired or meaningful ones.

5.5 Explaining dimensionless groups

Many of these dimensionless numbers have analogous counterparts in the line drive system. π_1 is the ratio of total compressibility to fluid compressibility, π_2 is the ratio of total expansivity to fluid expansivity. $\pi_3 = M = (\rho_m C_{pm})/(\rho_f C_{pf})$ is the matrix to fluid heat capacity ratio in which $\rho_m C_{pm} = \phi\rho_f C_{pf} + (1-\phi)\rho_r C_{pr}$ (Phillips, 2009). π_4 shows the compressibility of the fluid and π_5 shows the expansivity of the fluid at initial reservoir temperature. π_6 and π_7 show effective aspect ratio in the x and y directions respectively. Unlike the line drive system, these aspect ratio groups are defined by the total length of the horizontal well (i.e. sum of all three sections, π_6) and the insulation length (π_7). The groups π_8 and π_9 represent the dip angle group in the x and y directions respectively. In the line drive system the dip angle group is defined by the distance (i.e. model length) between the injector and the producer. In the ZMW system, the dip angle groups are defined by the total length (π_8) and the insulation length (π_9) of the horizontal well. The groups π_{10}, π_{11} and π_{12} are specific to the ZMW system and show the aspect ratio of the production, injection and insulation sections of the horizontal well, respectively. π_{13} is analogous to the bouyancy number. π_{14} represents the Peclet number for the ZMW system. In the line drive system, a thermal Peclet number is defined by the length between the producer and the injector. In the ZMW system, the Peclet number is defined by the insulation length between the production and the injection sections. The groups π_{15} and π_{16} show the ratio of the conductive heat transfer across the boundary to the conductive heat transfer in the matrix. π_{17} shows the fluid compressibility. π_{18} represents the ratio of injection temperature to the average reservoir temperature. π_{19} scales the temperature difference across the horizontal well to the average reservoir temperature and shows the temperature distribution in the reservoir. The groups π_1, π_2, π_3 are purely rock and fluid

characteristics. Unlike a line drive design, in a ZMW system, many of the dimensionless numbers are operational and are set by the heat exchanger design. The groups π_8, π_9, π_{10}, π_{11} and π_{12} scale the geometry of the horizontal well to that of the reservoir, have no fluid or rock properties in them and are operational. The groups π_4, π_6, π_7, π_{14}, π_{18}, π_{19} are also operational. Chapter 3 provides a more detailed explanation of these dimensionless numbers.

Chapter 6

A model for the ZMW design

In the previous chapter, the dimensionless numbers for a ZMW system were derived analytically and their corresponding model was simulated. In this chapter, a model for predicting dimensionless temperature of a ZMW system is presented. This chapter proceeds with the same flow as Chapter 4. Fifteen reservoir models are considered and their dimensionless numbers are matched to validate their effect on dimensionless temperature. A violin plot is created for quick uncertainty analysis. A relative importance analysis is performed to find the important dimensionless numbers in predicting the response. The reduced final response surface model is presented and its performance is assessed using testing runs.

6.1 Defining the response

Dimensionless production temperature is defined in Chapter 4 as the ratio of the producing fluid temperature to the initial average reservoir temperature. The energy recovery factor at time t_D is defined as the ratio of the cumulative produced energy at that time (i.e. t_D) to the cumulative produced energy at $t_D = 0.5$ (breakthrough time) (Muffler and Cataldi, 1978; Nathenson, 1975; Williams et al., 2008). The reason for this choice is that when temperature gradient is zero, the cumulative produced energy before breakthrough can be directly calculated using the initial reservoir temperature. Using the model for the thermal recovery factor, cumulative produced energy can be directly calculated at any dimensionless time. Produced energy is (Eq. 6.1):

$$\begin{aligned} Produced\,energy =& q \int_0^t \rho_f C_{pf} (T_{prod} - T_0) d\tau \\ =& q \int_0^{t_D} \rho_f C_{pf} (T_D T_{avg} - T_0) (\frac{M(\Sigma L) L_{ins} H}{q}) d\tau_D \end{aligned} \tag{6.1}$$

$$= \big(M(\Sigma L)L_{ins}H\big)(\rho_f C_{pf})_{avg} \int_0^{t_D} (T_D T_{avg} - T_0) d\tau_D$$

in which T_0 is the reference temperature (i.e. 25 C) and ΣL is the total length of the horizontal well (i.e. $L_{inj} + L_{ins} + L_{prod}$). $\rho_f C_{pf}$ changes slightly and can be averaged out of the integral. Before $t_D = 0.5$, $T_D = 1$ thus the thermal recovery factor is (Eq. 6.22):

$$RF = \frac{\big(M(\Sigma L)L_{ins}H\big) \int_0^{t_D} (\rho_f C_{pf})(T_D T_{avg} - T_0) d\tau_D}{0.5 \times \big(M(\Sigma L)L_{ins}H\big)(\rho_f C_{pf})(T_{avg} - T_0)} \tag{6.2}$$

The above integral can be evaluated using a model for the dimensionless production temperature. However, using the simulator output directly and regressing the thermal recovery factor versus dimensionless time results in a simpler model. The latter approach is presented in this chapter.

6.2 Validating the scaling groups

Similar to the Chapter 4, matching the dimensionless numbers gives similar dimensionless results. For confirming the dimensionless numbers, the parameters in the groups are changed while the groups are held constant. Fifteen different models were considered such that their geometrical dimensional properties are different but their dimensionless groups are identical (Appendix D). The dimensionless temperature and thermal recovery factor was then plotted versus dimensionless time. Matching the cases where the parameters have been changed but their group values remain the same would suggest that the dimensionless numbers adequately scale the system. The dimensional result vs. time for these fifteen models do not show any pattern (Figures 6.1a and 6.2a). The dimensionless results are plotted versus dimensionless time for the same models (Figures 6.1b and 6.2b). The reservoir models with identical dimensionless numbers (i.e. the same color) show the same dimensionless temperature or thermal recovery factor in the dimensionless space.

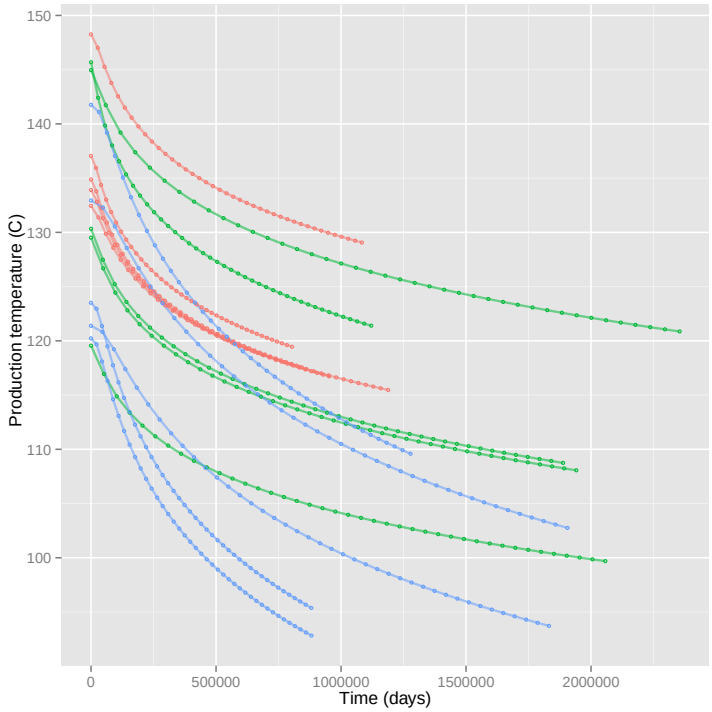

(a) Production temperature vs. time

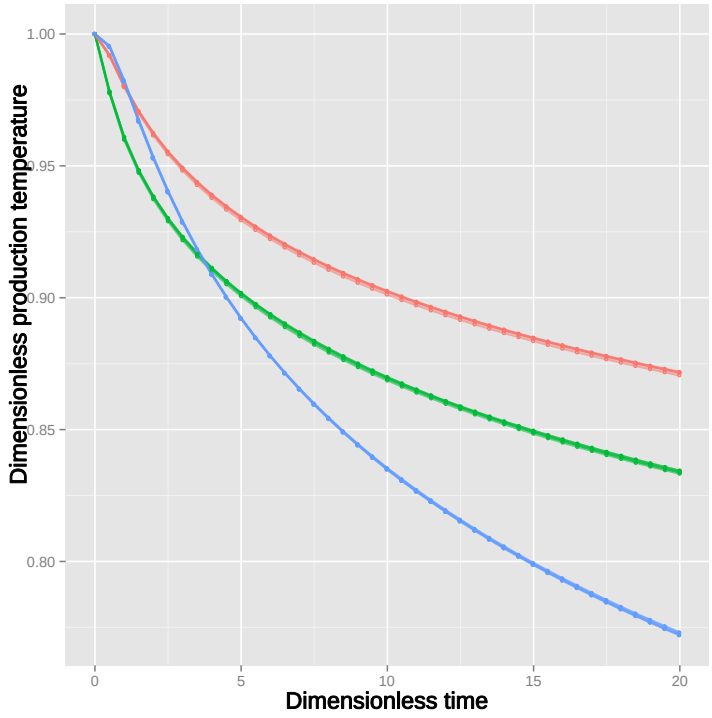

(b) Dimensionless production temperature vs. dimensionless time

Figure 6.1: Testing the dimensionless numbers. Reservoir models with the same dimensionless numbers (same color) show different temperature drop but similar dimensionless temperature.

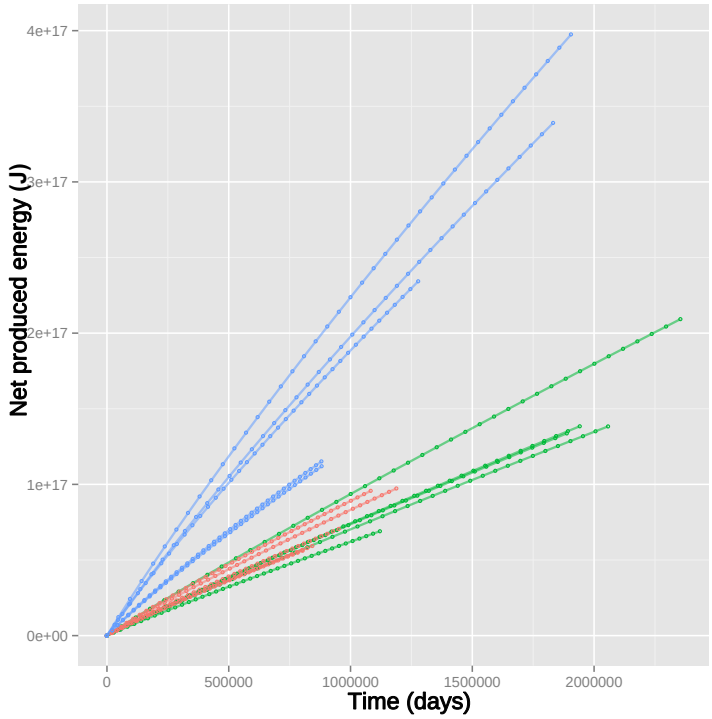

(a) Produced energy vs. time

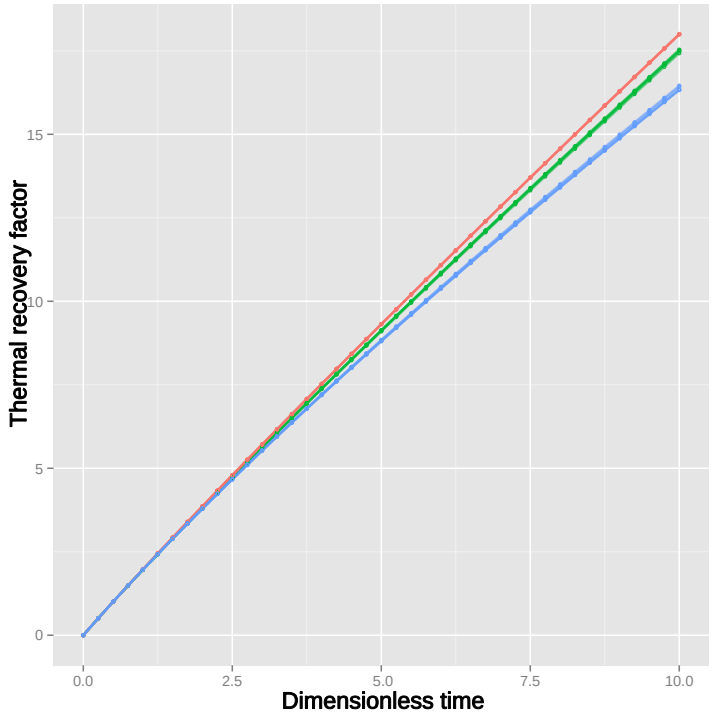

(b) Thermal recovery factor vs. dimensionless time

Figure 6.2: Testing the dimensionless numbers. Reservoir models with the same dimensionless numbers (same color) show different produced energy vs. time but similar thermal recovery factor vs. dimensionless time.

6.3 Modeling production temperature

6.3.1 Box-Behnken design

Twenty one parameters are used in the Box-Behnken design. The numerical model was described in Chapter 5. Temperature gradient is neglected for this study to simplify the results at early time. Temperature gradient increases the production temperature above the average reservoir temperature (i.e. $T_D > 1$) because the production section of the horizontal well draws water from the hotter sections of the reservoir at early time. This effect does not need to be considered after the breakthrough time when the cool front reaches the production well. The Box-Behnken design required 841 runs. These runs were divided into 20 parallel runs per batch submission and required ca. 85 minutes to complete.

6.3.2 Uncertainty analysis

Figure 6.3 presents a violin uncertainty plot for the dimensionless production temperature. At early time ($0 < t_D < 2.5$), dimensionless temperature reduces rapidly and its range of uncertainty (black thin line) remains low. At late times, the dimensionless temperature approaches a value between 0.6 and 0.7 asymptotically and its range of uncertainty increases. Section 6.4.1 presents an application of this plot. Violin plots and their use in segmenting the dimensionless time were discussed in Section 4.4.2. Five ranges for segmenting the model are considered: $0 \leq t_D \leq 0.5$, $0.5 < t_D \leq 2.5$, $2.5 < t_D \leq 5$, $5 < t_D \leq 10$ and $10 < t_D \leq 20$ (Figure 6.4).

6.3.3 Relative importance analysis

Table 6.1 shows the ranges of the dimensionless numbers used in the sensitivity analysis. Dimensionless numbers can be rank-ordered based on their relative importance in predicting the dimensionless temperature using the Boosting algorithm (Figure 6.5). Dimensionless time is the most important factor in determining dimensionless production temperature at early times. However, at later times, temperature ratio (π_{18}) and Peclet number (π_{14}) become more important. Dip angle group (π_8), dimensionless production (π_{10}) and injec-

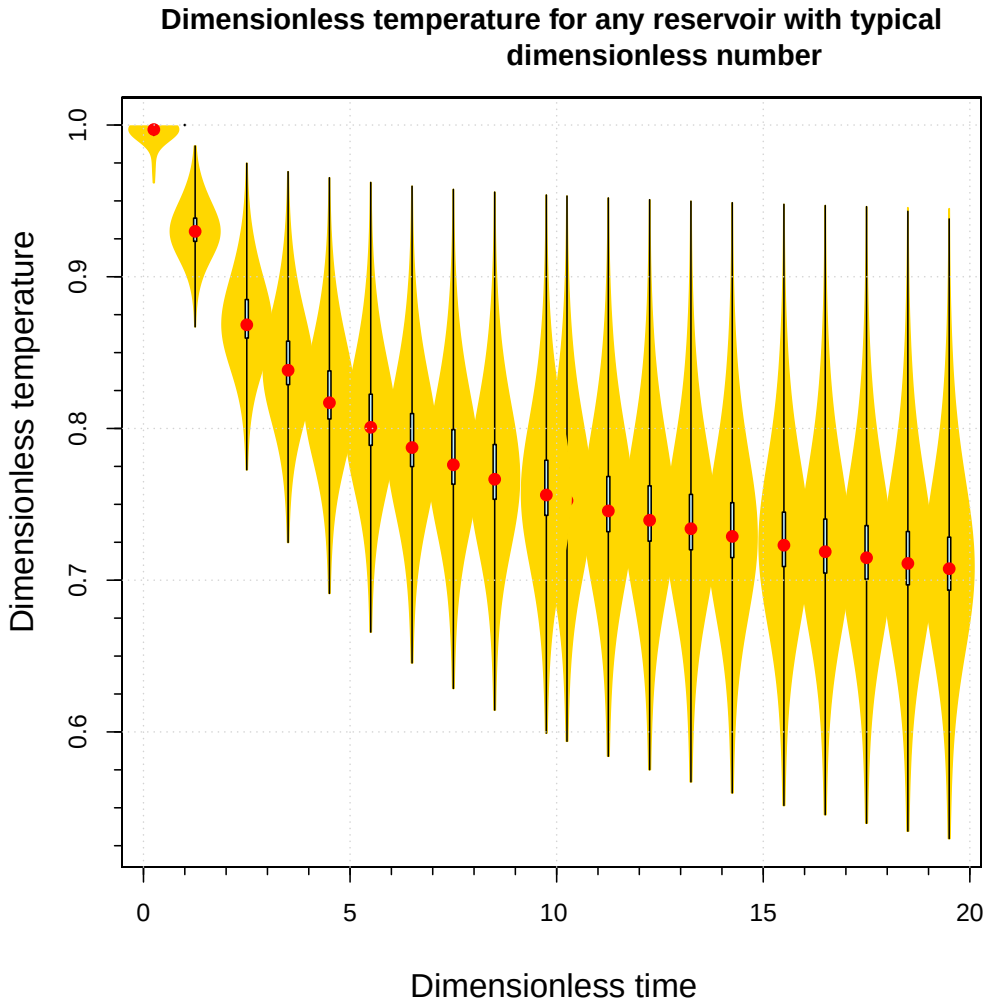

Figure 6.3: Violin plot for assessing the uncertainty of dimensionless production temperature.

tion length (π_{11}) are other important dimensionless numbers. This transition in relative importance is smooth and happens over time. The dimensionless numbers which do not affect the response can be safely disregarded for prediction. Dimensionless numbers with less than 1% relative importance were ignored. Finding these important dimensionless numbers is also very useful in the validation process (previous section). Reservoirs with identical important dimensionless numbers show similar behavior in the dimensionless space. Before proceeding to the model selection, it is a good practice to check the correlation between the dimensionless numbers to prevent ill-conditioned or singular matrices.

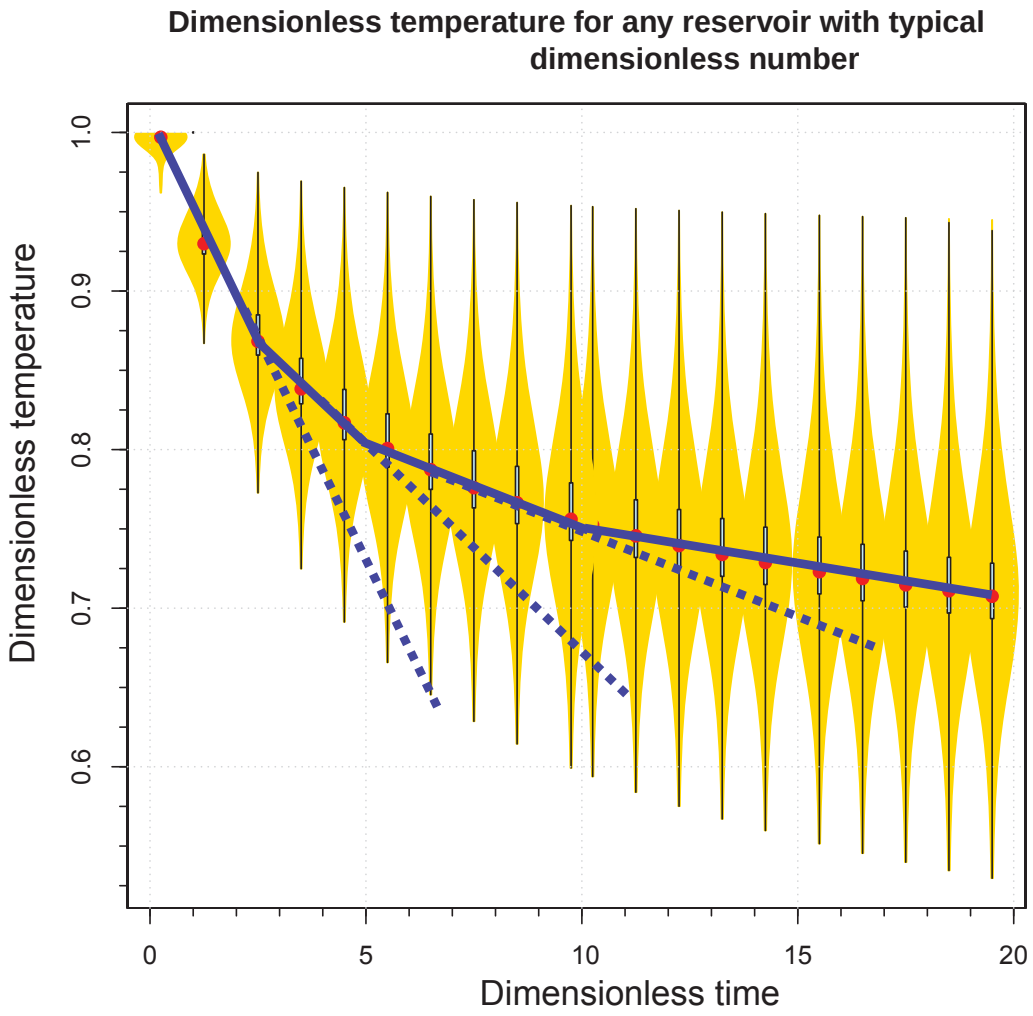

Figure 6.4: Five ranges for segmenting the model are considered: $0 \leq t_D \leq 0.5$, $0.5 < t_D \leq 2.5$, $2.5 < t_D \leq 5$, $5 < t_D \leq 10$ and $10 < t_D \leq 20$. The blue lines are sketched manually.

6.3.4 Correlation

Because the definition of the dimensionless numbers are heuristic and flexible, seeing their relation is useful to prevent collinearity or regression divergence. Figure 6.6 shows the correlation between the important dimensionless numbers for different values of dimensionless time. In the upper triangle of each sub-figure, the strength of the correlation is represented by the filled area. Positive correlation is blue and fills the pie clockwise while negative correlation is red and fills the pie counterclockwise. The lower triangle show similar information by the shape and direction of ellipses. As the correlation between two dimensionless numbers decreases, the ellipse shape becomes more circular. The lines in

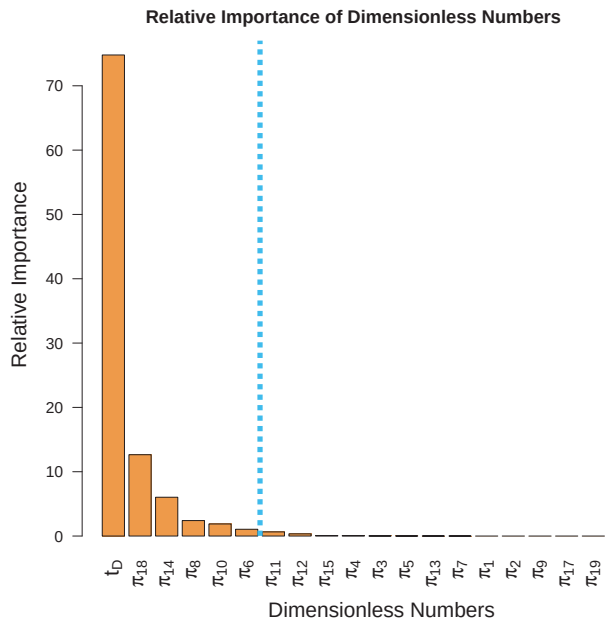

(a) Important dimensionless numbers for the range $0.5 < t_D \leq 2.5$

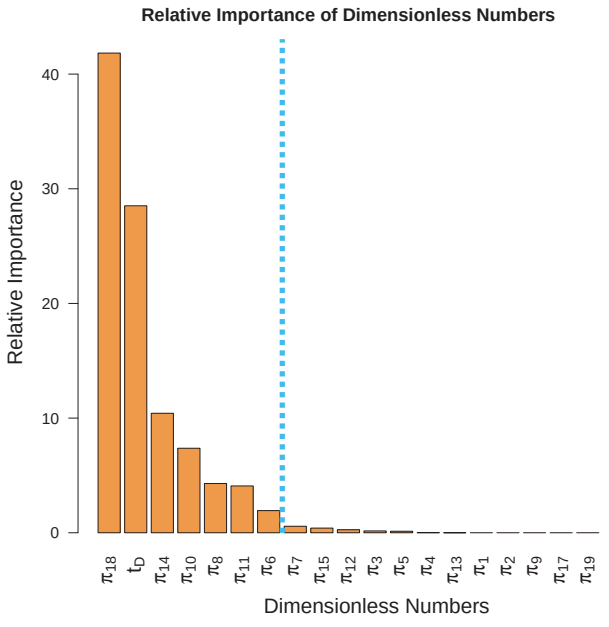

(b) Important dimensionless numbers for the range $2.5 < t_D \leq 5$

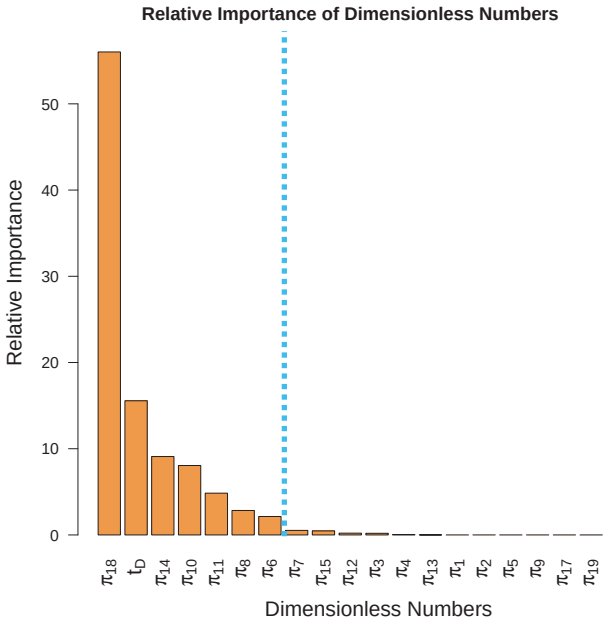

(c) Important dimensionless numbers for the range $5 < t_D \leq 10$

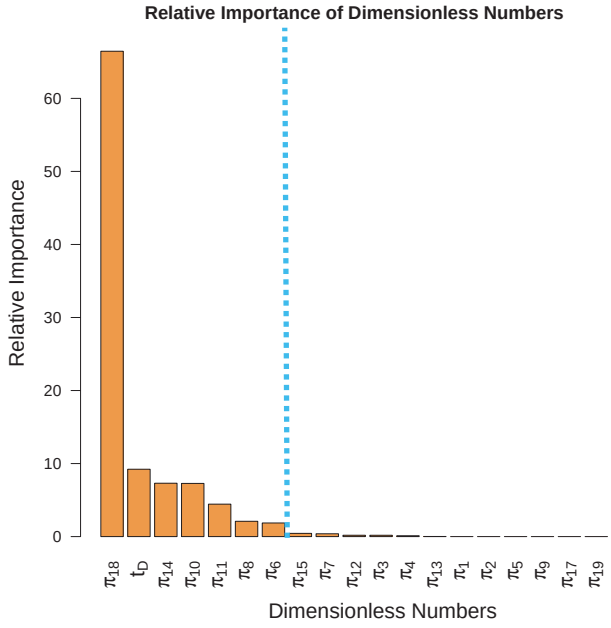

(d) Important dimensionless numbers for the range $10 < t_D \leq 20$

Figure 6.5: Important dimensionless numbers for each range of the dimensionless time. The cyan line shows the cut off for the dimensionless numbers with less than 1% importance.

Table 6.1: Ranges of dimensionless numbers used for sensitvitiy analysis. Other dimensionless numbers are held constant for this study.

Group	π_1	π_2	π_3	π_4	π_5	π_6	π_7	π_8	π_{10}	π_{11}
Low	0.21	0.155	0.46	0.0001448	0.060	2.18	0.31	0.3	0.57	0.57
High	1.05	0.45	0.73	0.0063	0.167	36.25	14.95	16.9	21.15	21.1

Group	π_{12}	π_{13}	π_{14}	π_{15}	π_{17}	π_{18}
Low	0.57	14.66	16.91	0.45	0.024	0.189
High	21.1	1483.2	473.4	1.21	0.040	0.897

the confidence ellipses show best fit lines between dimensionless numbers. Jagged lines indicate a sparsity of data. As this figure indicates, the correlation between the dimensionless predictors are all less than 0.8 and there was no multicollinearity problem for this set of predictors. Predictors can be omitted, combined or reformed if they are multicollinear (Montgomery et al., 2012). The response's (T_D) correlation with dimensionless time decreases and its correlation with temperature ratio increases. π_{10} has correlation with π_{11} because reservoir thickness (H) exists in the denominator of both numbers. π_8 correlation with π_{10} and π_{11} is similar and more than the correlation between π_{10} and π_{11} because of the structure of these groups. Figure 6.6 confirms Figure 6.5. Correlation between the dimensionless time and the dimensionless temperature decreases at late times (See Figure 6.3 and 6.5). The correlation between π_{18} and the dimensionless temperature increases at late times when the system's dimensionless temperature is approaching a constant value asymptotically (See Figure 6.3).

6.3.5 Model selection

The model was fit using eighty values for dimensionless time with step size of $t_D = 0.25$ (i.e. t_D values of 0.25, 0.5, ..., 20). A segmented (piecewise) regression is used to model dimensionless production temperature using all 841 runs. Note that this means that the first segment ($0 \leq t_D \leq 0.5$) has 3 values for dimensionless time (841×3 samples points), the second segment ($0.5 < t_D \leq 2.5$) has 9 values for dimensionless time (841×9 samples points), the third segment has 10 values (841×10 samples points), the fourth segment

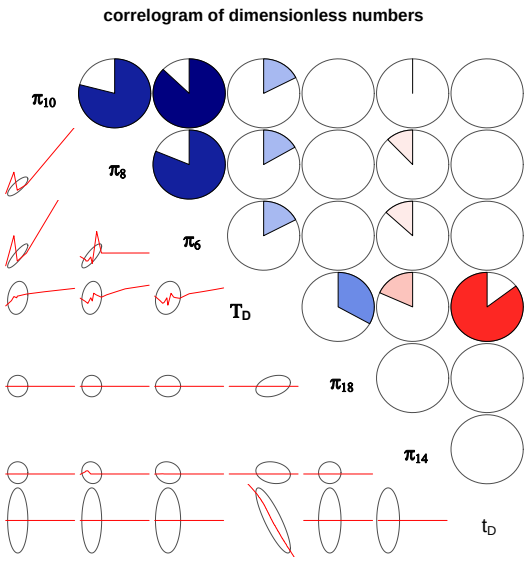

(a) $0.5 < t_D \leq 2.5$.

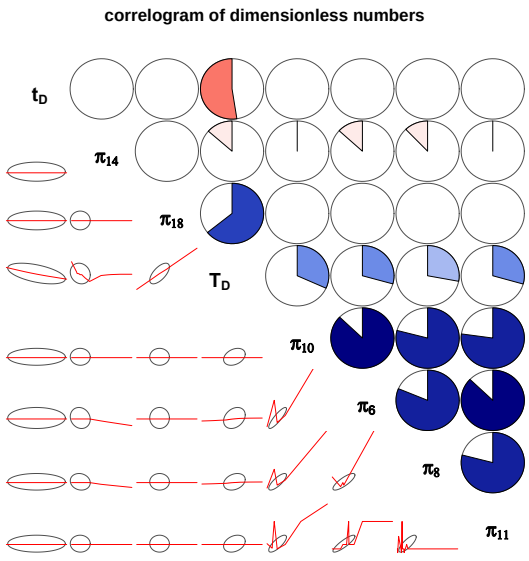

(b) $2.5 < t_D \leq 5$

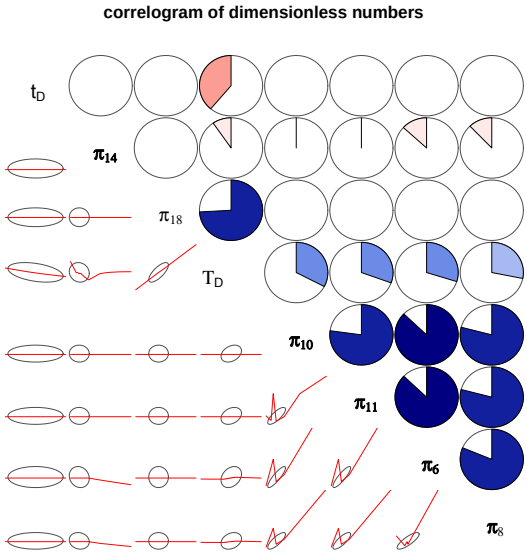

(c) $5 < t_D \leq 10$.

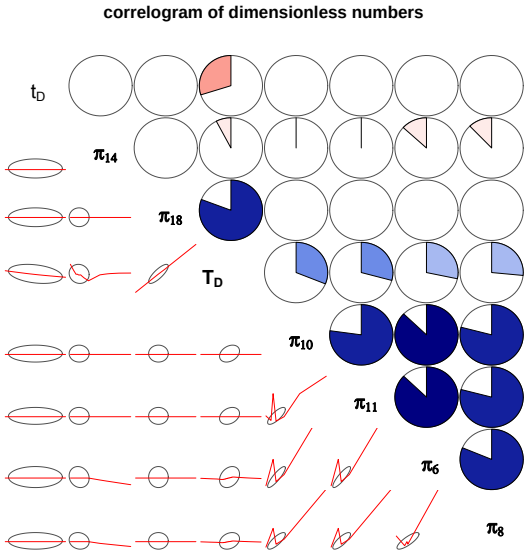

(d) $10 < t_D \leq 20$.

Figure 6.6: Correlation between dimensionless numbers at each range of dimensionless time. Correlation between response and factors changes with dimensionless time.

($5 < t_D \leq 10$) has twenty (841×20 points) and the fifth segment ($10 < t_D \leq 20$) has forty values for dimensionless time (841×40 points). Using an "all subset regression" procedure, possible sub-models are investigated (see section 4.4.4). In Figure 6.7, the black area shows the presence of a predictor and the y axis shows the R^2 value associated with that model. The best model for segment (a) has an R^2 value of 0.9398, the best model for segment (b) has an R^2 value of 0.8976, the best model for segment (c) has an R^2 value of 0.903 and the best model for case (d) has an R^2 value of 0.9166. These selected models for dimensionless production temperature are presented in Box 3.

6.3.6 Model assessment

Figure 6.8 shows the assessment of the reduced final model. In each sub-figure 786 runs were used for training and 55 runs for testing. This means 7,074 (i.e. 786×9) training samples (blue points) and 495 (i.e. 55×9) testing samples (red points) were used for the second segment, 7,860 (i.e. 786×10) training samples and 550 testing samples were used for the third segment, 15,720 training samples and 1,100 testing samples were used for the fourth segment and 31,440 training and 2,200 testing samples were used for the fifth segment.

6.4 Modeling thermal Recovery factor

The procedure that was used in the previous sections is used to model thermal recovery factor. First the violin plot is created (Figure 6.9) to determine how many piecewise regression models are needed and to specify their dimensionless time ranges (Figure 6.10). Then a sensitivity analysis is performed to find the important dimensionless numbers in predicting the response for each dimensionless time segment (Figure 6.11). The models are reduced by comparing their R^2 values and the final simple model is presented (Figure 6.12, Box 4). At the last step, these reduced models are assessed to observe their performance (Figure 6.13).

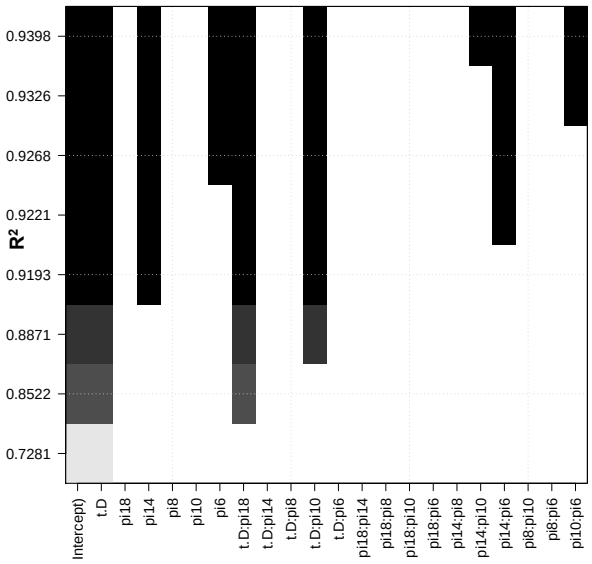

(a) $0.5 < t_D \leq 2.5$.

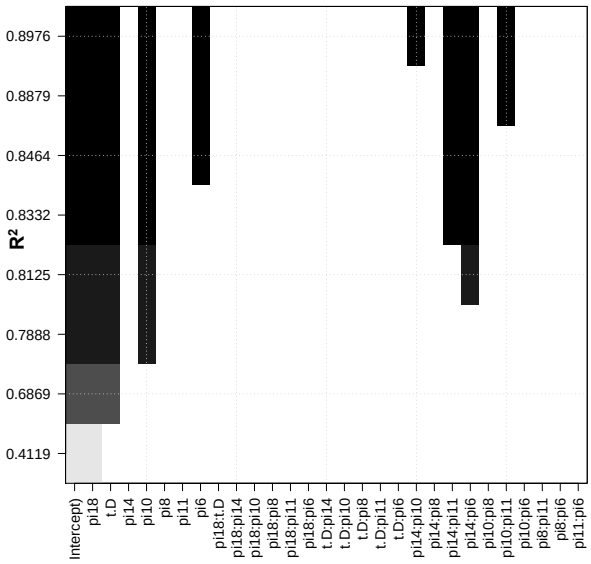

(b) $2.5 < t_D \leq 5$

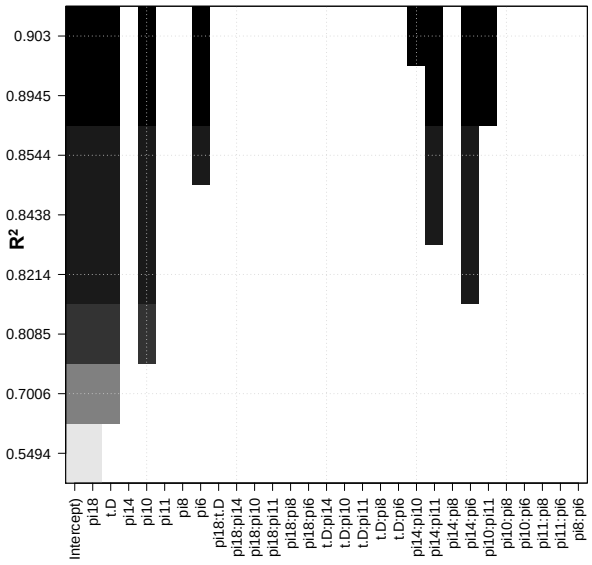

(c) $5 < t_D \leq 10$.

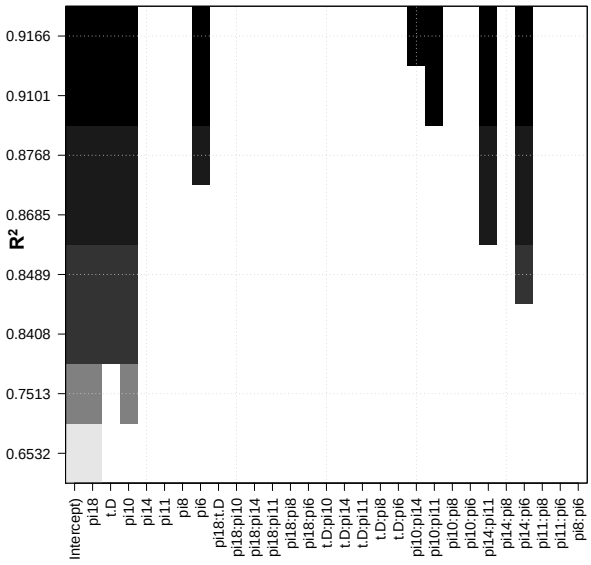

(d) $10 < t_D \leq 20$.

Figure 6.7: Reducing the models for production temperature at each range of dimensionless time.

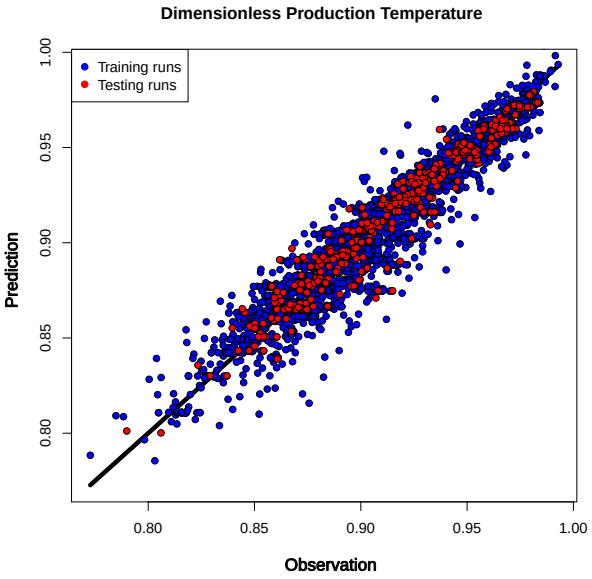

(a) $0.5 < t_D \leq 2.5$

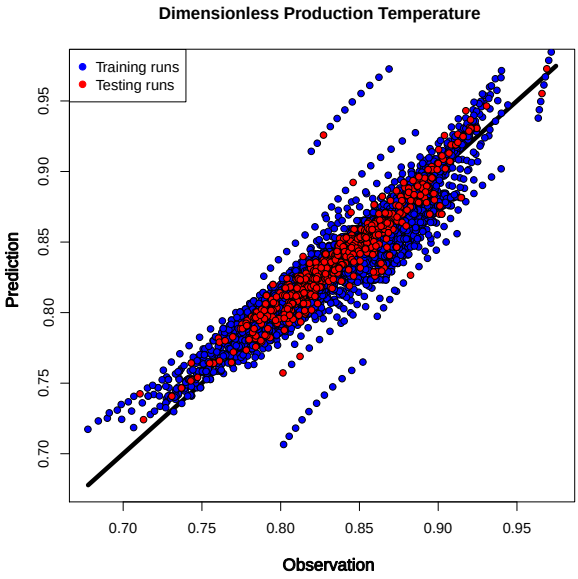

(b) $2.5 < t_D \leq 5$

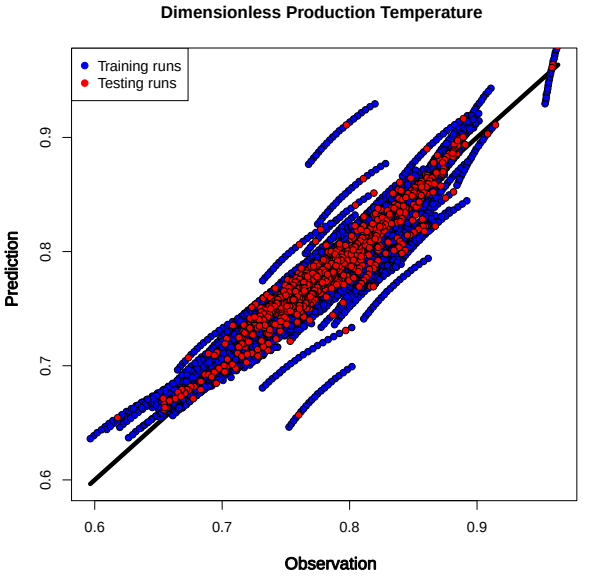

(c) $5 < t_D \leq 10$

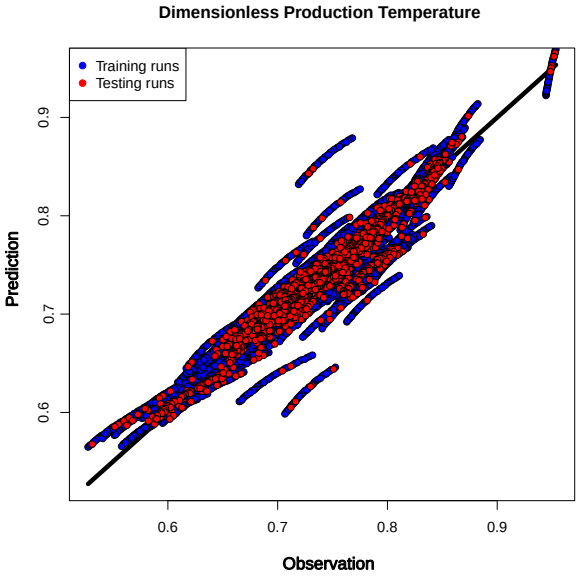

(d) $10 < t_D \leq 20$

Figure 6.8: Assessing the models for the dimensionless production temperature

Box 3: Proposed model for dimensionless production temperature

For $0 \leq t_D \leq 0.5$, we have:

$$T_D = 1 \tag{6.3}$$

For $0.5 \leq t_D \leq 2.5$, we have:

$$\begin{aligned} T_D =& 0.9782 - 0.1051 t_D + 0.0001\pi_{14} + 0.0059\pi_6 + 0.0963 t_D \pi_{18} + 0.0018 t_D \pi_{10} \\ &+ 0.0001\pi_{14}\pi_{10} - 0.0001\pi_{14}\pi_6 - 0.0002\pi_6\pi_{10} \end{aligned} \tag{6.4}$$

For $2.5 < t_D \leq 5$, we have:

$$\begin{aligned} T_D =& 0.7284 + 0.2924\pi_{18} - 0.0234 t_D + 0.0059\pi_{10} + 0.0101\pi_6 \\ &+ 0.0001\pi_{10}\pi_{14} + 0.0001\pi_{14}\pi_{11} - 0.0002\pi_6\pi_{14} - 0.001\pi_{10}\pi_{11} \end{aligned} \tag{6.5}$$

For $5 < t_D \leq 10$, we have:

$$\begin{aligned} T_D =& 0.6057 - 0.0106 t_D + 0.3952\pi_{18} + 0.0112\pi_6 + 0.0073\pi_{10} \\ &+ 0.0001\pi_{10}\pi_{14} + 0.0002\pi_{14}\pi_{11} - 0.0002\pi_6\pi_{14} - 0.0011\pi_{10}\pi_{11} \end{aligned} \tag{6.6}$$

and for $10 < t_D \leq 20$, we have:

$$\begin{aligned} T_D =& 0.5004 - 0.0047 t_D + 0.0081\pi_{10} + 0.4878\pi_{18} + 0.0113\pi_6 \\ &+ 0.0001\pi_{10}\pi_{14} + 0.0002\pi_{14}\pi_{11} - 0.0002\pi_6\pi_{14} - 0.0011\pi_{11}\pi_{10} \end{aligned} \tag{6.7}$$

After squeezing all the runs into a single violin plot (Figure 6.9), it is observed that two piecewise regression models can sufficiently predict the response. The ranges of the first and second models are $0 < t_D \leq 5$ and $5 < t_D \leq 20$ respectively (Figure 6.10).

A sensitivity analysis was performed to find the important dimensionless numbers in predicting the response (Figure 6.11). For $0 \leq t_D \leq 5$, dimensionless time is the only

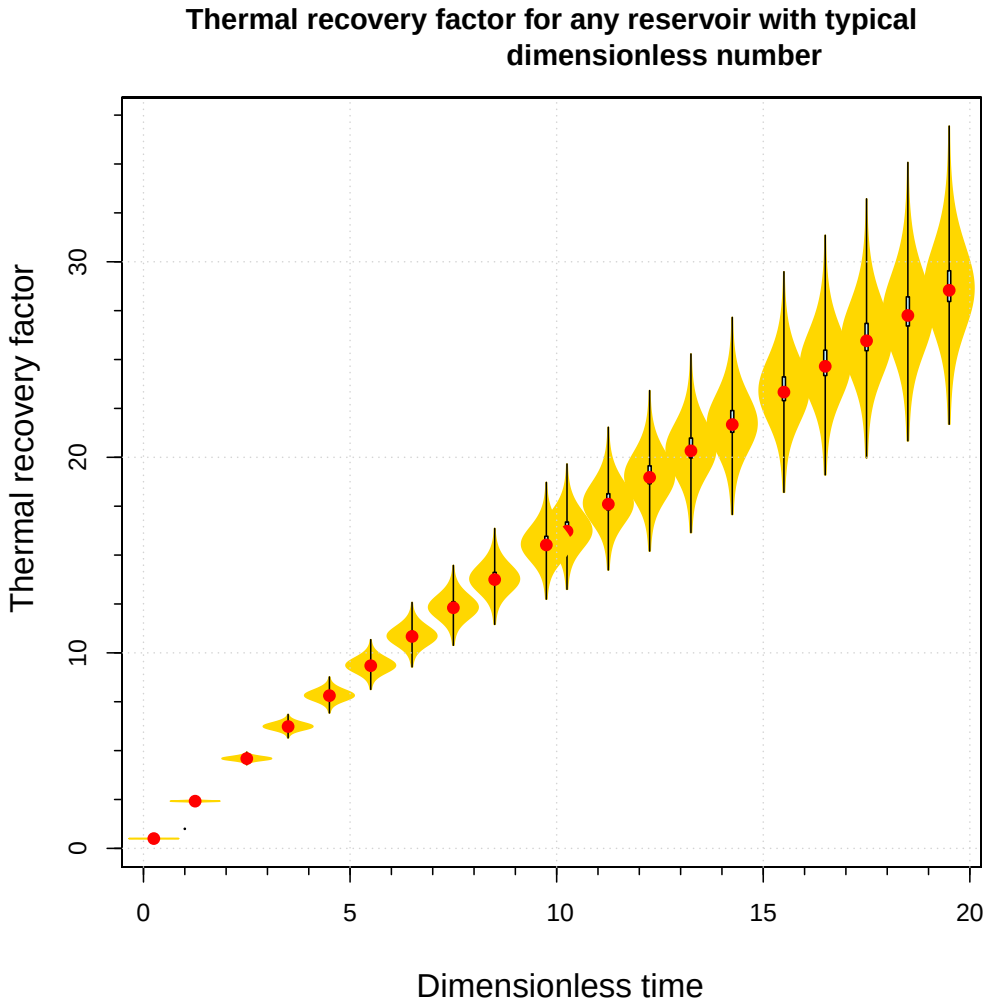

Figure 6.9: Violin plot for calculating thermal recovery factor of uncertain reservoirs.

predictor that is needed and for $5 < t_D \leq 20$, dimensionless time and temperature ratio (π_{18}) are needed for predicting the thermal recovery factor.

These important dimensionless numbers were used for developing a model for the thermal recovery factor. Figure 6.12 compares the R^2 values of all subset regression models. An R^2 value of 0.9881 was chosen for the best model. The simplified models for energy recovery factor are presented in Box 4. At the last step, the reduced models (Box 4) are assessed using 786 training and 55 testing runs (Figure 6.13).

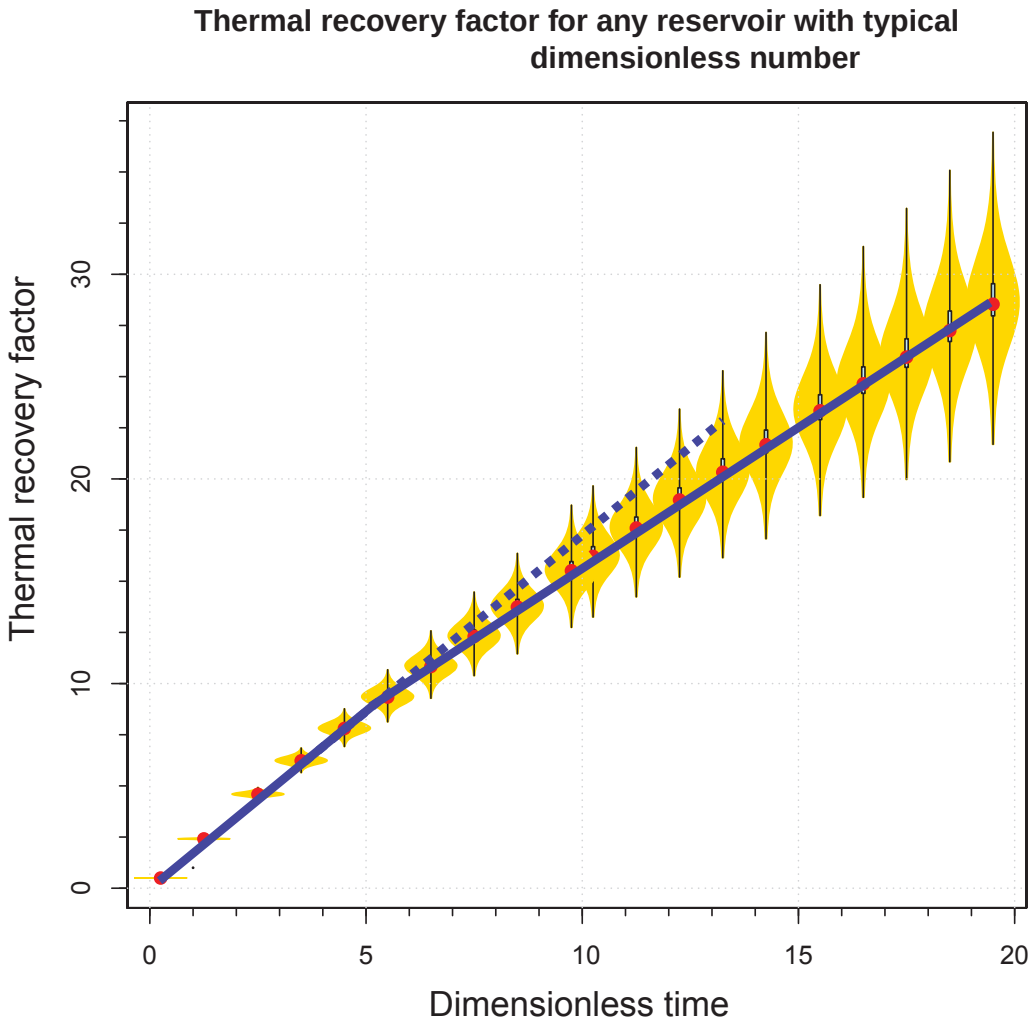

Figure 6.10: Two ranges for segmenting the model are considered: $0 < t_D \leq 5$ and $5 < t_D \leq 20$. The blue lines are sketched manually.

Box 4: Proposed model for thermal recovery factor

For $0 \leq t_D \leq 5$, we have:

$$RF = 1.7742 t_D \tag{6.8}$$

and for $5 < t_D \leq 20$, we have:

$$RF = 3.6441 + 0.8895 t_D - 3.5367 \pi_{18} + 1.081 t_D \pi_{18} \tag{6.9}$$

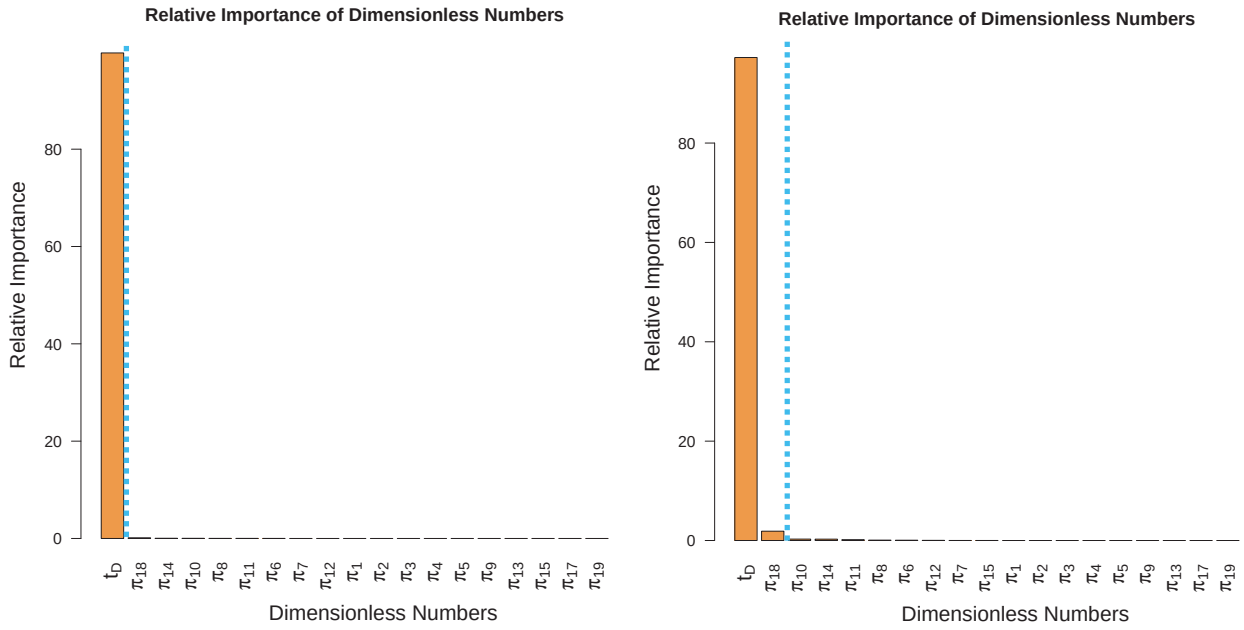

(a) $0 < t_D \leq 5$ (b) $5 < t_D \leq 20$

Figure 6.11: Important dimensionless numbers for predicting thermal recovery factor. The cyan line shows the cut off for the dimensionless numbers with less than 1% importance.

6.4.1 Applications

In the following some applications of the developed models are discussed. A reservoir with some unknown data is described in the Question A and the uncertainty in its temperature is calculated. Questions 2 and 3 use the developed models to calculate these values for the same reservoir.

Question 1) Consider a ZMW system with a production, injection and insulation length of 200 m each. The production section can provide a rate of 1000 m^3/day, all of which is injected back into the reservoir from the injection section. We only know that the reservoir's height and porosity are 30 m and 0.2, respectively. Other information about the reservoir (e.g average temperature, injection temperature and rock thermal conductivity, etc) are unknown but they are assumed to be typical (Table 6.1). Quantify the uncertainty in the production temperature after 30 years of production?

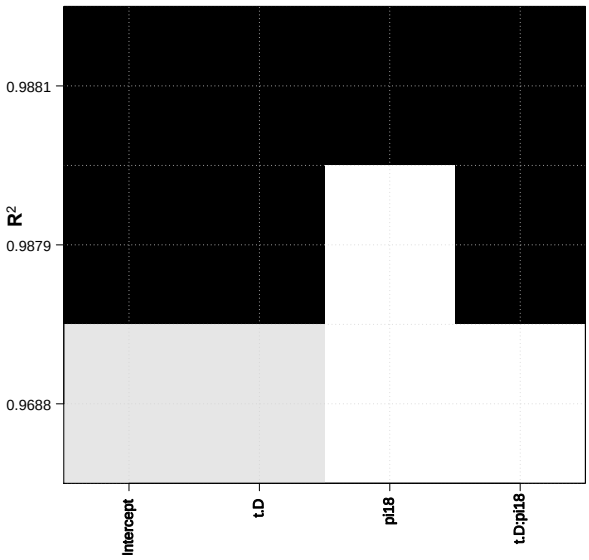

Figure 6.12: R^2 values of different models for thermal recovery factor for $5 < t_D \leq 20$.

Answer) Typical values for rock and water volumetric heat capacities are 2×10^6 J/m^3C and 4×10^6 J/m^3C:

$$\rho_m \, C_{pm} = 2.4 \times 10^6 \, J/m^3C \tag{6.10}$$

$$M = \frac{\rho_m C_{pm}}{\rho_f C_{pf}} = \frac{2.4 \times 10^6}{4 \times 10^6} = 0.6 \tag{6.11}$$

$$t_D = \frac{1}{M} \frac{q\,t}{(L_{prod} + L_{ins} + L_{inj}) L_{ins} H} = \frac{1}{0.6} \frac{1000 \, \frac{m^3}{day} \times 30 \, years}{600 \times 200 \times 30 \, m^3} = 5.07 \tag{6.12}$$

Using Figure 6.3, maximum, median and minimum dimensionless temperature for this reservoir after 30 years of production are ca. 0.96, 0.81 and 0.68 respectively.

Question 2) For the reservoir in the Question 1, if initial average reservoir temperature is 120 C and injection temperature is 80 C, find the uncertainty in the energy production rate after 30 years?

The volumetric heat capacity of water at 90 C is 4.05×10^6 J/m^3C. Using the dimensionless temperature values, maximum, median and minimum production temperature are 115.2, 97.2 and 81.6 C respectively.

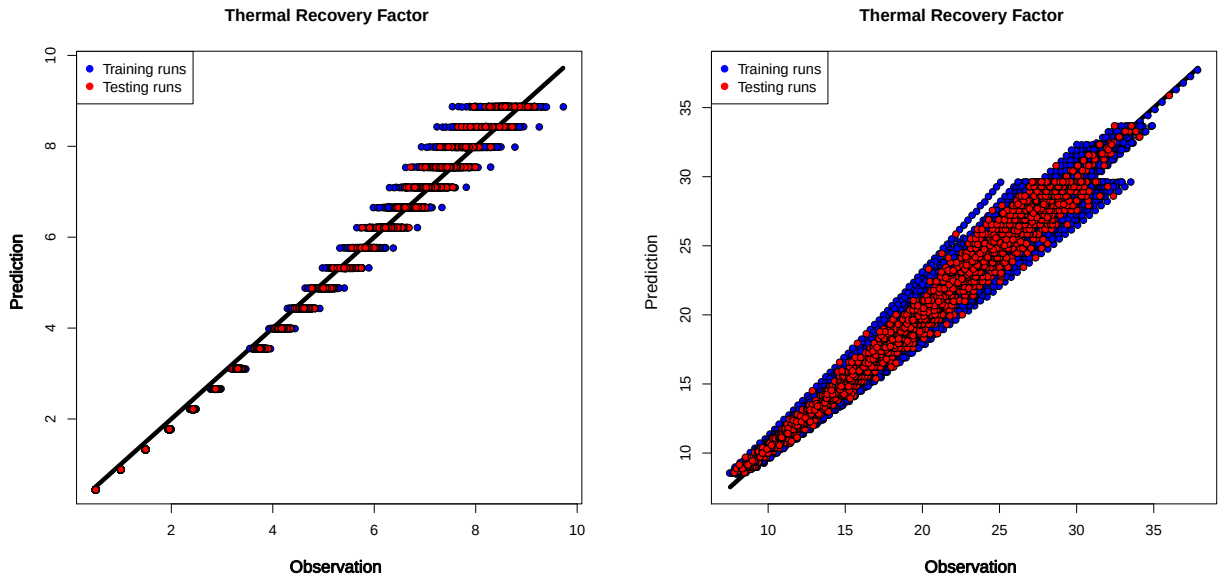

(a) Assessment of the model for $0 \leq t_D \leq 5$ (b) Assessment of the model for $5 < t_D \leq 20$

Figure 6.13: Model assessment for thermal recovery factor.

$$\dot{H} = q\rho_f \, C_{pf} \, (T_{prod} - T_{inj}) \tag{6.13}$$

Using Eq. 6.13, maximum, median and minimum energy production rate are 1.43×10^{11} (1.65 MW), 6.966×10^{10} (0.8 MW) and 6.48×10^{9} J/day (0.075 MW) respectively.

Question 3) Assume a thermal conductivity of 2.5×10^5 $J/(m\,day\,C)$ and dip angle of zero for the homogeneous reservoir in the Question 1 and calculate the production temperature and cumulative produced energy after 30 years using the developed model (assume $\frac{k_z}{k_y} = \frac{k_z}{k_x} = 0.1$)?

$$\pi_8 = \frac{(L_{prod} + L_{ins} + L_{inj})}{H} \tan(\alpha_X) = 0 \tag{6.14}$$

$$\pi_{10} = \frac{L_{prod}}{H} = 6.67 \tag{6.15}$$

$$\pi_{11} = \frac{L_{inj}}{H} = 6.67 \tag{6.16}$$

$$\kappa = \frac{\lambda_m}{\rho_f C_{pf}} = \frac{2.5 \times 10^5}{4 \times 10^6} = 0.0625 \tag{6.17}$$

$$\pi_{14} = \frac{u^*_{x1} z^*_1}{\kappa} = \frac{q}{\kappa L_{ins}} = \frac{1000}{0.0625 \times 200} = 80 \tag{6.18}$$

$$\pi_{18} = \frac{T_{inj}}{T_{avg}} = 0.667 \tag{6.19}$$

$$\pi_6 = \frac{L_{prod} + L_{ins} + L_{inj}}{H} \sqrt{\frac{k_z}{k_x}} = 6.32 \tag{6.20}$$

$$\pi_7 = \frac{L_{ins}}{H} \sqrt{\frac{k_z}{k_y}} = 2.11 \tag{6.21}$$

For $5< t_D \leq 10$, we have:

$$\begin{aligned} T_D \ =& 0.6057 - 0.0106 t_D + 0.3952 \pi_{18} + 0.0112 \pi_6 + 0.0073 \pi_{10} \\ &+ 0.0001 \pi_{10} \pi_{14} + 0.0002 \pi_{14} \pi_{11} - 0.0002 \pi_6 \pi_{14} - 0.0011 \pi_{10} \pi_{11} = 0.945 \end{aligned}$$

Thus the production temperature after 30 years of production is 113.4 C.

$$RF \ = 3.6441 + 0.8895 t_D - 3.5367 \pi_{18} + 1.081 t_D \pi_{18} = 9.45$$

$$RF = \frac{\big(M(\Sigma L) L_{ins} H\big) \int_0^{t_D} (\rho_f C_{pf})(T_D T_{avg}) d\tau_D}{0.5 \times \big(M(\Sigma L) L_{ins} H\big)(\rho_f C_{pf})(T_{avg})} \tag{6.22}$$

The cumulative produced energy at $t_D = 0.5$ is:

$$\begin{aligned} H(t_D = 0.5) =& 0.5 \times \big(M(\Sigma L) L_{ins} H\big)(\rho_f C_{pf})(T_{avg} - T_0) = \\ & 0.5 \times 0.6 \times 600 \times 200 \times 30 \times 4 \times 10^6 \times (120 - 25) = \\ & 4.1 \times 10^{14} \, J \end{aligned} \tag{6.23}$$

Thus the cumulative produced energy after 30 years is 3.87×10^{15} J.

If in a ZMW system, the injection temperature changes with time and instead $\Delta T = (T_{prod} - T_{inj})$ remains constant, the production temperature would be less and the net produced energy would be more than the values calculated here.

Chapter 7

Field case studies

Decisions on the location of the injection and production wells are important for estimating energy recovery. In this chapter, an optimization algorithm is used to select the best location for the injectors and producers in the Gueydan field. Then the results are presented and discussed[1]. From the Gueydan field case, we conclude that the temperature map should be used as the primary pre-development guideline for placing the injectors and producers. We use this conclusion to come up with a scheme for the Sweet Lake reservoir. At the end, the results of the Sweet Lake reservoir simulation are presented.

7.1 Gueydan Dome

This section provides estimates of energy generation using reasonable approximations for the study site, the Camerina A zone of the Gueydan field, Vermilion Parish, Louisiana. Well locations in the field are optimized with net enthalpy recovery for a 30 year project life as the objective function. A subset of existing wells originally drilled for oil exploration purposes are used for modeling geothermal exploitation. The results confirm that injection into cooler areas of the reservoir and producing from hotter regions is the best heat harvesting strategy. The results include simple performance models available for binary power plants. Louisiana geothermal resources, previously viewed as marginal, appear to be feasible targets for geothermal energy production.

Based on the conclusions of Quitzau and Bassiouni (1981) and Griggs (2004), abandoned wells at the top of the Camerina A sand in the Gueydan field (Figure 7.1) are considered as candidates for recompletion as part of a geothermal development program. This study optimizes producer and injector locations to maximize the enthalpy recovery from the reservoir. The number of well combinations for this problem is large and requires

[1]This part of the chapter was presented as "Well Placement Optimization for Maximum Energy Recovery from Hot Saline Aquifers" at the 39th Workshop on Geothermal Reservoir Engineering, Stanford University

many reservoir simulation runs. We select four production and four injection wells out of eleven abandoned wells, which requires 11,550 runs. Such problems require efficient and robust optimization to obtain the solution with a feasible number of simulations.

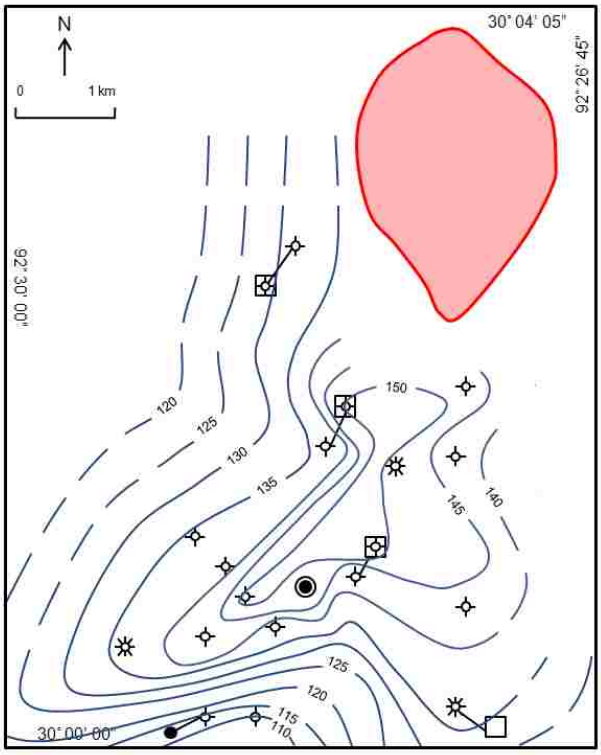

Figure 7.1: Structural map of the Camerina A sand. The red color shows the Gueydan Dome (after Gray and Nunn (2010))

.

7.1.1 Method

Algorithms for well placement optimization problems can be categorized into three groups: gradient-based techniques (Sarma and Chen, 2008; Bangerth et al., 2006; Gharib Shirangi, 2014; Shirangi and Emerick, 2016), proxy methods (Onwunalu et al., 2008; Wang et al., 2012; Ansari, 2013) and global search stochastic algorithms (Tupac et al., 2007; Shirangi and Durlofsky, 2015). Gradient-based optimization methods improve the objective function by stepping the vector of parameters in a direction based on matrices of partial derivatives of the objective function with respect to the parameters. Gradient methods commonly converge to false (local) optima. In the context of geothermal engineering,

Akın et al. (2010) used proxy methods to optimize injection well locations in the Kizildere geothermal field. Proxy models are computationally fast but approximate the objective function using a limited suite of preselected reservoir models. These response models may be inaccurate, particularly for nonlinear and undersampled cases. Onwunalu and Durlofsky (2010) showed the superior performance of particle swarm optimization (PSO; a stochastic global search method) compared with genetic algorithms. Afshari et al. (2011) showed that improved harmony search, another global search method, performs well for well location optimization. However, stochastic algorithms are heuristic and require parameter tuning; it is difficult to reach general conclusions about the best method for any particular case. This study used a particle swarm optimization algorithm (CMOST, 2011) for optimization.

The PSO algorithm is a stochastic population-based optimization method in which each particle is a point (i.e., a candidate solution) in the search space (Eberhart and Kennedy, 1995). The collection of these particles is called a swarm. Particle movement is governed by simple rules, which attempt to avoid local extrema and continue to search the parameter space for the optimal solution.

For an objective function with n parameters to be optimized, a particle is represented by $\mathbf{x}_i(k) = (x_{i,1}(k), x_{i,2}(k), ..., x_{i,n}(k))$ in which i is the number of the particle and k is the iteration. The previous best solution for the i^{th} particle through iteration k is denoted by $\mathbf{x}_i^{pbest}(k)$ and the position of the best particle in the neighborhood of particle i up to iteration k is $\mathbf{x}_i^{nbest}(k)$. A simplified particle swarm case uses one group of particles; thus the global best particle position is the same as the neighborhood best position for all the particles. The i^{th} particle is moved (Eq. 7.1) and its new position is evaluated at iteration k in the parameter space using:

$$\mathbf{x}_i(k+1) = \mathbf{x}_i(k) + \mathbf{v}_i(k+1) \tag{7.1}$$

in which $\mathbf{v}_i(k+1) = (v_{i,1}(k+1), v_{i,2}(k+1), ..., v_{i,n}(k+1))$ represents the parameter-space velocity of the ith particle at the (k+1)th iteration. The velocity vector is calculated using Eq. 7.2:

$$\mathbf{v}_i(k+1) = \omega\left(\mathbf{v}_i(k)\right) + c_1\left(\mathbf{D}_1(k)\left(\mathbf{x}_i^{pbest}(k) - \mathbf{x}_i(k)\right)\right) + c_2\left(\mathbf{D}_2(k)\left(\mathbf{x}_i^{nbest}(k) - \mathbf{x}_i(k)\right)\right) \tag{7.2}$$

in which $\mathbf{D}_i(k)$ are matrices whose diagonal elements are uniformly distributed random variables in the range [0,1], and ω, c_1 and c_2 are weights. The values of ω, c_1 and c_2 are chosen heuristically and depend on the type of the problem. Procedures to optimize these values have been developed for well placement optimization (Onwunalu and Durlofsky, 2010). There are three terms in Eq. 7.2, known as inertia (the term with ω), cognitive (the term with c_1) and social (the term with c_2) respectively. The inertia term assures that the particle velocity is somewhat persistent from one iteration to the next. The cognitive term moves the particle along its own previous best position whereas the social term moves the particle towards the best particle in its neighborhood. These three terms move the particle toward extrema. The inertia term provides a broad exploration of the search space and the cognitive and social terms move the particle towards the best solutions found (up to the current iteration).

The vector sum of the inertia, cognitive and social terms determines the next movement of the particle (two dimensional example, Figure 7.2). In this figure, $\mathbf{v}_i(k)$ is the particle's previous velocity, $\mathbf{v}_i^c(k)$ shows the cognitive velocity from the current position $\mathbf{x}_i(k)$ to the particle's previous best position $\mathbf{x}_i^{pbest}(k)$, and vis(k) is the social velocity from the current position to the current neighborhood best position $\mathbf{x}_i^{nbest}(k)$. The next movement of the i^{th} particle is then calculated by adding the weighted $\mathbf{v}_i(k)$, $\mathbf{v}_i^c(k)$ and $\mathbf{v}_i^s(k)$ vectors.

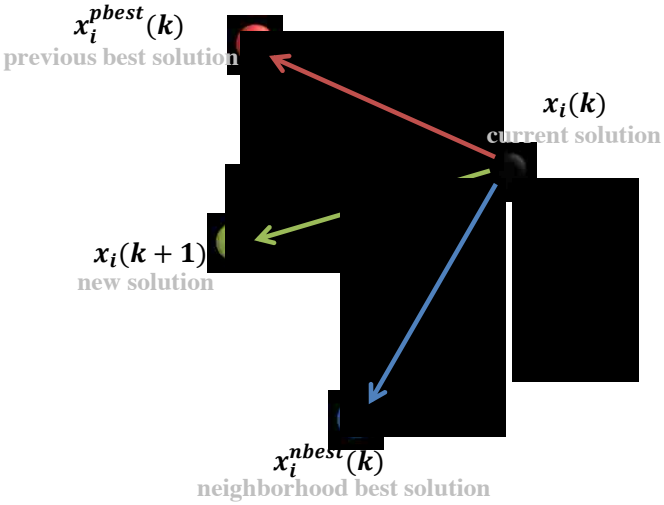

Figure 7.2: PSO algorithm in two-dimensional space. The $(k+1)^{th}$ movement of the i^{th} particle is the vector sum of inertia $\mathbf{v}_i(k)$, cognitive $\mathbf{v}_i^c(k)$ and social $\mathbf{v}_i^s(k)$ components proportional to their coefficients (after (Onwunalu and Durlofsky, 2010)).

7.1.2 Model

The Camerina A geopressured reservoir in the Gueydan field lies between 4200 and 4600 m subsea depth with a dip range from 1.2 to 28 $°C$ on the north and south edges of the four way closure (Figure 7.3, Gray and Nunn (2010)). A shale sequence ranging from 365 to 426 m thick overlies the Camerina A sand and a 150 m shale sequence is below it. The Camerina A structure has a four way closure, with one side bounded by a salt dome. The model does not consider thermal conduction through the salt dome because it does not affect heat production from the Camerina A (Gray and Nunn, 2010). The model uses a corner point grid with dimensions of the x-y-z grid count of $25 \times 32 \times 3$. Each grid block is 200 m on the sides and the thickness of the reservoir is divided into three layers that equally divide the areally varying thickness (the top layer thickness is shown in Figure 7.4).

Homogeneous horizontal and vertical permeabilities are 300 md and 30 md respectively. Thermal conductivity of the cap and base rock, the reservoir rock and water were set to 1.496×10^5, 2×10^5 and 5.35×10^4 $J.m^{-1}.day^{-1}.C^{-1}$ respectively. Thermal capacity of the cap and base rock and the reservoir rock were set to 2.347×10^6 and 1.97×10^6 $J.m^{-3}.C^{-1}$,

respectively and properties of the water (pure H_2O) were calculated from steam tables (STARS manual, 2011).

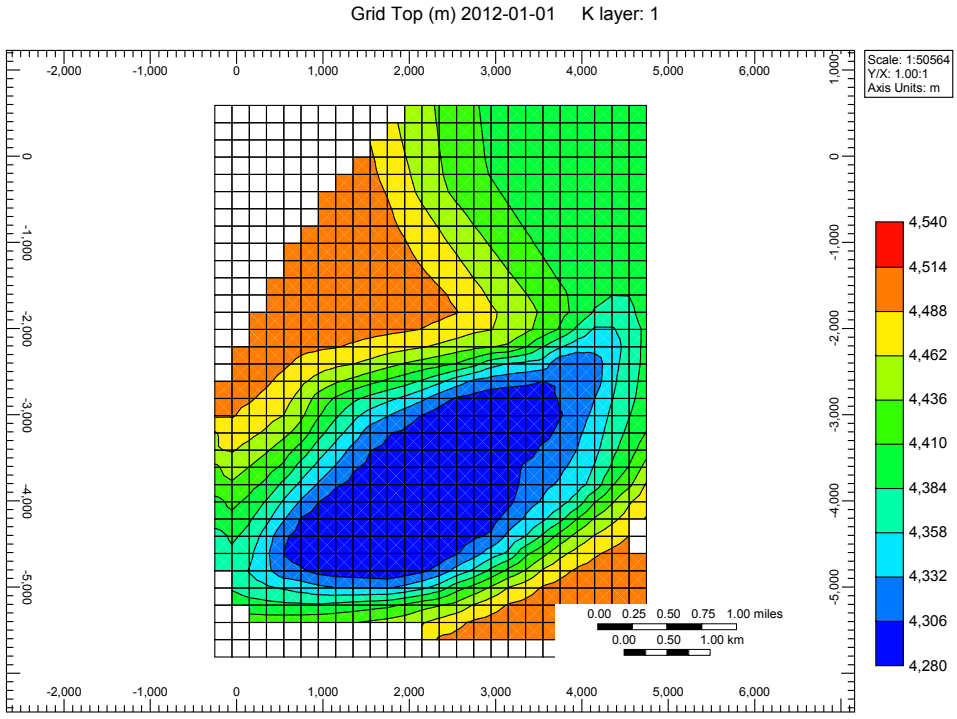

Figure 7.3: Structural map of the Camerina A (after Gray and Nunn (2010))

The initial pressure of the reservoir was assumed to be a uniform 80 MPa and the only variation in the initial pressure of the model is caused by the buoyancy and viscosity differences in the fluid during model initialization. The temperature of the zone varies between 128 and 150 $°C$ from the top to the bottom of the sand (Figure 7.5). Vertical wells were completed in all three layers of the model and were controlled using a constant flow rate constraint.

Net-to-gross ratios were only known at the wells and were kriged to estimate values for the other cells. The net-to-gross ratio relaxes to its average value away from available data. Rocks and fluids have different thermal characteristics, thus using net-to-gross ratio values helps to capture the effects of these differences.

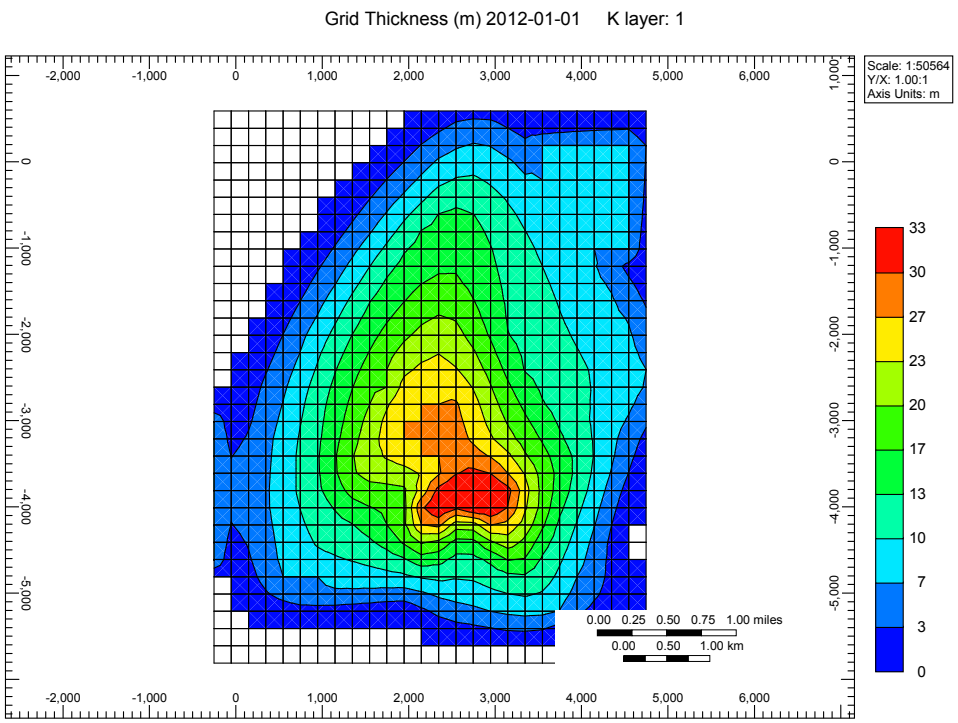

Figure 7.4: Isopach map of the Camerina A (after Gray and Nunn (2010))

7.1.3 Design and assumptions

We consider a mass withdrawal design in which all water that is produced from the reservoir is injected back into the reservoir. The total heat recovery during 30 years of geofluid production from the reservoir is then calculated. Binary power plants associated with low enthalpy geothermal reservoirs can have voidage-replacement ratios approaching one (DiPippo, 2012). Further, binary power plants require ca. 2500-4000 $m^3 day^{-1}$ of low enthalpy geothermal fluid to be economically viable. For the case studied here, eight vertical wells (four production and four injection) are used to deliver 8000 $m^3 day^{-1}$ (approximately two times the nominally required amount). Other assumptions are:

1. No history matching was done and the geologic model was fixed.

2. Eleven abandoned wells at the top of the Camerina A zone were chosen as candidate wells for the geothermal development. Out of these eleven, three wells were not used, four wells were chosen for production and four wells for injection. It is assumed

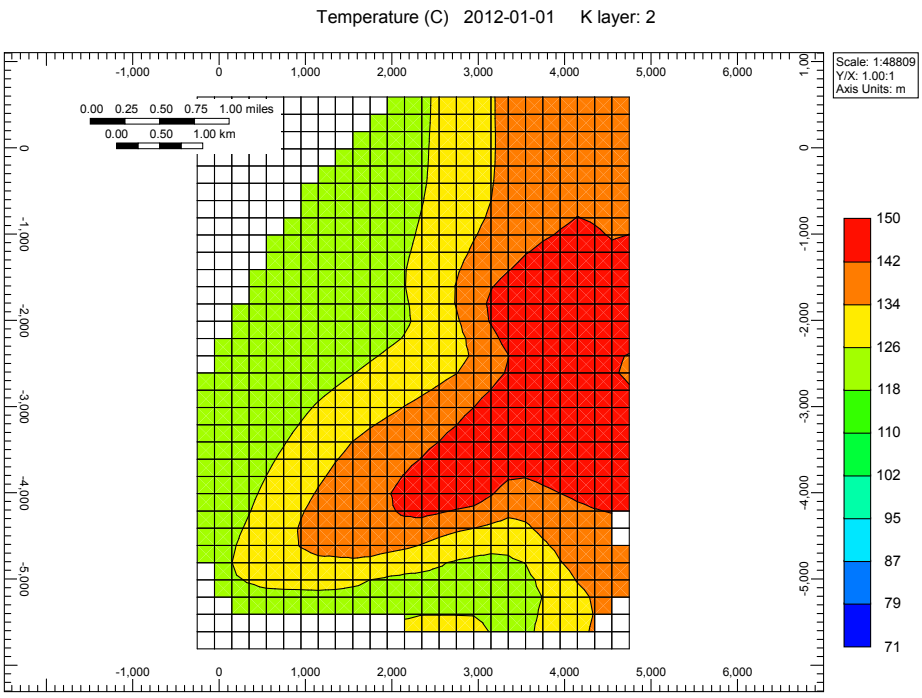

Figure 7.5: Initial reservoir temperature of the Camerina A (after Gray and Nunn (2010)).

that these wells can be restored for production and injection purposes (Quitzau and Bassiouni, 1981; Griggs, 2004).

3. No chemical reaction from cool water injection is considered (Safari-Zanjani et al.). Thus the permeability and porosity do not change and injection into the reservoir is not impaired. Power for the injection pump is not included in net energy calculations.

4. The flow rate constraint on each well is 2000 $m^3 day^{-1}$. These values were chosen to be lower than well test results from similar zones in Louisiana (John et al., 1998).

The model requires 11,550 numerical reservoir simulations for all well combinations. A particle swarm algorithm (CMOST, 2011) was used for determining the best well locations for maximum heat recovery within 500 runs. Values for ω, c1 and c2 were set to 0.6, 1.6 and 1.6 respectively and 10 particles were considered for the population size.

7.1.4 Results

The thermal state of the model after the initial 1000 years with no injection or production is nearly identical to that provided by the mapping of temperatures from well data. There are three natural convection cells in the model (Figure 7.6), with the highest flux arrow corresponding to velocities of ca. $3.3 \times m.day^{-1}$ ($3.8 \times 10^{-5}\ m.s^{-1}$). A mean interstitial fluid velocity of $3 \times 10^{-5}\ m.s^{-1}$ for most aquifers is a high value (Phillips, 2009). The natural convection is created by buoyancy and elevation differences in the model and is small near the boundaries. This initial state is used for the forced convection (heat extraction) studies that follow. Details of the wells are presented in Table 7.1.

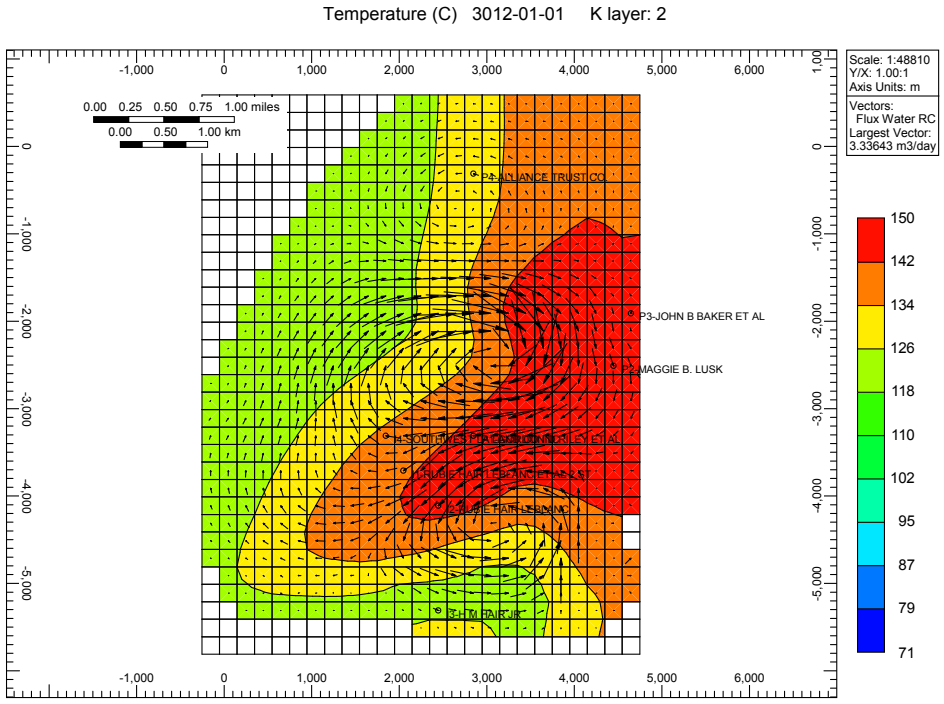

Figure 7.6: Predicted equilibrium state for the Camerina A geothermal reservoir. Three natural convection cell in the reservoir can be detected after the equilibrium state is reached.

The particle swarm optimization used 500 model runs and 10 particles for the population size, and assumed that the wells could be selected with replacement. However, the optimization sometimes naively selected wells more than once. After eliminating the infea-

Table 7.1: Detail of the wells

Well	Mid-perf depth (m)	Perforation length (m)	Status
Gordon D Riley et al #1	4319	78	Producer
Maggie B Lusk et al #1	4374.4	24.7	Producer
John B Baker et al #1	4392.45	16.9	Producer
Alliance Trust Co. #19	4431.6	32.2	Producer
Rubie Hair LeBlanc et al #2	4324.05	67.3	Injector
Ruby Hair LeBlanc #1	4323.65	84.5	Injector
H.M. Hair Jr. #1	4462.7	9.8	Injector
SW LA Land Co. Inc. et al #1	4339.6	75.1	Injector
U Cam RB Lejune	4348.4	55.8	Not used
U Cam H M Hair Est	4301.1	42.22	Not used
SW LA Land Co Inc	4356.1	45.5	Not used

sible cases, the optimal feasible case is predicted to produce 2.72×10^{16} J. The optimization task took ca. 825 minutes to complete.

The temperature response in the production wells (Figure 7.7) depends on the well locations in the field (Figure 7.8). The average temperature for the mixed fluid varies between 140-142 $°C$. The John B Baker et al #1 well shows a steady temperature and produces the highest enthalpy. The temperature of the Gordon D Riley et al. #1 has a concave down decline due to being located in a low temperature section of the reservoir (as compared to other production wells) and due to its proximity to injection wells. The temperature of the Maggie B Lusk et al #1 well increases as geofluid from the hotter sections of the reservoir flows toward it. The temperature drop in the Alliance Trust Co. #19 well is less than the Gordon D Riley et al. #1 well because it is located farther from the injection wells.

The optimization places production wells in the hotter sections of the reservoir while the injection wells are located in the cooler areas of the reservoir (Figure 7.8). Thermal breakthrough in the Gordon D Riley et al #1 well causes a decline in its temperature. For developing Gulf Coast geothermal projects, design of brine injection should emphasize thermal sweep of the reservoir because reservoir pressure is high enough to ensure adequate productivity. For the Camerina A, injection of cooled brine into the reservoir periphery

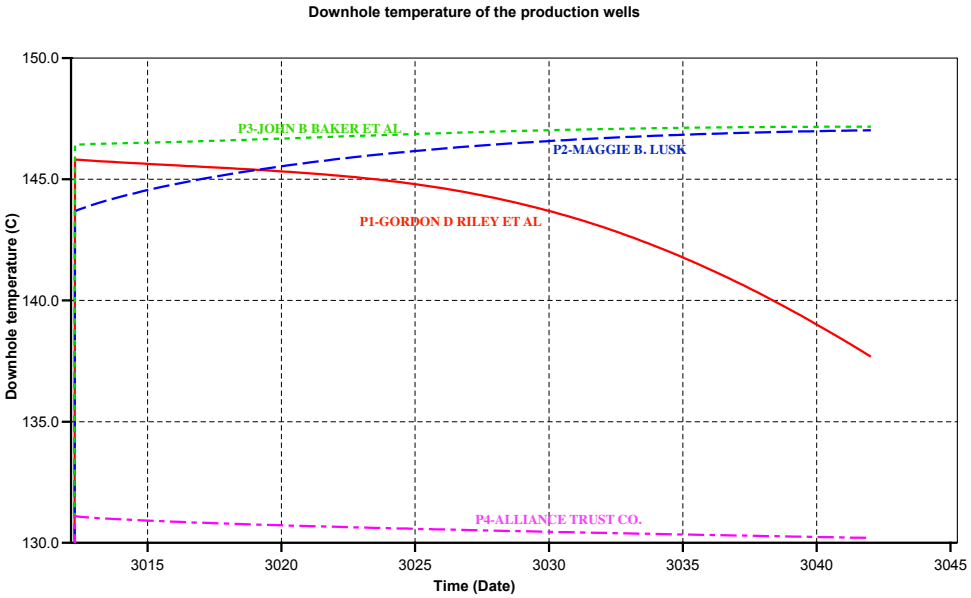

Figure 7.7: Downhole temperature profile of the selected production wells. The well John B Baker et al #1 shows a steady temperature and produces the highest enthalpy.

(which has lower temperatures) and producing from the hot areas gives the highest thermal sweep.

After 30 years of production, reservoir pressure remains high (Figure 7.9). The production of geofluid reduces the pressure around the production wells; injecting all of the cooled geofluid maintains the pressure around the injection wells. Near the boundaries, the pressures around the production wells decline more and pressures around the injection wells increase more than those away from the boundaries. In particular, the H.M. Hair Jr. #1 well is located in a low net-to-gross section of the reservoir and its surrounding pressure increases rapidly due to lower reservoir quality. Although the injected brine maintains reservoir pressure, the main reason for injection is disposal of the saline water. Production wells can likely sustain higher geofluid production rates because pressure declines are modest.

7.1.5 Discussion

The maximum net energy that can be extracted from the Camerina A zone using the suggested design is 2.72×10^{16} J for 30 years. The wells have similar constant production

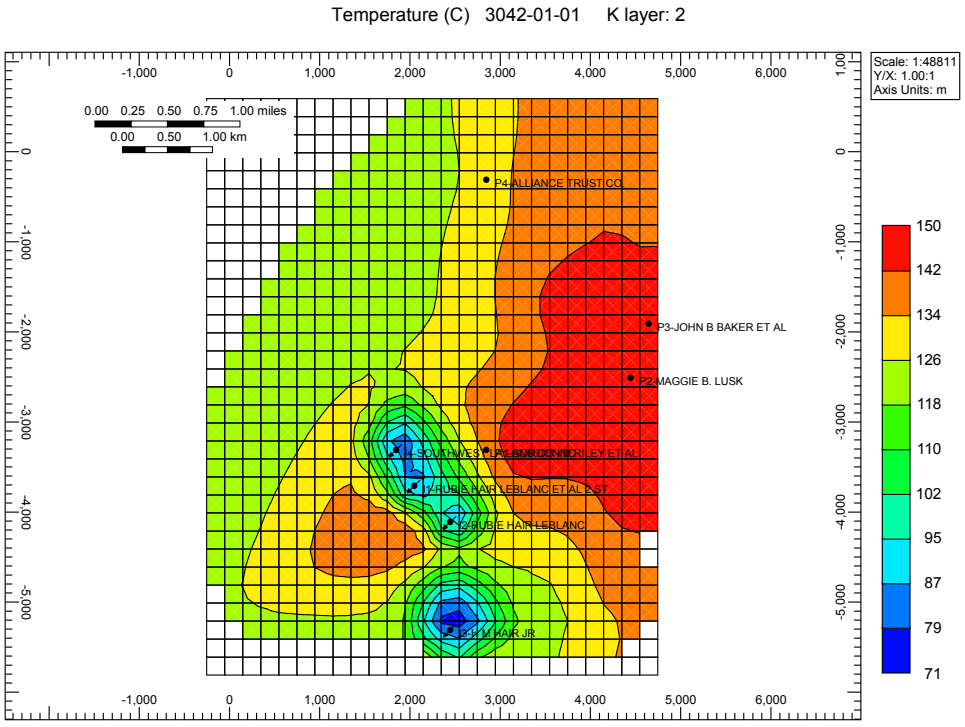

Figure 7.8: Reservoir temperature after 30 years of the geofluid injection/production. Thermal breakthrough in the Gordon D Riley et al #1 well causes a rapid decline in its temperature.

rates and the average temperature of the mixed geofluid is calculated to increase from 141.8 to 142.1 $°C$ after eleven years and then drop to 140.5 $°C$. The Camerina A is a low enthalpy geothermal reservoir (less than 150 $°C$), thus requiring a binary power plant. A Carnot cycle provides an upper bound on the efficiency of any power plant operating between a low temperature (here, the injection temperature T_{inj}) and a high temperature (here, production temperature T_{prod}). The Carnot relation is:

$$\eta = 1 - \frac{T_{inj}}{T_{prod}} = 1 - \frac{70 + 273.15}{140 + 273.15} = 17\% \tag{7.3}$$

The Carnot estimate for the assumed conditions is 4.88 MW. Binary cycles are less efficient than the Carnot. A more realistic cycle for calculating thermal efficiency of a binary plant is a triangular cycle. In this cycle, the brine transfers heat to a working

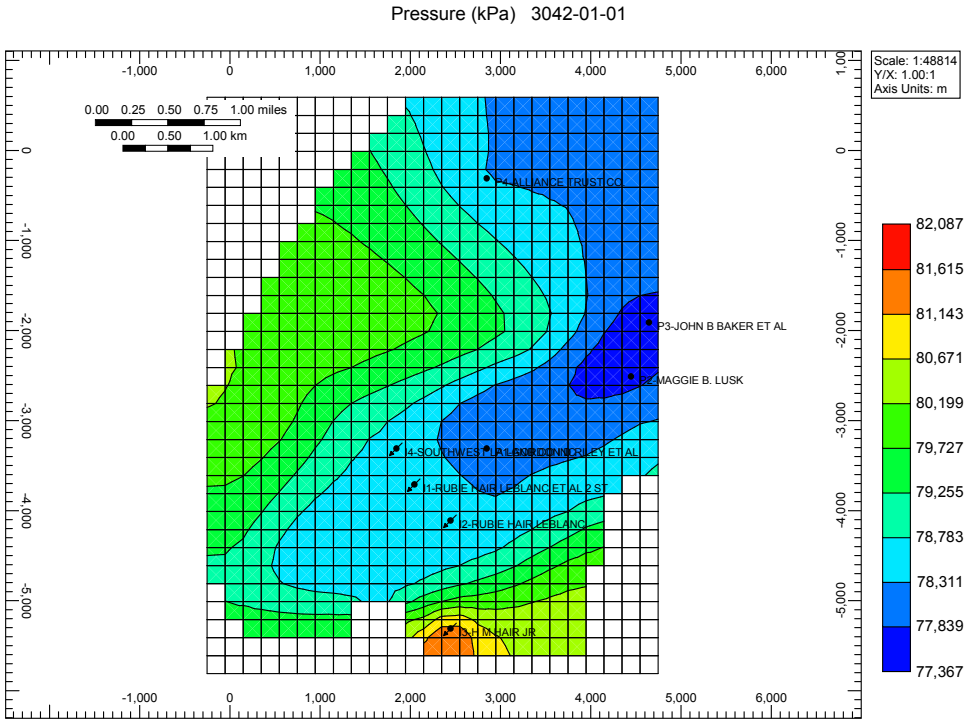

Figure 7.9: Reservoir pressure distribution after 30 years of geofluid injection/production. The production of geofluid for 30 years reduces the pressure of the reservoir around production wells and reinjecting constant flow rate cooler brine increases the pressure around the injection wells.

fluid in an isobaric state (ca. 80 MPa) instead of an isothermal state that Carnot cycle assumes. The geofluid cools as it passes through heat exchanger in an isentropic expansion. The brine is finally injected into the reservoir in an isothermal process (ca. 70 $°C$). The triangle rule (Eq. 7.4) yields a thermal efficiency of 9.26 percent:

$$\eta = \frac{T_{prod} - T_{inj}}{T_{prod} + T_{inj}} = 9.26\% \tag{7.4}$$

The small temperature differences between the production and injection wells result in low thermal efficiency. The triangle cycle suggests maximum average power (using the average produced fluid temperature) of 2.67 MW for the Camerina A model scenario.

Considering that the average rate of electricity consumption per person is about 0.5 kW, estimated the 2.67 MW of electricity would be sufficient to provide electricity for ca. 5000 persons for a period of 30 years.

Chandrasekharam and Bundschuh (2008) give an approximate formula for calculating the power production from geothermal systems: a flow rate of 25 to 27 $l.s^{-1}$ with a temperature between 140 to 147 $°C$ can produce 1 MW electricity. Using this approximation, the Camerina A scenario producing 92 $l.s^{-1}$ is capable of generating 3 to 4 MW of electricity.

Finally, because the pressure of the Camerina A zone remains high during its exploitation (Figure 7.9), downhole pumps are not needed to assist production.

7.1.6 Conclusion

The primary reason for brine injection into geopressured aquifers is to dispose of highly saline water and to mitigate geomechanical risk. For developing U.S. Gulf Coast geothermal projects, injection of brine should be designed to maximize thermal sweep of the reservoir. Because the pressure of these reservoirs is already high, the thermal sweep is more important than pressure maintenance. This study shows that injection of cool brine into the Gueydan Dome reservoir along the peripheral sections which have lower temperature and producing from the hot sections of the reservoir results in the highest thermal sweep. With the design proposed in this work, a system like the Gueydan Dome reservoir could produce at least 2.5 MW power for over thirty years. In the following, the developed models are used to calculate the net energy produced from the Gueydan Dome reservoir using the line drive model (Question 1) and the ZMW model (Question 2).

Question 1) The Gueydan Dome geothermal reservoir has a volume of $8.58 \times 10^8\, m^3$ and porosity of 0.2. If four production and four injection wells were used to develop this reservoir and the rate for each well is 2,000 m^3/day. Average reservoir temperature is 140 $°C$, injection temperature is assumed to be 70 $°C$ and reservoir rock thermal capacity is $1.97 \times 10^6\, J/m^3\, °C$. What would be the estimated recovery factor from this reservoir in 30 years? (assume reservoir dip angle is zero)

Answer) Water thermal capacity at 140 $^{\circ}C$ is ca. $3.956 \times 10^6 J/m^3\,^{\circ}C$. The energy in place is:

$$\begin{aligned}\rho_m\, C_{pm} &= \phi\, \rho_w\, C_{pw} + (1-\phi)\, \rho_r\, C_{pr} \\ &= 0.2 \times 3.956 \times 10^6 + 0.8 \times 1.97 \times 10^6 = 2.37 \times 10^6\, J/m^3\,^{\circ}C \end{aligned} \tag{7.5}$$

$$M = \frac{\rho_m C_{pm}}{\rho_f C_{pf}} = \frac{2.37 \times 10^6}{3.956 \times 10^6} = 0.6 \tag{7.6}$$

$$t_D = \frac{1}{0.6}\frac{qt}{LWH} = \frac{1}{0.6}\frac{8000\,\frac{m^3}{day} \times 30\,years}{8.58 \times 10^8\, m^3} = 0.17 \tag{7.7}$$

$$\pi_7 = \frac{L}{H}\tan(\alpha) = 0 \tag{7.8}$$

$$\pi_{15} = \frac{\tau \sin(\alpha) H}{T_{avg}} = 0 \tag{7.9}$$

$$\begin{aligned} T_D =& 0.9936 - 0.0267 t_D - 0.0516 \pi_{15} + 0.0002 \pi_7 \\ & - 0.8434 t_D \pi_{15} + 0.0029 t_D \pi_7 + 0.0045 \pi_{15} \pi_7 = 0.989 \end{aligned} \tag{7.10}$$

$$RF = 1.083 t_D = 0.18 \tag{7.11}$$

$$H_{in\,place} = \rho_m\, C_{pm}\, V\,(T_p - T_{ref})$$
$$= 2.37 \times 10^6 \times 8.58 \times 10^8 \times (140 - 25) = 2.34 \times 10^{17}\, J \tag{7.12}$$

The produced enthalpy is:

$$H_{pord} = RF \times H_{in\,place} = 4.22 \times 10^{16} \tag{7.13}$$

Water thermal capacity at 70 C is $4.09 \times 10^6 J/m^3\,^\circ C$. The enthalpy that is injected back into the reservoir during 30 years is:

$$H_{inj} = q_i \rho_m\, C_{pm}\,(T_i - T_{ref})$$
$$= 8000 \times 4.09 \times 10^6 \times 30 \times 365.24 \times (70 - 25) = 1.61 \times 10^{16}\, J \tag{7.14}$$

Thus the net produced energy is:

$$H_{net} = H_{prod} - H_{inj} = 2.61 \times 10^{16}\, J \tag{7.15}$$

The simulated energy recovery value for this reservoir is 2.72×10^{16} J.

Question 2) A ZMW system with a production, insulation and injection length of 300 m each is placed in the Gueydan Dome reservoir (described in Question 1). The production section provides a rate of 1000 m^3/day which is injected back into the reservoir from the injection section. Calculate the production temperature and the net produced energy within 30 years? Assume a thermal conductivity of $2.5 \times 10^5\, J/(m\, day\,^\circ C)$, a dip angle of zero, an average reservoir thickness of 45 m and $\frac{k_z}{k_y} = \frac{k_z}{k_x} = 0.5$

Answer) From Question 1, $M = 0.6$. Dimensionless time is:

$$t_D = \frac{1}{M}\frac{q\,t}{(L_{prod}+L_{ins}+L_{inj})L_{ins}H} = \frac{1}{0.6}\frac{1000\,\frac{m^3}{day}\times 30\,years}{900\times 300\times 45\,m^3} = 1.5 \tag{7.16}$$

$$\pi_6 = \frac{L_{prod}+L_{ins}+L_{inj}}{H}\sqrt{\frac{k_z}{k_x}} = 14.14 \tag{7.17}$$

$$\pi_8 = \frac{(L_{prod}+L_{ins}+L_{inj})}{H}\tan(\alpha_X) = 0 \tag{7.18}$$

$$\pi_{10} = \frac{L_{prod}}{H} = 6.67 \tag{7.19}$$

$$\kappa = \frac{\lambda_m}{\rho_f C_{pf}} = \frac{2.5\times 10^5}{3.956\times 10^6 J/m^3 C} = 0.0632 \tag{7.20}$$

$$\pi_{14} = \frac{u^*_{x1}z^*_1}{\kappa} = \frac{q}{\kappa L_{ins}} = \frac{1000}{0.0632\times 300} = 52.74 \tag{7.21}$$

$$\pi_{18} = \frac{T_{inj}}{T_{avg}} = \frac{70}{140} = 0.5 \tag{7.22}$$

For $0.5\leq t_D \leq 2.5$, we have:

$$\begin{aligned} T_D \; =& 0.9782 - 0.1051t_D + 0.0001\pi_{14} + 0.0059\pi_6 + 0.0963t_D\pi_{18} + 0.0018t_D\pi_{10} \\ &+ 0.0001\pi_{14}\pi_{10} - 0.0001\pi_{14}\pi_6 - 0.0002\pi_6\pi_{10} = 0.94 \end{aligned}$$

Thus the production temperature after 30 years of production using a line drive scheme is 138.5 C and using a single ZMW scheme is 135.4 ° C.

7.2 Sweet Lake

The Sweet Lake geopressured-geothermal aquifer, located southeast of Lake Charles, Louisiana, is a sedimentary basin, in the "Miogyp" sand of the Camerina zone of the upper Frio formation (John et al. (1998), Figure 7.10). The basin contains the Hackberry, Big Lake and Sweet Lake structures. The Sweet Lake aquifer is located in a dipping graben which widens westward (John et al., 1998). The Miogyp sand is typically found between 15000 to 15640 feet depth in the test well with 250 feet net sand and ca. 20° dip angle to the northwest (Gould et al., 1981; Hoffman et al., 1981).

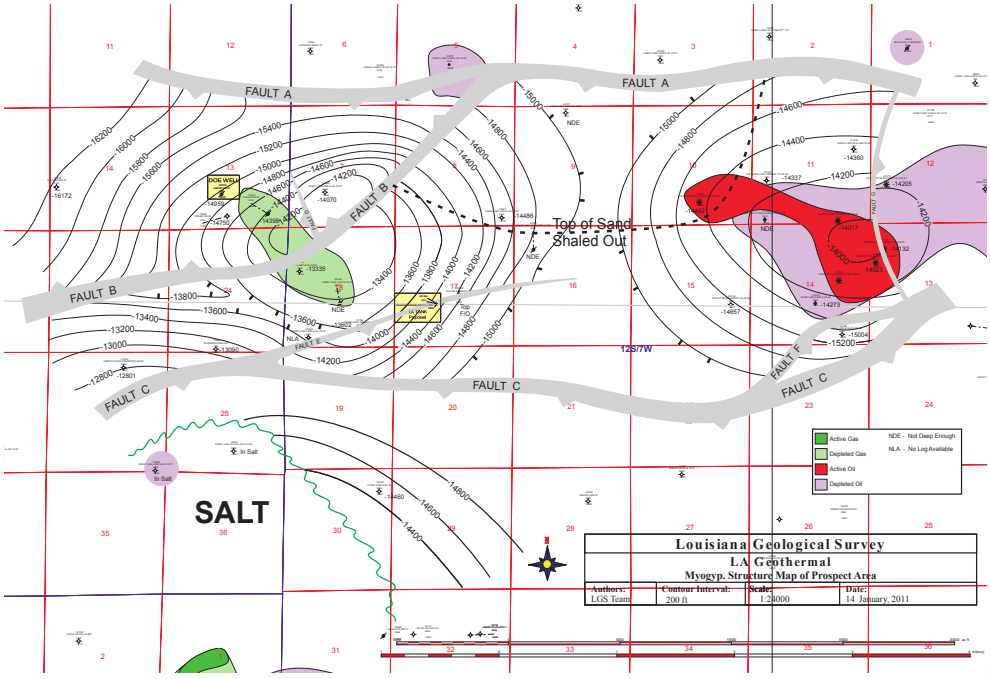

Figure 7.10: Structural map of the Sweet Lake reservoir (after John et al. (1998)).

7.2.1 Model

The initial reservoir's pressure in one of the perforated zones is recorded as 12060 psi, (ca. 4900 psi above normal reservoir pressure) (Andrade et al., 1982). The uniaxial compaction coefficient for this sand is $4.5 \times 10^{-7}\ psi^{-1}$, pore compressibility for 24 percent porosity is $1.5 \times 10^{-6}\ psi^{-1}$ and its total compressibility is $5 \times 10^{-6}\ psi^{-1}$ (Jogi et al., 1981).

Overburden pressure gradient is 1 psi/ft and pore pressure gradient is 0.5 to 1 psi/ft (Jogi et al., 1981).

Figure 7.11 shows the structural map of the Sweet Lake reservoir digitized from John et al. (1998) and loaded into the pre-processing application of the CMG software suite called Builder (2011). There were 27 miles of seismic lines, 17 well logs and multiple well test analysis used to construct this structural map. The graben angle is calculated as 26 degrees using well test analysis (Gould et al., 1981).

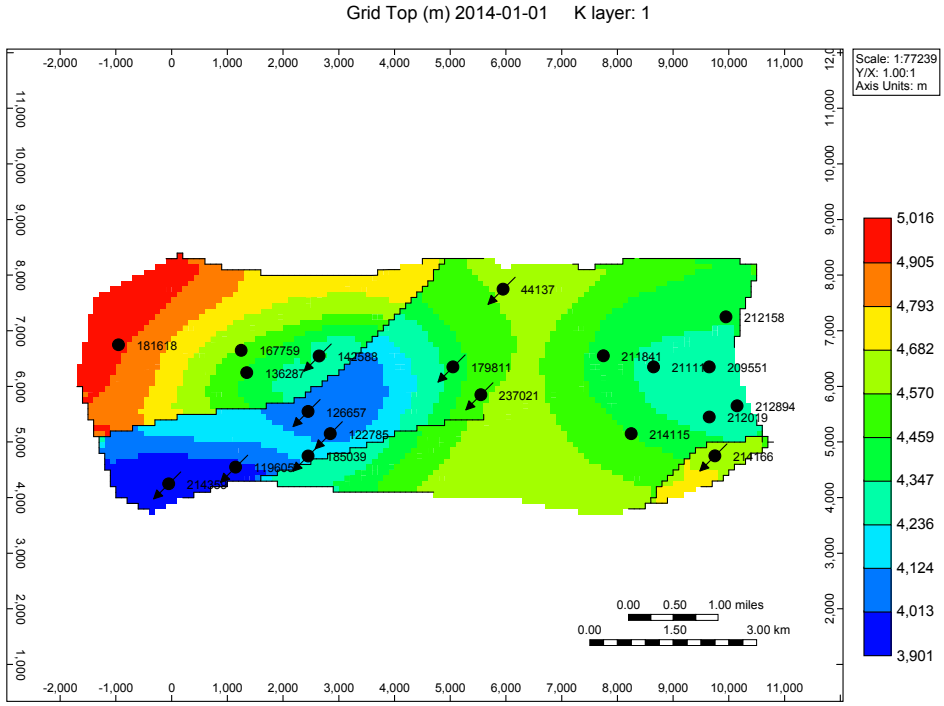

Figure 7.11: Structural map of the Sweet Lake (after John et al. (1998))

A corner point grid system of $125 \times 50 \times 7$ with the grid block length and width of 100 m is used for this reservoir. There are seven distinct sand layers within the Miogyp sequence (Hoffman et al., 1981). Because the thickness of the reservoir is not constant, the whole reservoir is divided into seven equal layers in the current study. Figure 7.12 shows the thickness of one of the reservoir layers.

Rock, water and overburden/underburden heat capacities and thermal conductivities were assumed to be identical to those in the Gueydan field study. Water properties such

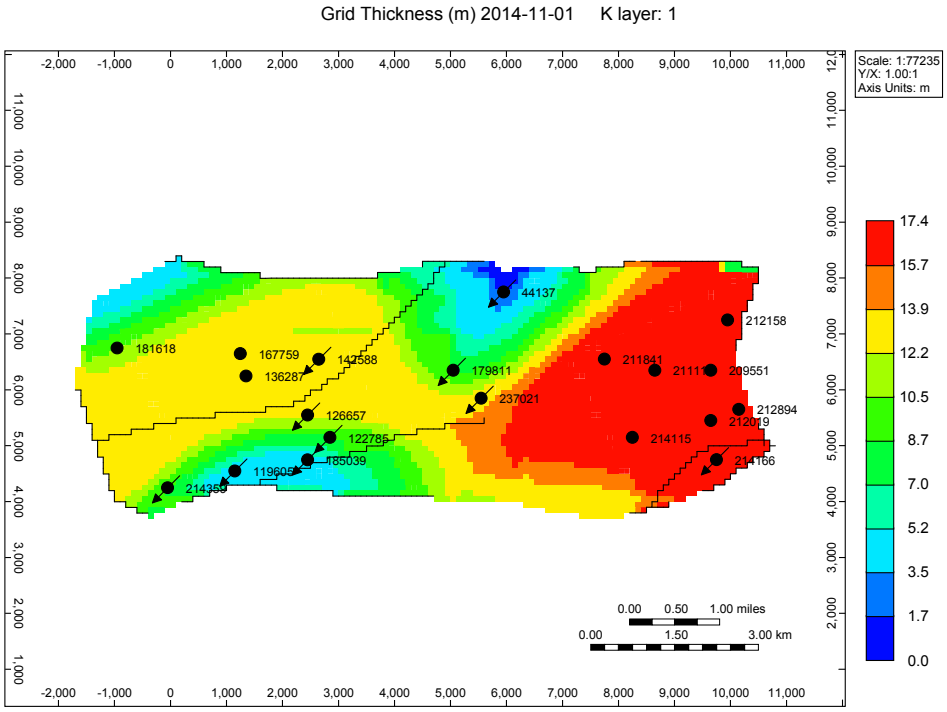

Figure 7.12: Isopach map of the Sweet Lake (after John et al. (1998))

as viscosity, heat capacity and thermal conductivity changes with temperature and are set to the simulator's default values (STARS manual, 2011).

The conclusion from the Gueydan Dome reservoir and the temperature map were used as the primary guideline for placing the injectors and producers to obtain a high thermal recovery. An average temperature of 300 °F (ca. 149 °C) with a geothermal gradient of 1.28 °F per 100 feet (ca. 0.024 °C/km) are calculated for this sand. Twenty wells in the Sweet Lake reservoir (named by their state serial numbers) were selected. Ten producers were placed in the hot sections of the reservoir and ten injectors in the lower temperature sections of the reservoir (Figure 7.13). Permeability, porosity and compressibility are important factors for determining aquifer flow rate. Early well test studies report an air permeability of 3.6 md (or water permeability of 400 md) for the fifth sand (Gould et al., 1981). Later studies report a permeability of 17.1 md for this layer (Andrade et al., 1982). The properties of the seven layers are shown in Table 7.2 (Hoffman et al., 1981). The flow rate of the wells were set to a constant value of 2000 m^3/day which is reasonable for this reservoir according

to the short production history that it has (John et al., 1998; Andrade et al., 1982). The water injection temperature of all the injectors were set to 40 °C.

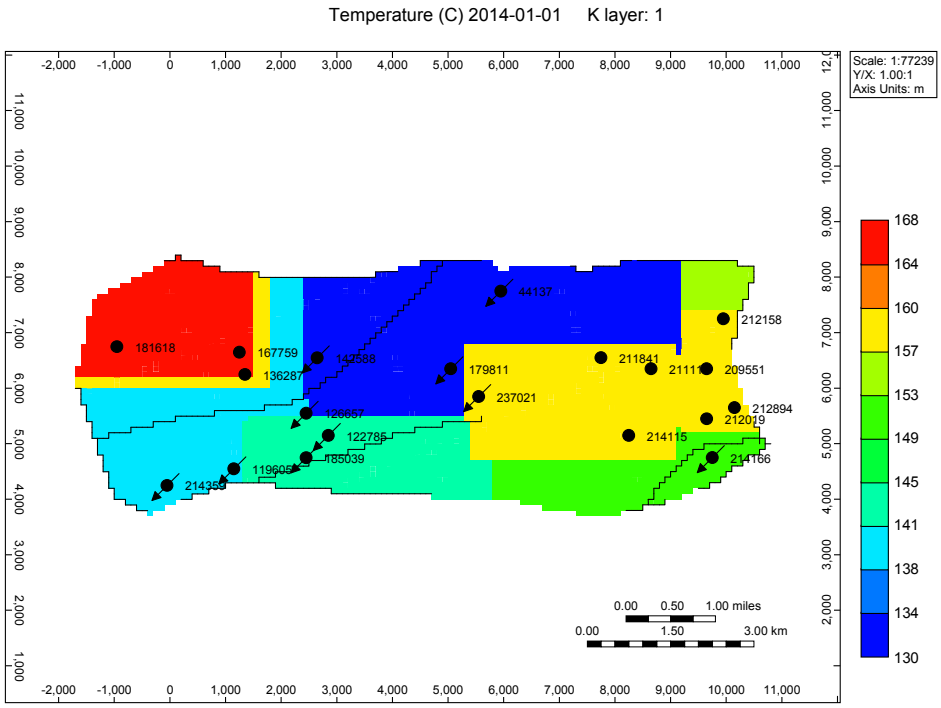

Figure 7.13: Initial reservoir temperature of the Sweet Lake. This map is an approximation to the map provided by Louisiana Geological Survey for Sweet Lake reservoir.

Table 7.2: Properties of the seven Sweet Lake layers.

Layer	Average porosity	Average permeability
1	0.1634	20
2	0.1386	20
3	0.2042	20
4	0.1812	140
5	0.2084	17.1
6	0.1569	20
7	0.13	30

7.2.2 Results

The simulation is run for 30 years to observe the effect of cold front movement and temperature change in the producers. Figure 7.14 shows the advancement of thermal front at the end of simulation. Most of the injectors are located far from the producers and they

don't have any influence on the produced hot water. Note that the temperature map has been the primary guideline for placing the producers and injectors which requires that one injector be located in the graben section. The thermal front of the injector in the graben section (well 142588) advances towards its nearby wells. Injector 214166 is isolated from its neighboring producers because of the nearby fault.

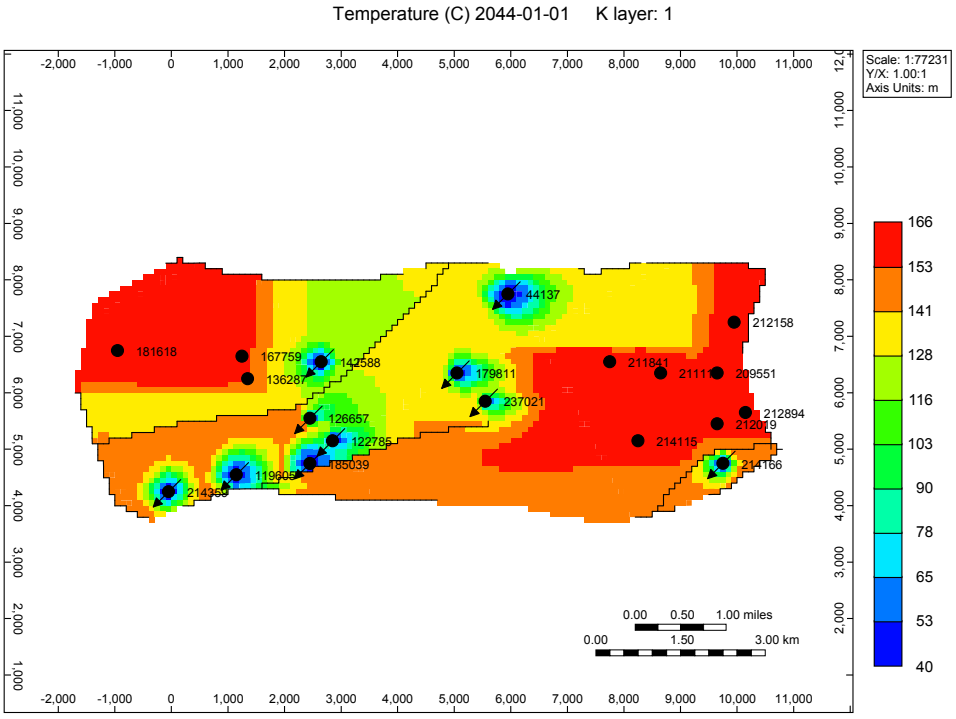

Figure 7.14: Reservoir temperature after 30 years of the geofluid injection/production. Thermal breakthrough in the well 167759 declines its temperature.

Three producers in the graben section show temperature decline (Figure 7.15). Well 136287 in the graben section shows the highest temperature reduction (ca. 20 °C) because of its proximity to injector 142588. Well 167759 shows 11 °C reduction in temperature. 3.5 °C temperature reduction in well 181618 is primarily due to the temperature distribution in the reservoir.

Most of the producers only show small temperature change during their production because the cold front does not reach them after 30 years of injection with the current rate

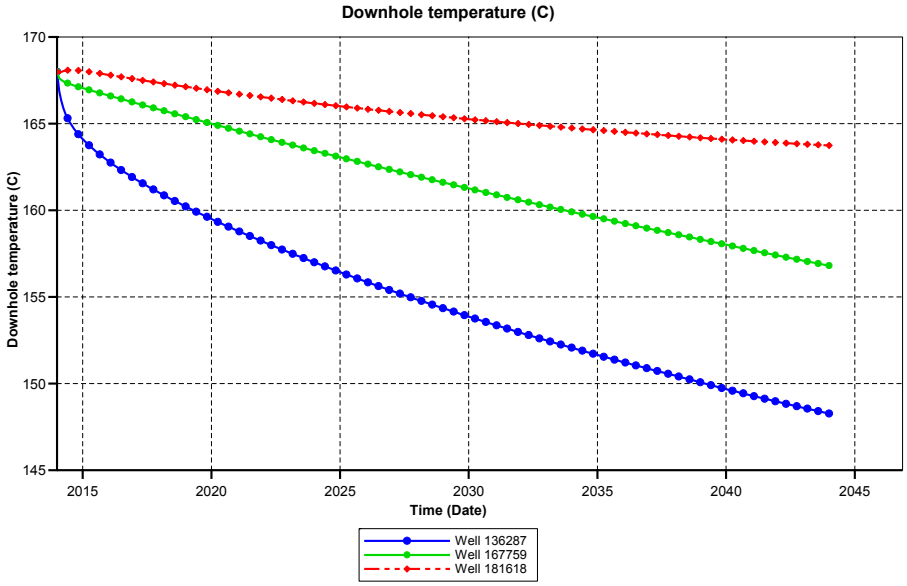

Figure 7.15: Downhole temperature profile of the production wells. The temperature of three wells reduces as a result of cold water injection.

(2000 m^3/day, Figure 7.16). The slight decrease and increase in temperature of all of these producers is the result of the initial temperature distribution in the reservoir.

7.2.3 Discussion

9.94×10^{16} J net energy can be produced from all the produces in 30 years, out of which 2.86×10^{16} J comes from the adjacent boundary of the reservoir. Economical geothermal energy production from Sweet Lake reservoir depends on its ability to produce at high rates for a long period of time (e.g. 30 years). Flow rates higher than 2000 m^3/day can be used for Sweet Lake wells considering the reservoir's high pressure, its volume and history (Andrade et al., 1982). However, it is not clear how long these flow rates can continue in practice. Maximum energy limit that could be produced from this reservoir is still uncertain in this pre-development assessment. Further research and development data such as high quality well test and production data for a long period of time and for all production wells are necessary to fully assess Sweet Lake prospect. In the following, the developed models are used to calculate the net energy production from the Sweet Lake reservoir using the line drive model (Question 1) and the ZMW model (Question 2).

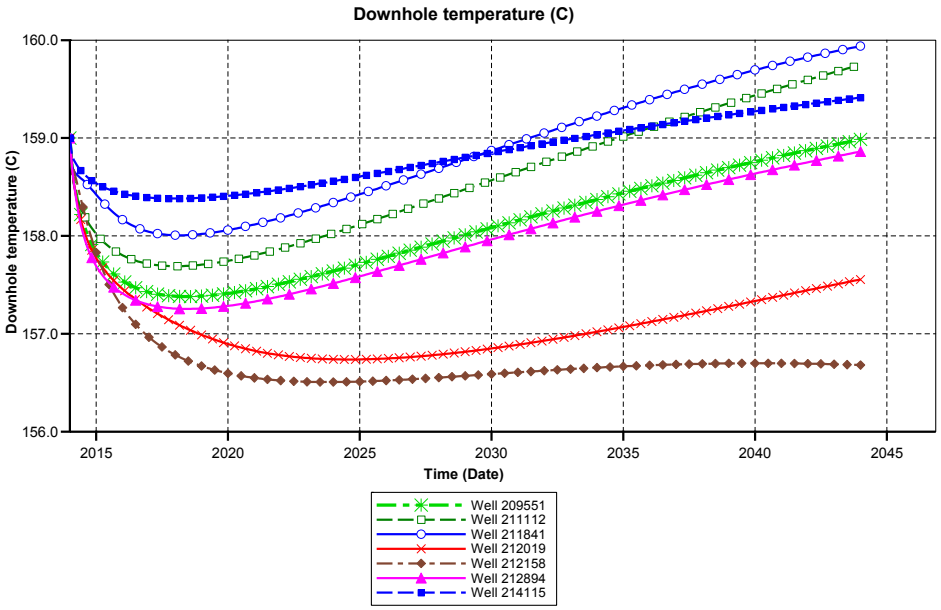

Figure 7.16: Downhole temperature profile of the production wells. Slight increase in temperature is due to geothermal gradient.

Question 1) The Sweet Lake geothermal reservoir has a volume of $4.23 \times 10^9\, m^3$ and an average porosity of 0.169 (Table 7.2). Ten production and ten injection wells produce from this reservoir. The rate of each well is 2000 m^3/day. Calculate the recovery factor from this reservoir in 30 years? Average reservoir temperature is 147.5 °C, injection temperature is 40 °C and reservoir rock thermal capacity is $1.97 \times 10^6 J/m^3\,°C$. Calculate the energy that could be produced from this reservoir within 30 years using the line drive model? (assume reservoir dip angle is zero)

Answer) Water thermal capacity at 147.5 °C is ca. $3.93 \times 10^6 J/m^3\,°C$. The energy in place is:

$$\begin{aligned} \rho_m\, C_{pm} &= \phi\, \rho_w\, C_{pw} + (1-\phi)\, \rho_r\, C_{pr} \\ &= 0.169 \times 3.93 \times 10^6 + 0.831 \times 1.97 \times 10^6 = 2.30 \times 10^6\, J/m^3\,°C \end{aligned} \tag{7.23}$$

$$M = \frac{\rho_m C_{pm}}{\rho_f C_{pf}} = \frac{2.30 \times 10^6}{3.93 \times 10^6} = 0.59 \tag{7.24}$$

$$t_D = \frac{1}{0.59}\frac{qt}{LWH} = \frac{1}{0.59}\frac{20000\,\frac{m^3}{day} \times 30\,years}{4.23 \times 10^9\,m^3} = 0.088 \tag{7.25}$$

$$\pi_7 = \frac{L}{H}\tan(\alpha) = 0 \tag{7.26}$$

$$\pi_{15} = \frac{\tau \sin(\alpha) H}{T_{avg}} = 0 \tag{7.27}$$

$$\begin{aligned} T_D =& 0.9936 - 0.0267 t_D - 0.0516 \pi_{15} + 0.0002 \pi_7 \\ & - 0.8434 t_D \pi_{15} + 0.0029 t_D \pi_7 + 0.0045 \pi_{15} \pi_7 = 0.99 \end{aligned} \tag{7.28}$$

$$RF = 1.083 t_D = 0.095 \tag{7.29}$$

$$\begin{aligned} H_{in\,place} &= \rho_m\, C_{pm}\, V\, (T_p - T_{ref}) \\ &= 2.30 \times 10^6 \times 4.23 \times 10^9 \times (147.5 - 25) = 1.19 \times 10^{18}\, J \end{aligned} \tag{7.30}$$

The produced enthalpy is:

$$H_{pord} = RF \times H_{in\,place} = 1.13 \times 10^{17} \tag{7.31}$$

Water thermal capacity at 40 °C is $4.124 * 10^6 J/m^3\,°C$. The enthalpy that is injected back into the reservoir during 30 years is:

$$\begin{aligned} H_{inj} &= q_i \rho_m \, C_{pm} \, (T_i - T_{ref}) \\ &= 20000 \times 4.124 \times 10^6 \times 30 \times 365.24 \times (40 - 25) = 1.32 \times 10^{16} \, J \end{aligned} \tag{7.32}$$

Thus the net produced energy is:

$$H_{net} = H_{prod} - H_{inj} = 9.98 \times 10^{16} \, J \tag{7.33}$$

The simulated value for this reservoir is $9.94 \times 10^{16} \; J$.

Question 2) A ZMW system with a production, insulation and injection length of 300 m each is placed in the Sweet Lake reservoir (described in Question 1). The production section provides a rate of 1000 m^3/day which is injected back into the reservoir from the injection section. Calculate the production temperature and the net produced energy within 30 years? Assume a thermal conductivity of $2.5 \times 10^5 \, J/(m.day\,°C)$, a dip angle of zero, an average reservoir thickness of 90 m and $\frac{k_z}{k_y} = \frac{k_z}{k_x} = 0.5$?

Answer) From Question 1, $M = 0.59$. Dimensionless time is:

$$t_D = \frac{1}{M} \frac{q\,t}{(L_{prod} + L_{ins} + L_{inj}) L_{ins} H} = \frac{1}{0.59} \frac{1000 \, \frac{m^3}{day} \times 30 \, years}{900 \times 300 \times 90 \, m^3} = 0.764 \tag{7.34}$$

$$\pi_6 = \frac{L_{prod} + L_{ins} + L_{inj}}{H} \sqrt{\frac{k_z}{k_x}} = 7.07 \tag{7.35}$$

$$\pi_8 = \frac{(L_{prod} + L_{ins} + L_{inj})}{H} \tan(\alpha_X) = 0 \tag{7.36}$$

$$\pi_{10} = \frac{L_{prod}}{H} = 3.33 \tag{7.37}$$

$$\pi_{11} = \frac{L_{inj}}{H} = 3.33 \tag{7.38}$$

$$\kappa = \frac{\lambda_m}{\rho_f C_{pf}} = \frac{2.5 \times 10^5}{3.93 \times 10^6} = 0.0636 \tag{7.39}$$

$$\pi_{14} = \frac{u^*_{x1} z^*_1}{\kappa} = \frac{q}{\kappa L_{ins}} = \frac{1000}{0.0636 \times 300} = 52.41 \tag{7.40}$$

$$\pi_{18} = \frac{T_{inj}}{T_{avg}} = \frac{40}{147.5} = 0.27 \tag{7.41}$$

$$\begin{aligned} T_D \ =& 0.9782 - 0.1051 t_D + 0.0001\pi_{14} + 0.0059\pi_6 + 0.0963 t_D \pi_{18} + 0.0018 t_D \pi_{10} \\ &+ 0.0001\pi_{14}\pi_{10} - 0.0001\pi_{14}\pi_6 - 0.0002\pi_6\pi_{10} = 0.945 \end{aligned}$$

Thus the production temperature after 30 years of production using a line drive scheme is 146 °C and using a single ZMW scheme is 139.4 °C.

Chapter 8

Conclusion and recommendation

8.1 Conclusions

Analytical solutions are a good way for understanding a physical phenomenon. Interpreting simulation results is not easy and analytical solutions are not always available. Statistical modeling is a good approach to translate the output of a simulator into quick models. In this work, two heat extraction designs were modeled using scaling and statistical modeling: a line drive system and a Zero Mass Withdrawal system.

This work makes following contributions or conclusions:

1. Dimensionless numbers associated with each of these designs were derived using Inspectional Analysis (IA).

2. Analytical solutions quickly become complicated. Scaling requires less intellectual effort compared with analytical solutions.

3. The spatial dimensions of the scaling are set by the spatial extension of the phenomenon. For complicated cases (such as the ZMW), analytical solutions were useful in defining scaling dimensions in the x and y directions.

4. The problem of multicollinearity in statistical modeling was brought to notice and a combination of methods were used for addressing it (e.g. the use of boosting algorithm for eliminating unimportant dimensionless numbers).

5. A Box-Behnken experimental design was used for sampling. Experimental designs gives maximum statistical information by sampling the entire space with fewer number of runs.

6. For model fitting, by creating the experimental design in the dimensional space, we can create more interpretable models and reduce multicollinearity, though it requires more runs.

7. For testing and verifying, the dimensionless numbers were selected first and then dimensional parameters were randomly selected to find reservoirs which have different dimensional parameters but identical dimensionless numbers.

8. After trying different sensitivity analysis approaches available in the machine learning literature, we found that a robust and promising method known as boosting gives interpretable results. This robust algorithm also finds relatively more important dimensionless numbers in predicting the response and removes less important dimensionless numbers.

9. Unlike previous research which ignores the less important dimensionless numbers heuristically and based on physical reasoning, boosting is a good approach for finding the important dimensionless numbers statistically and ignoring the less important ones.

10. The important dimensionless numbers found by boosting algorithm are critical. Our experience shows that if these important dimensionless numbers between the reservoirs match, then their dimensionless results will also match.

11. Dimensionless time was used in the models for the first time.

12. The importance of the dimensionless numbers changes with dimensionless time. Using segmented regression is a good approach for creating models that include dimensionless time.

13. The developed models were reduced and simplified using an all subset regression procedure.

14. The performance of the final models were assessed using training and testing runs.

15. The final models are simple and are interpretable.

8.2 Recommendations

Scaling and statistical modeling are still a developing area. More research is required for making these methods rigorous and schematic. Following works needs more research:

1. Defining meaningful dimensionless numbers creates multicollinearity and confounding problems in the regressors. Dimensionless numbers can be defined in ways to minimize their correlation.

2. Other regression methods such as ridge regression, lasso regression and principal component regression are useful tools for addressing multicollinearity and creating interpretable models. These methods can be studied in more details.

3. Principal component analysis can be another approach for reducing the number of variables. These methods were giving more complicated models (models with more terms) but may offer more accurate predictions.

4. Splines offer very useful set of tools for model fitting. The objective of this study was to obtain simple, quick and interpretable models. Splines are less interpretable and more complicated but give better predictions than the simple response surface.

5. There is a fundamental difference between this work and the work of Vogel (1968). In this work, the dimensionless numbers are calculated at the initial condition and do not change with dimensionless time and only their importance in predicting the response changes with dimensionless time. However in Vogel's work, dimensionless numbers are updated in time. Vogel's work can be studied in the framework of scaling and statistical modeling.

6. For the ZMW case, it may be possible to find an analytical solution for the streamlines using three dimensional complex analysis. The partial differential equations for the ZMW case can be simplified and coupled with this streamline model to create an analytical solution for a simplified case of the ZMW design (e.g. ignoring overburden/underburden boundaries, conduction in the reservoir, etc.). For simplified cases, analytical models can be compared with current developed models.

7. Box-Cox transformation can be used to normalize the response and Box-Tidwell transformation can be used to address nonlinearity in the response. For unknown reasons, this work didn't see any benefit when using Box-Tidwell and Box-Cox transformations. Gauss-Markov assumptions for the regression models can be checked and studied in more detail.

8. Because the importance of the dimensionless numbers changes with dimensionless time, other regression methods with time varying coefficients can be used instead of segmented regression to find more accurate models. Time series methods such as Kalman filters can be tested.

9. Gulf Coast geopressured geothermal reservoirs are also valuable assets for producing natural gas. Natural gas production from these reservoirs can also be considered in their economical evaluations.

10. Similar to water flooding, laboratory 3D models can be built for a geothermal reservoir in which the model is initially hot and then cold water is injected. These experiments can check the theoretically developed dimensionless numbers.

References

Afonja, G. I. (2013). *Development of a Framework for Scaling Surfactant Enhanced CO_2 Flooding from Laboratory Scale to Field Implementation.* Ph. D. thesis, Louisiana State University.

Afshari, S., B. Aminshahidy, and M. R. Pishvaie (2011). "Application of an improved harmony search algorithm in well placement optimization using streamline simulation". *Journal of Petroleum Science and Engineering 78*(3), 664–678.

Akhmadullin, I. and M. Tyagi (2014). "Design and analysis of electric power production unit for low enthalpy geothermal reservoir applications". *International Journal of Environmental, Chemical, Ecological, Geological and Geophysical Engineering 8*(6), 436–442.

Akın, S., M. V. Kok, and I. Uraz (2010). "Optimization of well placement geothermal reservoirs using artificial intelligence". *Computers & Geosciences 36*(6), 776–785.

Shirangi, M. G. and L. J. Durlofsky (2015). Closed-loop field development under uncertainty by use of optimization with sample validation. *SPE Journal 20*(05), 908–922.

Shirangi, M. G. and A. A. Emerick (2016). An improved tsvd-based levenberg–marquardt algorithm for history matching and comparison with gauss–newton. *Journal of Petroleum Science and Engineering 143*, 258–271.

Gharib Shirangi, M. (2014). History matching production data and uncertainty assessment with an efficient tsvd parameterization algorithm. *Journal of Petroleum Science and Engineering 113*, 54–71.

Al-Khoury, R. (2011). *Computational modeling of shallow geothermal systems.* CRC Press.

Safari-Zanjania, M., C. D. White, and J. S. Hanor. Impactst of rock-brine interactions on sandstone properties in lower miocene sediments, southwest louisiana.

Ansari, E. (2013). "Development of a surrogate simulator for two-phase subsurface flow simulation using trajectory piecewise linearization". *Journal of Petroleum Exploration and Production Technology*, 1–11.

Andrade, M., F. Rago, H. Ohkuma, K. Sepehrnoori, E. Peters, and M. Dorfman (1982). *Analysis of Sweet Lake geopressured-geothermal aquifer.* Technical report, Univ. of Texas, Austin.

Ansari, E., R. Hughes, and C. D. White (2014). "Well placement optimization for maximum energy recovery from hot saline aquifers". In *39th Workshop on Geothermal Reservoir Engineering, Stanford University. SGP-TR-202.*

Bangerth, W., H. Klie, M. Wheeler, P. Stoffa, and M. Sen (2006). "On optimization algorithms for the reservoir oil well placement problem". *Computational Geosciences 10*(3), 303–319.

Bassiouni, Z. (1980). *Evaluation of potential geopressure geothermal test sites in southern Louisiana*. Technical report, Louisiana State Univ., Baton Rouge (USA). Dept. of Petroleum Engineering.

Bebout, D., D. Gutierrez, and A. Bachman (1981). *Geopressured geothermal resource in Texas and Louisiana: geological constraints*. Technical report, Louisiana Geological Survey, Baton Rouge.

Bejan, A. (2013). *Convection heat transfer*. John Wiley & Sons.

Box, G. E., J. S. Hunter, and W. G. Hunter (2005). *Statistics for experimenters: design, innovation, and discovery*, Volume 2. Wiley Online Library.

Buckingham, E. (1914). "On physically similar systems; illustrations of the use of dimensional equations". *Physical Review 4*(4), 345–376.

Builder (2011). Pre-processing application. *Computer Modeling Group, Ltd, Calgary, AB, Canada*.

Chandrasekharam, D. and J. Bundschuh (2008). *Low-enthalpy geothermal resources for power generation*. CRC Press.

CMOST (2011). Enhance and accelerate sensitivity analysis, history matching, optimization and uncertainty analysis. *Computer Modeling Group, Ltd, Calgary, AB, Canada*.

Craig, F., J. Sanderlin, D. Moore, T. Geffen, et al. (1957). "A laboratory study of gravity segregation in frontal drives". *Trans. AIME 210*(275).

DiPippo, R. (2012). *Geothermal power plants: principles, applications, case studies and environmental impact*. Butterworth-Heinemann.

Durham Jr, C., D. Bebout, and A. Bachman (1981). *Background and status of the Sweet Lake geopressured-geothermal test, Cameron Parish, Louisiana*. Technical report.

Eberhart, R. and J. Kennedy (1995). "a new optimizer using particle swarm theory". In *Micro Machine and Human Science, 1995. MHS'95., Proceedings of the Sixth International Symposium on*, pp. 39–43. IEEE.

Feng, Y. (2012). *Numerical study of downhole heat exchanger concept in geothermal energy extraction from saturated and fractured reservoirs*. Ph. D. thesis, Louisiana State University.

Feng, Y., M. Tyagi, and C. D. White (2014). "A downhole heat exchanger for horizontal wells in low-enthalpy geopressured geothermal brine reservoirs". *Geothermics 53*, 368–378.

Fridleifsson, I. B., R. Bertani, E. Huenges, J. W. Lund, A. Ragnarsson, and L. Rybach (2008). "The possible role and contribution of geothermal energy to the mitigation of climate change". In *IPCC scoping meeting on renewable energy sources, proceedings, Luebeck, Germany*, Volume 20, pp. 59–80. Citeseer.

GEA (2012). *Geothermal Energy Association, Geothermal: International Market Overview Report* . Technical report.

Geertsma, J., G. A. Croes, and N. Schwarz (1956). "Theory of dimensionally scaled models of petroleum reservoirs". *Trans. AIME 207*, 118–127.

Gould, T., C. Kenner, J. Clark, D. Bebout, and A. Bachman (1981). *Reservoir engineering and computer model analyses of flow tests on the Miogypsinoides sandstone: Sweet Lake geothermal-geopressured prospect*. Technical report, Intercomp, Houston, TX.

Grant, M. (2013). *Geothermal reservoir engineering*. Access Online via Elsevier.

Gray, T. and J. Nunn (2010). "Geothermal resource assessment of the Gueydan salt dome and the adjacent Southeast Gueydan Field". *Gulf Coast Association of Geological Societies Transactions 60*, 307–323.

Griggs, J. (2004). A re-evaluation of geopressured-geothermal aquifers as an energy resource. Master's thesis, Louisiana State University.

Gringarten, A. and J. Sauty (1975). "a theoretical study of heat extraction from aquifers with uniform regional flow". *Journal of Geophysical Research 80*(35), 4956–4962.

Hastie, T., R. Tibshirani, J. Friedman (2009). *The elements of statistical learning*, Volume 2. Springer.

Hawkins, M. F. J. (1977). *Investigations on the Geo-pressure Energy Resource of Southern Louisiana*. Technical report, Final report to ERDA on contract No. AT-(40-1)-4889, Louisiana State University.

Hoffman, K., C. Durham Jr, D. Bebout, and A. Bachman (1981). *Geology of the Sweet Lake Prospect, Cameron Parish, Louisiana: an update*. Technical report, Magma Gulf Co., Houston, TX.

James, G., D. Witten, T. Hastie, and R. Tibshirani (2013). *An introduction to statistical learning*. Springer.

Jin, L., A. K. Wojtanowicz, G. Afonja, and W. Li (2010). "Scaling analysis of wells with downhole water loop completion for bottomwater control". *Journal of Canadian Petroleum Technology 49*(11), 81–90.

Jin, R., W. Chen, and T. W. Simpson (2001). "Comparative studies of metamodelling techniques under multiple modelling criteria". *Structural and Multidisciplinary Optimization 23*(1), 1–13.

Jogi, P., S. Kalra, K. Gray, T. Thompson, D. Bebout, and A. Bachman (1981). "Compaction measurements on the Sweet Lake test well". Technical report, Univ. of Texas, Austin.

John, C., G. Maciasz, and B. Harder (1998). *Gulf Coast geopressured-geothermal program summary report compilation. Volume 2-A: Resource description, program history, wells tested, university and company based research, site restoration.* Technical report, Louisiana State Univ., Basin Research Inst., Baton Rouge, LA (United States).

Kalla, S. (2005). Use of orthogonal arrays, quasi-monte carlo sampling, and kriging response models for reservoir simulation with many varying factors. Master's thesis, Louisiana State University.

Kroese, D. P., T. Taimre, and Z. I. Botev (2011). *Handbook of Monte Carlo Methods*, Volume 706. John Wiley & Sons.

Kuhn, M. and K. Johnson (2013). *Applied predictive modeling*. Springer.

Landa, J. and G. Bars (2003). "A methodology for history matching and the assessment of uncertainties associated with flow prediction". In *SPE Annual Technical Conference and Exhibition, Denver, Colorado, SPE-84465-MS*, Denver, Colorado, SPE-84465-MS.

Langhaar, H. L. (1951). *Dimensional analysis and theory of models*, Volume 2. Wiley New York.

Lemmon, E., M. Huber, and M. McLinden (2007). REFPROP user's guide version 8.0. *National Institute of Standards and Technology, Colorado*.

Lu, J. (1998). A mathematical model of horizontal wells productivity and well testing analysis. Master's thesis, Virginia Polytechnic Institute and State University.

Lund, J. W. (2003). "The use of downhole heat exchangers". *Geothermics 32*(4), 535–543.

McMullan, J. H. and Z. Bassiouni (1984). rediction of maximum flow rates from geopressured aquifers". *Journal of petroleum technology 36*(3), 503–509.

Mendenhall, W., R. Beaver, and B. Beaver (2012). *Introduction to probability and statistics*. Cengage Learning.

Montgomery, D. C., D. C. Montgomery, and D. C. Montgomery (1984). *Design and analysis of experiments*, Volume 7. Wiley New York.

Montgomery, D. C. and R. H. Myers (1995). *Response surface methodology: process and product optimization using designed experiments*, Volume 705. John Wiley & Sons.

Montgomery, D. C., E. A. Peck, and G. G. Vining (2012). *Introduction to linear regression analysis*, Volume 821. Wiley.

Muffler, P. and R. Cataldi (1978). "Methods for regional assessment of geothermal resources". *Geothermics 7*(2), 53–89.

Nathenson, M. (1975). *Physical factors determining the fraction of stored energy recoverable from hydrothermal convection systems and conduction-dominated areas*. Technical report, Geological Survey, Menlo Park, Calif.(USA).

Novakovic, D. (2002). *Numerical reservoir characterization using dimensionless scale numbers with application in upscaling*. Ph. D. thesis, Louisiana State University.

Onwunalu, J., M. Litvak, L. Durlofsky, and K. Aziz (2008). "Application of statistical proxies to speed up field development optimization procedures". In *Abu Dhabi International Petroleum Exhibition and Conference, SPE-117323-MS*.

Onwunalu, J. E. and L. J. Durlofsky (2010). "Application of a particle swarm optimization algorithm for determining optimum well location and type". *Computational Geosciences 14*(1), 183–198.

Phillips, O. M. (2009). *Geological fluid dynamics: sub-surface flow and reactions*. Cambridge University Press.

Plaksina, T., C. White, J. Nunn, and T. Gray (2011). "Effects of coupled convection and CO_2 injection in simulation of geopressured geothermal reservoirs". In *36th Workshop on Geothermal Reservoir Engineering, Stanford University*, pp. 146–154.

Quitzau, R. and Z. Bassiouni (1981). "The possible impact of the geopressure resource on conventional oil and gas exploration". In *SPE Annual Technical Conference and Exhibition, San Antonio, Texas, SPE-10281-MS.*

R Core Team (2014). *R: A Language and Environment for Statistical Computing*. Vienna, Austria: R Foundation for Statistical Computing.

Rai, K. (2008). Screening model for surfactant-polymer flooding using dimensionless groups. Master's thesis, University of Texas at Austin.

Rice, J. (2006). *Mathematical statistics and data analysis*. Cengage Learning.

Robinson, E. (1967). *Acadia and Vermolion Parishes, Louisiana*. Technical report, The Pure Oil Company, Geomap Company, Plano, TX.

Ruark, A. E. (1935). "Inspectional analysis: a method which supplements dimensional analysis". *Journal of the Mitchell Society 51*, 127–133.

Sarma, P. and W. Chen (2008). "Efficient well placement optimization with gradient-based algorithms and adjoint models". In *Intelligent Energy Conference and Exhibition, Amsterdam, The Netherlands, SPE-112257-MS*.

Shook, M., D. Li, and L. W. Lake (1992). "Scaling immiscible flow through permeable media by inspectional analysis". *In Situ;(United States) 16*(4).

Simpson, T. W., D. K. Lin, and W. Chen (2001). "Sampling strategies for computer experiments: design and analysis". *International Journal of Reliability and Applications 2*(3), 209–240.

Simpson, T. W., T. M. Mauery, J. J. Korte, and F. Mistree (2001). "Kriging models for global approximation in simulation-based multidisciplinary design optimization". *AIAA journal 39*(12), 2233–2241.

Sonin, A. A. (2001). The physical basis of dimensional analysis. *Department of Mechanical Engineering, MIT, Cambridge, MA*.

Soong, T. T. (2004). *Fundamentals of probability and statistics for engineers*. John Wiley & Sons.

STARS manual (2011). Advanced process and thermal reservoir simulator. *Computational Modeling Group, Ltd. , Calgary, AB, Canada*.

Tan, Q.-M. (2014). *Dimensional analysis*. Springer.

Tester, J. W., B. J. Anderson, A. Batchelor, D. Blackwell, R. DiPippo, E. Drake, J. Garnish, B. Livesay, M. Moore, K. Nichols, et al. (2006). The future of geothermal energy. *Massachusetts Institute of Technology 358*.

Tupac, Y., L. Almeida, L. Almeida, and M. Vellasco (2007). "evolutionary optimization of oil field development". In *Digital Energy Conference and Exhibition, Houston, Texas, U.S.A, SPE-107552-MS*.

Tyagi, M. and C. White (2010). DOE project proposal.

Vinsome, P. and J. Westerveld (1980). "A simple method for predicting cap and base rock heat losses in'thermal reservoir simulators". *Journal of Canadian Petroleum Technology 19*(3).

Wang, H., D. Echeverr a Ciaurri, L. Durlofsky, and A. Cominelli (2012). Optimal well placement under uncertainty using a retrospective optimization framework. *SPE Journal 17*(1), 112–121.

White, C. and S. Royer (2003). Experimental design as a framework for reservoir studies. In *SPE Reservoir Simulation Symposium, Houston, Texas, SPE-79676-MS*.

White, C. D. (2013). *Statistical Reservoir Modeling, PETE 7285 course notes*.

Williams, C. F., M. J. Reed, and R. H. Mariner (2008). A review of methods applied by the us geological survey in the assessment of identified geothermal resources. *US Geological Survey Open-File Report 1296*(2008), 27.

Wood, D. J., L. W. Lake, R. T. Johns, V. Nunez, et al. (2008). "A screening model for CO_2 flooding and storage in Gulf Coast reservoirs based on dimensionless groups". *SPE Reservoir Evaluation & Engineering 11*(03), 513–520.

Appendix A

Deriving fundamental equations

A.1 Continuity equation

The general continuity equation for single phase flow in porous media shows that the divergence of the mass transport determines the change in the water mass in the medium if no water is generated in the rock (Eq. A.1, Phillips (2009)).

$$\frac{\partial}{\partial t}(\phi\rho_f) + \nabla.(\rho_f \mathbf{u}) = 0 \tag{A.1}$$

The continuity equation can be expanded to yield Eq. A.2:

$$\rho_f \frac{\partial \phi}{\partial t} + \phi \frac{\partial \rho_f}{\partial t} + \nabla \rho_f . \mathbf{u} + \rho_f \nabla . \mathbf{u} = 0 \tag{A.2}$$

Rock and fluid characteristics (Eqs. A.3-A.6) can be substituted into the continuity equation (Eq. A.2) by applying the chain rule in time (Eqs. A.7, A.8) and space (Eqs. A.9, A.10) to get a physically useful form. (Eq. A.11)

$$c_f = \frac{1}{\rho_f}(\frac{\partial \rho_f}{\partial p}) \tag{A.3}$$

$$c_\phi = \frac{1}{\phi}(\frac{\partial \phi}{\partial p}) \tag{A.4}$$

$$\beta_f = -\frac{1}{\rho_f}(\frac{\partial \rho_f}{\partial T}) \tag{A.5}$$

$$\beta_\phi = -\frac{1}{\phi}(\frac{\partial \phi}{\partial T}) \tag{A.6}$$

$$\frac{\partial \rho_f}{\partial t} = \frac{\partial \rho_f}{\partial p}.\frac{\partial p}{\partial t} + \frac{\partial \rho_f}{\partial T}.\frac{\partial T}{\partial t} = \rho_f c_f \frac{\partial p}{\partial t} - \rho_f \beta_f \frac{\partial T}{\partial t} \tag{A.7}$$

$$\frac{\partial \phi}{\partial t} = \frac{\partial \phi}{\partial p}.\frac{\partial p}{\partial t} + \frac{\partial \phi}{\partial T}.\frac{\partial T}{\partial t} = \phi c_\phi \frac{\partial p}{\partial t} - \phi \beta_\phi \frac{\partial T}{\partial t} \tag{A.8}$$

$$\nabla \rho_f = \rho_f c_f \nabla p - \rho_f \beta_f \nabla T \tag{A.9}$$

$$\nabla \phi = \phi c_\phi \nabla p - \phi \beta_\phi \nabla T \tag{A.10}$$

$$\rho_f(\phi c_\phi \frac{\partial p}{\partial t} - \phi \beta_\phi \frac{\partial T}{\partial t}) + \phi(\rho_f c_f \frac{\partial p}{\partial t} - \rho_f \beta_f \frac{\partial T}{\partial t}) + (\rho_f c_f \nabla p - \rho_f \beta_f \nabla T).\mathbf{u} + \rho_f \nabla.\mathbf{u} = 0 \tag{A.11}$$

Dividing Eq. A.11 by ρ_f and substituting $c_t = c_f + c_\phi$ and $\beta_t = \beta_f + \beta_\phi$ yields Eq. A.12:

$$\phi(c_t)\frac{\partial p}{\partial t} - \phi(\beta_t)\frac{\partial T}{\partial t} + (c_f \nabla p - \beta_f \nabla T).\mathbf{u} + \nabla.\mathbf{u} = 0 \tag{A.12}$$

A.2 Darcy equation

The general form of the Darcy equation describes the velocity field in the reservoir (Eq. A.13); in which $\mathbf{Z}$ is a unit vector normal to the horizontal and $\mathbf{k}$ is the permeability tensor.

$$\mathbf{u} = -\frac{\mathbf{k}}{\mu}(\nabla P + \rho_f g \mathbf{Z}) \tag{A.13}$$

A.3 Energy equation

The general form of the energy equation in porous media describes convection and conduction in the reservoir (Eq. A.14, Grant (2013)).

$$\frac{\partial}{\partial t}\left((1-\phi)\,\rho_r U_r + \phi \rho_f U_f\right) + \nabla.(\rho_f \mathbf{u}\,\mathcal{H} - \boldsymbol{\lambda}\nabla T) = 0 \tag{A.14}$$

For liquids and solids, $C_v \approx C_p$ and we can assume $U = \mathcal{H} = C_p T$ (Al-Khoury, 2011). Assuming constant matrix conductivity ($\boldsymbol{\lambda} = \lambda_m = \lambda_f \phi + \lambda_r(1-\phi)$) and expanding the convection term yields Eq. A.15:

$$((1-\phi)\rho_r C_{pr}\frac{\partial T}{\partial t}+\phi\rho_f C_{pf}\frac{\partial T}{\partial t})+\nabla\rho_f\mathbf{u}\,\mathcal{H}+\rho_f\mathbf{u}\nabla\mathcal{H}+\rho_f\mathcal{H}\nabla.\mathbf{u}-\lambda_m\nabla^2 T=0 \quad \text{(A.15)}$$

Substituting Eqs. A.7, A.8 (the chain rule in time) into Eq. A.2, multiplying it by $\mathcal{H}$ and rearranging, yields Eq. A.16.

$$\nabla\rho_f.\mathbf{u}\,\mathcal{H}+\rho_f\mathcal{H}\nabla.\mathbf{u}=-C_{pf}T\phi(\rho_f c_f\frac{\partial p}{\partial t}-\rho_f\beta_f\frac{\partial T}{\partial t})-C_{pf}T\rho_f(\phi c_\phi\frac{\partial p}{\partial t}-\phi\beta\phi\frac{\partial T}{\partial t}) \quad \text{(A.16)}$$

Substituting Eq. A.16 into Eq. A.15, defining matrix heat capacity $\rho_m C_{pm}=\phi\rho_f C_{pf}+(1-\phi)\rho_r C_{pr}$, matrix/fluid heat capacity ratio $M=(\rho_m C_{pm})/(\rho_f C_{pf})$, thermal diffusivity $\kappa=\lambda_m/(\rho_f C_{pf})$, total compressibility $c_t=c_f+c_\phi$ and total thermal expansivity $\beta_t=\beta_f+\beta_\phi$, yields Eq. A.17:

$$M\frac{\partial T}{\partial t}+\mathbf{u}.\nabla T-T\phi(c_t\frac{\partial p}{\partial t}-\beta_t\frac{\partial T}{\partial t})-\kappa\nabla^2 T=0 \quad \text{(A.17)}$$

In geothermal reservoirs, heat is gained from adjacent strata (i.e. overburden/underburden) of the reservoir. Specifically in Zero Mass Withdrawal systems, the reservoir's enthalpy is recovered during time because no mass is reduced. We assume that overburden and underburden layers extend to infinity and they are impermeable, thus having only conduction heat transfer. With convecting velocities being zero, Eq. A.17 is reduced to Eqs. A.18 and A.19 for overburden and underburden respectively:

$$\frac{\partial T}{\partial t}=\kappa_{ob}\nabla^2 T \quad \text{(A.18)}$$

$$\frac{\partial T}{\partial t}=\kappa_{ub}\nabla^2 T \quad \text{(A.19)}$$

Appendix B

Regular line drive

B.1 Inspectional analysis

After the physical process is formulated, we use scale factors and follow the work of previous researchers to non-dimensionalize the equations (Shook et al., 1992; Novakovic, 2002; Wood et al., 2008; Jin et al., 2010). The equations listed in Chapter 3 involve twenty three parameters ($\phi, c_t, c_f, \beta_t, \beta_f, M, k_x, k_z, L, H, \kappa, \kappa'_{ob}, \kappa'_{ub}, \rho_f, p_i, T_{avg}, T_{inj}, \tau, \alpha, q, \mu$) and seven variables ($x, z, u_x, u_z, p, T, t$) to be scaled using Eqs. B.1. In these linear combinations, the quantities with an asterisk "*" are called scale factors and subscripts "1" and "2" and "D" indicate the multiplicative and additive scale factors and dimensionless variables, respectively.

$$
\begin{aligned}
x &= x_1^* x_D + x_2^* \\
z &= z_1^* z_D + z_2^* \\
u_x &= u_{x1}^* u_{xD} + u_{x2}^* \\
u_z &= u_{z1}^* u_{zD} + u_{z2}^* \\
p &= p_1^* p_D + p_2^* \\
T &= T_1^* T_D + T_2^* \\
t &= t_1^* t_D + t_2^*
\end{aligned}
\tag{B.1}
$$

Substituting scaled variables into the equations transforms all the equations into the dimensionless space.

- Continuity equation

$$\begin{aligned}\frac{\partial p_D}{\partial t_D} - \frac{\beta_t}{c_t}\frac{T_1^*}{p_1^*}\frac{\partial T_D}{\partial t_D} &+ (u_{x1}^* u_{xD} + u_{x2}^*)(\frac{c_f}{\phi c_t}\frac{t_1^*}{x_1^*}\frac{\partial p_D}{\partial x_D} - \frac{\beta_f}{\phi c_t}\frac{T_1^* t_1^*}{p_1^* x_1^*}\frac{\partial T_D}{\partial x_D}) \\ &+ (u_{z1}^* u_{zD} + u_{z2}^*)(\frac{c_f}{\phi c_t}\frac{t_1^*}{z_1^*}\frac{\partial p_D}{\partial z_D} - \frac{\beta_f}{\phi c_t}\frac{T_1^* t_1^*}{p_1^* z_1^*}\frac{\partial T_D}{\partial z_D}) \\ &+ \frac{1}{\phi c_t}\frac{u_{x1}^* t_1^*}{p_1^* x_1^*}\frac{\partial u_{xD}}{\partial x_D} + \frac{1}{\phi c_t}\frac{u_{z1}^* t_1^*}{p_1^* z_1^*}\frac{\partial u_{zD}}{\partial z_D} = 0\end{aligned} \tag{B.2}$$

- Darcy equation

$$u_{xD} = -\frac{k_x}{u_{x1}^* \mu}(\frac{p_1^*}{x_1^*}\frac{\partial p_D}{\partial x_D} - \rho_f g \sin\alpha) - \frac{u_{x2}^*}{u_{x1}^*} \tag{B.3}$$

$$u_{zD} = -\frac{k_z}{u_{z1}^* \mu}(\frac{p_1^*}{z_1^*}\frac{\partial p_D}{\partial z_D} - \rho_f g \cos\alpha) - \frac{u_{z2}^*}{u_{z1}^*} \tag{B.4}$$

- Energy equation

$$\begin{aligned}\frac{\partial T_D}{\partial t_D} &+ (u_{x1}^* u_{xD} + u_{x2}^*)\frac{t_1^*}{M x_1^*}\frac{\partial T_D}{\partial x_D} + (u_{z1}^* u_{zD} + u_{z2}^*)\frac{t_1^*}{M z_1^*}\frac{\partial T_D}{\partial z_D} \\ &+ (T_1^* T_D + T_2^*)(\frac{\phi c_t}{M}\frac{p_1^*}{T_1^*}\frac{\partial p_D}{\partial t_D} - \frac{\phi\beta_t}{M}\frac{\partial T_D}{\partial t_D}) \\ &- \kappa(\frac{t_1^*}{M x_1{*}^2}\frac{\partial^2 T_D}{\partial x_D^2} + \frac{t_1^*}{M z_1^{*^2}}\frac{\partial^2 T_D}{\partial z_D^2}) = 0\end{aligned} \tag{B.5}$$

- Reservoir boundary condition

$$\frac{T_1^*}{t_1^*}\frac{\partial T_D}{\partial t_D} = \kappa'_{ob}(\frac{T_1^*}{x_1^{*^2}}\frac{\partial^2 T_D}{\partial x_D^2} + \frac{T_1^*}{z_1^{*^2}}\frac{\partial^2 T_D}{\partial z_D^2}) \tag{B.6}$$

$$\frac{T_1^*}{t_1^*}\frac{\partial T_D}{\partial t_D} = \kappa'_{ub}(\frac{T_1^*}{x_1^{*^2}}\frac{\partial^2 T_D}{\partial x_D^2} + \frac{T_1^*}{z_1^{*^2}}\frac{\partial^2 T_D}{\partial z_D^2}) \tag{B.7}$$

$$u_{zD} = -\frac{u^*_{z2}}{u^*_{z1}} \quad At\ z_D = -\frac{z^*_2}{z^*_1}, \forall x_D, t_D \tag{B.8}$$

$$u_{zD} = -\frac{u^*_{z2}}{u^*_{z1}} \quad At\ z_D = \frac{H - z^*_2}{z^*_1}, \forall x_D, t_D \tag{B.9}$$

$$\frac{\partial T_D}{\partial x_D} = 0 \quad At\ x_D = 0, \forall z_D, t_D \tag{B.10}$$

$$\frac{\partial T_D}{\partial x_D} = 0 \quad At\ x_D = \frac{L - x^*_2}{x^*_1}, \forall z_D, t_D \tag{B.11}$$

- Injection

$$u_{xD} = \frac{u_T}{u^*_{x1}} \quad At\ x_D = \frac{L - x^*_2}{x^*_1}, \forall z_D, \forall t_D \tag{B.12}$$

$$T_D = \frac{T_{inj}}{T^*_1} \quad At\ x_D = -\frac{x^*_2}{x^*_1}, \forall z_D, \forall t_D \tag{B.13}$$

$$q_{inj} = u_T WH = -q_{prod} \tag{B.14}$$

- Production

$$u_{xD} = \frac{u_T}{u^*_{x1}} \quad At\ x_D = \frac{x^*_2}{x^*_1}, \forall z_D, \forall t_D \tag{B.15}$$

- Initial conditions

$$p_D = \frac{p_i}{p^*_1} \quad At \quad t_D = -\frac{t^*_2}{t^*_1} \quad \forall x_D, z_D \tag{B.16}$$

$$T_D = \frac{T_{avg}}{T_1^*} + \frac{\tau \cos\alpha}{T_1^*}(\frac{H}{2} - z_1^* z_D - z_2^*) + \frac{\tau \sin\alpha}{T_1^*}(\frac{L}{2} - x_1^* x_D - x_2^*) \quad \forall x_D, z_D, t \tag{B.17}$$

B.2 Dimensionless groups

The form of the equations should not change by transforming to dimensionless space. Many of these scaling groups can be set to zero or one (Eq. B.18). The remaining scaling groups that cannot be assigned any number defines the dimensionless groups required to describe the system. These remaining groups should also be analyzed for dependency to eliminate redundant dimensionless numbers and further be heuristically manipulated to achieve the most succinct form of the minimum dimensionless numbers. We further note that the dimensionless time is defined based on the energy equation.

$$u_{x2}^* = u_{z2}^* = z_2^* = x_2^* = t_2^* = T_2^* = p_2^* = 0 \tag{B.18}$$

$$x_1^* = L \qquad z_1^* = H$$

$$\frac{u_T}{u_{x1}^*} = 1 \Rightarrow u_{x1}^* = u_T \qquad \frac{u_{x1}^*}{x_1^*} = \frac{u_{z1}^*}{z_1^*} \Rightarrow u_{z1}^* = \frac{H}{L} u_T$$

$$T_1^* = T_{avg} \qquad t_1^* = M\frac{x_1^*}{u_{x1}^*} = M\frac{L}{u_t} = M\frac{PV}{\phi q}$$

$$p_1^* = \frac{u_T L \mu}{k_x}$$

Note that if the dimensionless time was defined based on the momentum equation, it was $t_{D_{hyd}} = \frac{\phi C_f}{C_t}\frac{qt}{LWH}$.

The use of scaling factors defines many of the dimensionless groups in Eqs. B.2-B.17. The sixteen remaining dimensionless numbers are no longer arbitrary and are specific to the described problem. They are:

$$\pi_1 = \frac{\phi c_t}{c_f} \qquad \pi_2 = \frac{\phi \beta_t}{\beta_f}$$

$$\pi_3 = M \qquad \pi_4 = c_f p_1^* = \frac{c_f \mu q L}{k_x W H}$$

$$\pi_5 = \beta_f T_1^* = \beta_f T_{avg} \qquad \pi_6 = \frac{L}{H}\sqrt{\frac{k_z}{k_x}}$$

$$\pi_7 = \frac{L}{H}\tan\alpha \qquad \pi_8 = \frac{L}{H}$$

$$\pi_9 = \frac{k_x \rho_f g \sin(\alpha) W H}{q\mu} \qquad \pi_{10} = \frac{q}{\kappa W}$$

$$\pi_{11} = \frac{\kappa'_{ob}}{\kappa} \qquad \pi_{12} = \frac{\kappa'_{ub}}{\kappa}$$

$$\pi_{13} = c_f p_i \qquad \pi_{14} = \frac{T_{inj}}{T_{avg}}$$

$$\pi_{15} = \frac{\tau \sin(\alpha) L}{T_{avg}}$$

B.3 Dimensionless model

- Continuity equation

$$\begin{aligned}\frac{\partial p_D}{\partial t_D} - (\frac{\pi_2}{\pi_1}\frac{\pi_5}{\pi_4})\frac{\partial T_D}{\partial t_D} &+ (\frac{\pi_3}{\pi_1})(\frac{\partial p_D}{\partial x_D} - (\frac{\pi_5}{\pi_4})\frac{\partial T_D}{\partial x_D}) \\ &+ (\frac{\pi_3}{\pi_1})(\frac{\partial p_D}{\partial z_D} - (\frac{\pi_5}{\pi_4})\frac{\partial T_D}{\partial z_D}) \\ &+ (\frac{\pi_3}{\pi_1})(\frac{1}{\pi_4})(\frac{\partial u_{xD}}{\partial x_D} + \frac{\partial u_{zD}}{\partial z_D}) = 0\end{aligned} \tag{B.19}$$

- Darcy equation

$$u_{xD} = -(\frac{\partial p_D}{\partial x_D} - \pi_9(1 + \pi_4 p_D - \pi_5 T_D)) \tag{B.20}$$

$$u_{zD} = -\pi_6^2(\frac{\partial p_D}{\partial z_D} - \frac{\pi_9}{\pi_7}(1 + \pi_4 p_D - \pi_5 T_D)) \tag{B.21}$$

- Energy equation

$$\begin{aligned} &\frac{\partial T_D}{\partial t_D} + (\frac{\partial T_D}{\partial x_D} + \frac{\partial T_D}{\partial z_D}) \\ &\quad -\pi_4(\frac{\partial p_D}{\partial t_D}) \\ &\quad -(\frac{1}{\pi_8 \pi_{10}})(\frac{\partial^2 T_D}{\partial x_D^2} + (\pi_8^2)\frac{\partial^2 T_D}{\partial z_D^2}) = 0 \end{aligned} \tag{B.22}$$

- Reservoir boundary condition

$$\frac{\partial T_D}{\partial t_D} = \frac{\pi_3 \pi_{11}}{\pi_8 \pi_{10}}(\frac{\partial^2 T_D}{\partial x_D^2} + \pi_8^2 \frac{\partial^2 T_D}{\partial z_D^2}) \tag{B.23}$$

$$\frac{\partial T_D}{\partial t_D} = \frac{\pi_3 \pi_{12}}{\pi_8 \pi_{10}}(\frac{\partial^2 T_D}{\partial x_D^2} + \pi_8^2 \frac{\partial^2 T_D}{\partial z_D^2}) \tag{B.24}$$

$$u_{zD} = 0 \quad At\ z_D = 0, \forall x_D, t_D \tag{B.25}$$

$$u_{zD} = 0 \quad At\ z_D = 1, \forall x_D, t_D \tag{B.26}$$

$$\frac{\partial T_D}{\partial x_D} = 0 \quad At\ x_D = 0, \forall z_D, t_D \tag{B.27}$$

$$\frac{\partial T_D}{\partial x_D} = 0 \quad At\ x_D = 1, \forall z_D, t_D \tag{B.28}$$

- Injection

$$u_{xD} = 1 \quad At\ x_D = 1,\ \ \forall z_D, t_D \tag{B.29}$$

$$T_D = \pi_{14} \quad At\ x_D = 0,\ \ \forall z_D, t_D \tag{B.30}$$

- Production

$$u_{xD} = 1 \quad At\ x_D = 0,\ \ \forall z_D, t_D \tag{B.31}$$

$$q_{prod} = -q_{inj} \tag{B.32}$$

- Initial conditions

$$p_D = \frac{\pi_{13}}{\pi_4} \quad At\ t_D = 0, \forall x_D, z_D \tag{B.33}$$

$$T_D = 1 + (\frac{\pi_{15}}{\pi_7})(\frac{1}{2} - z_D) + \pi_{15}(\frac{1}{2} - x_D) \quad At\ t_D = 0 \quad \forall x_D, z_D, \tag{B.34}$$

Appendix C

Zero Mass Withdrawal design

C.1 Inspectional analysis

After the physical process is formulated, we use scale factors and follow the work of previous researchers to non-dimensionalize the equations (Shook et al., 1992; Novakovic, 2002; Wood et al., 2008; Jin et al., 2010). The above equations involve twenty six parameters (ϕ, c_t, c_f, β_t, β_f, M, k_x, k_y, k_z, L, W, H , L_{prod}, L_{ins}, L_{inj}, κ, κ'_{ob}, κ'_{ub}, p_i, T_{avg}, T_{inj}, τ, α_X, α_Y, q, μ) and nine variables ($x, y, z, u_x, u_y, u_z, p, T, t$) to be scaled using Eqs. C.1. In these linear combinations, the quantities with an asterisk "*" are called scale factors and subscripts "1" and "2" and "D" indicate the multiplicative and additive scale factors and dimensionless variables, respectively.

$$
\begin{aligned}
x &= x_1^* x_D + x_2^* \\
y &= y_1^* y_D + y_2^* \\
z &= z_1^* z_D + z_2^* \\
u_x &= u_{x1}^* u_{xD} + u_{x2}^* \\
u_y &= u_{y1}^* u_{yD} + u_{y2}^* \\
u_z &= u_{z1}^* u_{zD} + u_{z2}^* \\
p &= p_1^* p_D + p_2^* \\
T &= T_1^* T_D + T_2^* \\
t &= t_1^* t_D + t_2^*
\end{aligned}
\tag{C.1}
$$

Substituting scaled variables into the equations, transforms all the equations into the dimensionless space.

- Continuity equation

$$\begin{aligned}\frac{\partial p_D}{\partial t_D}-\frac{\beta_t}{c_t}\frac{T_1^*}{p_1^*}\frac{\partial T_D}{\partial t_D}&+(u_{x1}^*u_{xD}+u_{x2}^*)(\frac{c_f}{\phi c_t}\frac{t_1^*}{x_1^*}\frac{\partial p_D}{\partial x_D}-\frac{\beta_f}{\phi c_t}\frac{T_1^*t_1^*}{p_1^*x_1^*}\frac{\partial T_D}{\partial x_D})\\&+(u_{y1}^*u_{yD}+u_{y2}^*)(\frac{c_f}{\phi c_t}\frac{t_1^*}{y_1^*}\frac{\partial p_D}{\partial y_D}-\frac{\beta_f}{\phi c_t}\frac{T_1^*t_1^*}{p_1^*y_1^*}\frac{\partial T_D}{\partial y_D})\\&+(u_{z1}^*u_{zD}+u_{z2}^*)(\frac{c_f}{\phi c_t}\frac{t_1^*}{z_1^*}\frac{\partial p_D}{\partial z_D}-\frac{\beta_f}{\phi c_t}\frac{T_1^*t_1^*}{p_1^*z_1^*}\frac{\partial T_D}{\partial z_D})\\&+\frac{1}{\phi c_t}\frac{u_{x1}^*t_1^*}{p_1^*x_1^*}\frac{\partial u_{xD}}{\partial x_D}+\frac{1}{\phi c_t}\frac{u_{y1}^*t_1^*}{p_1^*y_1^*}\frac{\partial u_{yD}}{\partial y_D}+\frac{1}{\phi c_t}\frac{u_{z1}^*t_1^*}{p_1^*z_1^*}\frac{\partial u_{zD}}{\partial z_D}=0\end{aligned}\tag{C.2}$$

- Darcy equation

$$u_{xD}=-\frac{k_x}{u_{x1}^*\mu}(\frac{p_1^*}{x_1^*}\frac{\partial p_D}{\partial x_D}-\rho_f\,g\sin\alpha_X\cos\alpha_Y)-\frac{u_{x2}^*}{u_{x1}^*}\tag{C.3}$$

$$u_{yD}=-\frac{k_y}{u_{y1}^*\mu}(\frac{p_1^*}{y_1^*}\frac{\partial p_D}{\partial y_D}-\rho_f\,g\cos\alpha_X\sin\alpha_Y)-\frac{u_{y2}^*}{u_{y1}^*}\tag{C.4}$$

$$u_{zD}=-\frac{k_z}{u_{z1}^*\mu}(\frac{p_1^*}{z_1^*}\frac{\partial p_D}{\partial z_D}-\rho_f\,g\cos\alpha_X\cos\alpha_Y)-\frac{u_{z2}^*}{u_{z1}^*}\tag{C.5}$$

- Energy equation

$$\begin{aligned}\frac{\partial T_D}{\partial t_D}&+(u_{x1}^*u_{xD}+u_{x2}^*)\frac{t_1^*}{Mx_1^*}\frac{\partial T_D}{\partial x_D}+(u_{y1}^*u_{yD}+u_{y2}^*)\frac{t_1^*}{My_1^*}\frac{\partial T_D}{\partial y_D}\\&+(u_{z1}^*u_{zD}+u_{z2}^*)\frac{t_1^*}{Mz_1^*}\frac{\partial T_D}{\partial z_D}\\&+(T_1^*T_D+T_2^*)(\frac{\phi c_t}{M}\frac{p_1^*}{T_1^*}\frac{\partial p_D}{\partial t_D}-\frac{\phi\beta_t}{M}\frac{\partial T_D}{\partial t_D})\\&-\kappa(\frac{t_1^*}{Mx_1^{*^2}}\frac{\partial^2T_D}{\partial x_D^2}+\frac{t_1^*}{My_1^{*^2}}\frac{\partial^2T_D}{\partial y_D^2}+\frac{t_1^*}{Mz_1^{*^2}}\frac{\partial^2T_D}{\partial z_D^2})=0\end{aligned}\tag{C.6}$$

$$\frac{\partial T_D}{\partial t_D}=\kappa'_{ob}(\frac{t_1^*}{x_1^{*^2}}\frac{\partial^2T_D}{\partial x_D^2}+\frac{t_1^*}{y_1^{*^2}}\frac{\partial^2T_D}{\partial y_D^2}+\frac{t_1^*}{z_1^{*^2}}\frac{\partial^2T_D}{\partial z_D^2})\tag{C.7}$$

$$\frac{\partial T_D}{\partial t_D} = \kappa'_{ub}\left(\frac{t_1^*}{x_1^{*^2}}\frac{\partial^2 T_D}{\partial x_D^2} + \frac{t_1^*}{y_1^{*^2}}\frac{\partial^2 T_D}{\partial y_D^2} + \frac{t_1^*}{z_1^{*^2}}\frac{\partial^2 T_D}{\partial z_D^2}\right) \tag{C.8}$$

- Reservoir boundary conditions

$$u_{xD} = -\frac{u_{x2}^*}{u_{x1}^*},\ \frac{\partial T_D}{\partial x_D} = 0 \quad At\ x_D = -\frac{x_2^*}{x_1^*}, \forall y_D^*, z_D^*, t_D^* \tag{C.9}$$

$$u_{xD} = -\frac{u_{x2}^*}{u_{x1}^*},\ \frac{\partial T_D}{\partial x_D} = 0 \quad At\ x_D = \frac{L - x_2^*}{x_1^*}, \forall y_D^*, z_D^*, t_D^* \tag{C.10}$$

$$u_{yD} = -\frac{u_{y2}^*}{u_{y1}^*},\ \frac{\partial T_D}{\partial y_D} = 0 \quad At\ y_D = -\frac{y_2^*}{y_1^*}, \forall x_D^*, z_D^*, t_D^* \tag{C.11}$$

$$u_{yD} = -\frac{u_{y2}^*}{u_{y1}^*},\ \frac{\partial T_D}{\partial y_D} = 0 \quad At\ y_D = \frac{W - y_2^*}{y_1^*}, \forall x_D^*, z_D^*, t_D^* \tag{C.12}$$

$$u_{zD} = -\frac{u_{z2}^*}{u_{z1}^*},\ \frac{\partial T_D}{\partial z_D} = 0 \quad At\ z_D = -\frac{z_2^*}{z_1^*}, \forall x_D^*, y_D^*, t_D^* \tag{C.13}$$

$$u_{zD} = -\frac{u_{z2}^*}{u_{z1}^*},\ \frac{\partial T_D}{\partial z_D} = 0 \quad At\ z_D = \frac{H - z_2^*}{z_1^*}, \forall x_D^*, y_D^*, t_D^* \tag{C.14}$$

- Initial conditions

$$p_D = \frac{p_i - p_2^*}{p_1^*} \quad At \quad t_D = -\frac{t_2^*}{t_1^*} \quad \forall x_D^*, y_D^*, z_D^*, t_D^* \tag{C.15}$$

$$\begin{aligned} T_D = \frac{T_{avg}}{T_1^*} &+ \frac{\tau \sin\alpha_X \cos\alpha_Y}{T_1^*}\left(\frac{L}{2} - x_1^* x_D - x_2^*\right) \\ &+ \frac{\tau \sin\alpha_Y \cos\alpha_X}{T_1^*}\left(\frac{W}{2} - y_1^* y_D - y_2^*\right) \\ &+ \frac{\tau \cos\alpha_X \cos\alpha_Y}{T_1^*}\left(\frac{H}{2} - z_1^* z_D - z_2^*\right) \quad \forall x_D^*, y_D^*, z_D^*, t_D^* \end{aligned} \tag{C.16}$$

C.1.1 Dimensionless groups

The form of the equations should not change by transforming to dimensionless space. Many of these scaling groups can be set to zero or one (Eq. C.17). The remaining scaling groups that cannot be assigned any number defines the dimensionless groups required to describe the system. These remaining groups should also be analyzed for dependency to eliminate redundant dimensionless numbers and further be heuristically manipulated to achieve the most succinct form of the minimum dimensionless numbers.

$$u_{x2}^* = u_{y2}^* = u_{z2}^* = x_2^* = y_2^* = z_2^* = t_2^* = 0 \tag{C.17}$$

Following the discussion on scaling the dimensions of a ZMW system, we have:

$$x_1^* = L_{prod} + L_{ins} + L_{inj} \qquad y_1^* = L_{ins} \tag{C.18}$$

Using Eq. C.17 and from the continuity equation we have:

$$\frac{u_{x1}}{x_1^*} = \frac{u_{y1}}{y_1^*} = \frac{u_{z1}}{z_1^*} \tag{C.19}$$

Other scaling groups can be set to one, thus other scaling factors become:

$$\begin{aligned} z_1^* &= H \\ u_{x1}^* &= \frac{q}{L_{ins}\, H} \\ u_{y1}^* &= \frac{q}{(L_{prod} + L_{ins} + L_{inj})H} \\ u_{z1}^* &= \frac{q}{(L_{prod} + L_{ins} + L_{inj})L_{ins}} \\ T_1^* &= T_{avg} \end{aligned}$$

Because the focus of the study is to model thermal recovery factor and production temperature, we use energy equation for defining the scaling factor for time (t_1^*). Pressure can be scaled using the Darcy equation.

$$t_1^* = M\frac{z_1^*}{u_{z1}^*} = M\frac{H(L_{prod}+L_{ins}+L_{inj})L_{ins}}{q}$$
$$p_1^* = \frac{u_{x1}^*\mu x_1^*}{k_x} = \frac{\mu}{k_x}q\frac{L_{prod}+L_{ins}+L_{inj}}{HL_{ins}}$$

The use of scaling factors define many of the dimensionless groups in Eqs. C.2-C.16. The nineteen remaining dimensionless numbers are no longer arbitrary and are specific to the described problem. They are:

$$\pi_1 = \frac{\phi c_t}{c_f} \qquad \pi_2 = \frac{\phi\beta_t}{\beta_f}$$
$$\pi_3 = M \qquad \pi_4 = c_f p_1^* = \frac{c_f\mu q(L_{prod}+L_{ins}+L_{inj})}{HL_{ins}}$$
$$\pi_5 = \beta_f T_1^* = \beta_f T_{avg} \qquad \pi_6 = \frac{(L_{prod}+L_{ins}+L_{inj})}{H}\sqrt{\frac{k_z}{k_x}}$$
$$\pi_7 = \frac{L_{ins}}{H}\sqrt{\frac{k_z}{k_y}} \qquad \pi_8 = \frac{(L_{prod}+L_{ins}+L_{inj})}{H}\tan(\alpha_X)$$
$$\pi_9 = \frac{L_{ins}}{H}\tan(\alpha_Y) \qquad \pi_{10} = \frac{L_{prod}}{H}$$
$$\pi_{11} = \frac{L_{inj}}{H} \qquad \pi_{12} = \frac{L_{ins}}{H}$$
$$\pi_{13} = \frac{k_x}{\mu}\frac{\rho_f g\sin\alpha_X\cos\alpha_Y L_{ins}H}{q} \qquad \pi_{14} = \frac{u_{x1}^* z_1^*}{\kappa} = \frac{q}{\kappa L_{ins}}$$
$$\pi_{15} = \frac{\kappa'_{ob}}{\kappa} \qquad \pi_{16} = \frac{\kappa'_{ub}}{\kappa}$$
$$\pi_{17} = c_f\, p_i \qquad \pi_{18} = \frac{T_{inj}}{T_{avg}}$$
$$\pi_{19} = \frac{\tau\sin\alpha_X\cos\alpha_Y(L_{prod}+L_{ins}+L_{inj})}{T_{avg}}$$

C.2 Dimensionless model

- Continuity equation

$$\begin{aligned}\frac{\partial p_D}{\partial t_D} - (\frac{\pi_5\pi_1}{\pi_4\pi_2})\frac{\partial T_D}{\partial t_D} + \frac{\pi_3}{\pi_1}(\frac{\partial p_D}{\partial x_D} - \frac{\pi_5}{\pi_4}\frac{\partial T_D}{\partial x_D}) \\ + \frac{\pi_3}{\pi_1}(\frac{\partial p_D}{\partial y_D} - \frac{\pi_5}{\pi_4}\frac{\partial T_D}{\partial y_D}) \\ + \frac{\pi_3}{\pi_1}(\frac{\partial p_D}{\partial z_D} - \frac{\pi_5}{\pi_4}\frac{\partial T_D}{\partial z_D}) \\ + (\frac{\pi_3}{\pi_1\pi_4})(\frac{\partial u_{xD}}{\partial x_D} + \frac{\partial u_{yD}}{\partial y_D} + \frac{\partial u_{zD}}{\partial z_D}) = 0\end{aligned} \tag{C.20}$$

- Darcy equation

$$u_{xD} = -\frac{\partial p_D}{\partial x_D} - \pi_{13} \tag{C.21}$$

$$u_{yD} = -(\frac{\pi_{10} + \pi_{11} + \pi_{12}}{\pi_{12}})^2\frac{\partial p_D}{\partial y_D} - \frac{\pi_{13}\pi_9\pi_6^2}{\pi_8\pi_7^2} \tag{C.22}$$

$$u_{zD} = -\pi_6^2\frac{\partial p_D}{\partial z_D} - \frac{\pi_{13}\pi_6^2}{\pi_8} \tag{C.23}$$

- Energy equation

$$\begin{aligned}&\frac{\partial T_D}{\partial t_D} + (\frac{\partial T_D}{\partial x_D} + \frac{\partial T_D}{\partial y_D} + \frac{\partial T_D}{\partial z_D}) \\ &\quad + (\frac{1}{\pi_3})(\pi_1\pi_4\frac{\partial p_D}{\partial t_D} - \pi_2\pi_5\frac{\partial T_D}{\partial t_D}) \\ &\quad - (\frac{1}{\pi_{14}})\left((\frac{1}{\pi_{10} + \pi_{11} + \pi_{12}})\frac{\partial^2 T_D}{\partial x_D^2} + (\frac{\pi_{10} + \pi_{11} + \pi_{12}}{\pi_{12}^2})\frac{\partial^2 T_D}{\partial y_D^2} + (\pi_{10} + \pi_{11} + \pi_{12})\frac{\partial^2 T_D}{\partial z_D^2}\right) = 0\end{aligned}$$

- Reservoir boundary conditions

$$\frac{\partial T_D}{\partial t_D} = (\frac{\pi_3\pi_{15}}{\pi_{14}})\left((\frac{1}{\pi_{10}+\pi_{11}+\pi_{12}})\frac{\partial^2 T_D}{\partial x_D^2} + (\frac{\pi_{10}+\pi_{11}+\pi_{12}}{\pi_{12}^2})\frac{\partial^2 T_D}{\partial y_D^2} + (\pi_{10}+\pi_{11}+\pi_{12})\frac{\partial^2 T_D}{\partial z_D^2}\right) \tag{C.24}$$

$$\frac{\partial T_D}{\partial t_D} = (\frac{\pi_3\pi_{16}}{\pi_{14}})\left((\frac{1}{\pi_{10}+\pi_{11}+\pi_{12}})\frac{\partial^2 T_D}{\partial x_D^2} + (\frac{\pi_{10}+\pi_{11}+\pi_{12}}{\pi_{12}^2})\frac{\partial^2 T_D}{\partial y_D^2} + (\pi_{10}+\pi_{11}+\pi_{12})\frac{\partial^2 T_D}{\partial z_D^2}\right) \tag{C.25}$$

$$u_{xD} = 0,\ \frac{\partial T_D}{\partial x_D} = 0 \quad At\ x_D = 0, \forall y_D, z_D, t_D \tag{C.26}$$

$$u_{xD} = 0,\ \frac{\partial T_D}{\partial x_D} = 0 \quad At\ x_D = 1, \forall y_D, z_D, t_D \tag{C.27}$$

$$u_{yD} = 0,\ \frac{\partial T_D}{\partial y_D} = 0 \quad At\ y_D = 0, \forall x_D, z_D, t_D \tag{C.28}$$

$$u_{yD} = 0,\ \frac{\partial T_D}{\partial y_D} = 0 \quad At\ y_D = 1, \forall x_D, z_D, t_D \tag{C.29}$$

$$u_{zD} = 0,\ \frac{\partial T_D}{\partial z_D} = 0 \quad At\ z_D = 0, \forall x_D, y_D, t_D \tag{C.30}$$

$$u_{zD} = 0,\ \frac{\partial T_D}{\partial z_D} = 0 \quad At\ z_D = 1, \forall x_D, y_D, t_D \tag{C.31}$$

- Initial conditions

$$p_D = \frac{\pi_{17}}{\pi_4} \quad At \quad t_D = 0 \quad \forall x_D, y_D, z_D \tag{C.32}$$

$$T_D = 1 + (\pi_{19})(\frac{1}{2} - x_D) + (\frac{\pi_9\pi_{19}}{\pi_8})(\frac{1}{2} - y_D) + (\frac{\pi_{19}}{\pi_8})(\frac{1}{2} - z_D) \quad \forall x_D, y_D, z_D, t_D \tag{C.33}$$

Appendix D

Tables

Table D.1: Parameters and dimensionless numbers of the fifteen reservoirs used in the line drive validation study

Color	T_{avg}	T_{inj}	Length	Width	Thickness	q	π_7	π_8	π_9	π_{10}	π_{14}	π_{15}
Green	117.7231	41.20308	8370	77.6923	62	67.03419	25	135	11765	20	0.35	1.75
Green	145.2924	50.85235	13365	88.15585	99	76.0959	25	135	11765	20	0.35	1.75
Green	117.6128	41.16448	17145	77.60251	127	66.95646	25	135	11765	20	0.35	1.75
Green	131.2866	45.9503	15120	72.38119	112	62.47178	25	135	11765	20	0.35	1.75
Green	123.2541	43.13895	9720	64.9294	72	56.03065	25	135	11765	20	0.35	1.75
Blue	144.7008	95.79194	9180	132.3458	68	342.7211	30	135	11765	60	0.662	1.75
Blue	115.7777	76.64485	17685	68.68726	131	177.7817	30	135	11765	60	0.662	1.75
Blue	118.6059	78.51708	15930	66.26117	118	171.5188	30	135	11765	60	0.662	1.75
Blue	116.238	76.94953	11070	100.5957	82	260.3737	30	135	11765	60	0.662	1.75
Blue	134.8069	89.24215	18225	75.42822	135	195.3134	30	135	11765	60	0.662	1.75
Red	118.0974	59.75727	7480	145.0222	88	625.6456	25	85	11765	100	0.506	1.75
Red	125.385	63.44482	8500	114.6313	100	494.628	25	85	11765	100	0.506	1.75
Red	141.1314	71.4125	8840	145.9744	104	630.0176	25	85	11765	100	0.506	1.75
Red	117.9554	59.68541	11900	145.9291	140	629.5552	25	85	11765	100	0.506	1.75
Red	114.2298	57.80028	6885	142.9264	81	616.5229	25	85	11765	100	0.506	1.75

Table D.2: Parameters and dimensionless numbers of the fifteen reservoirs used in the ZMW validation study.

Color	T_{avg}	T_{inj}	$Thickness$	L_{ins}	L_{inj}	L_{prod}	q	π_6	π_7	π_{10}	π_{11}	π_{12}	π_{14}	π_{18}
Green	118.3574	23.67148	99.70753	199.4151	199.4151	1310.452	196.3046	5.421078	0.632456	13.14296	2	2	18.5185	0.2
Green	128.349	25.6698	96.94622	193.8924	193.8924	1274.16	191.8899	5.421078	0.632456	13.14296	2	2	18.5185	0.2
Green	143.6772	28.73543	106.9195	213.8391	213.8391	1405.239	213.3547	5.421078	0.632456	13.14296	2	2	18.5185	0.2
Green	144.7976	28.95953	73.77835	147.5567	147.5567	969.6656	147.309	5.421078	0.632456	13.14296	2	2	18.5185	0.2
Green	129.1785	25.83571	95.62628	191.2526	191.2526	1256.812	189.3614	5.421078	0.632456	13.14296	2	2	18.5185	0.2
Blue	119.4492	23.88984	65.29774	391.7864	391.7864	335.8234	385.9003	5.421078	1.897367	5.142955	6	6	18.5185	0.2
Blue	140.8114	28.16228	78.76227	472.5736	472.5736	405.0708	470.7961	5.421078	1.897367	5.142955	6	6	18.5185	0.2
Blue	120.2576	24.05153	94.11801	564.708	564.708	484.0447	556.4641	5.421078	1.897367	5.142955	6	6	18.5185	0.2
Blue	122.723	24.54459	65.28714	391.7229	391.7229	335.7688	386.5125	5.421078	1.897367	5.142955	6	6	18.5185	0.2
Blue	131.7886	26.35773	96.09262	576.5557	576.5557	494.2	571.6469	5.421078	1.897367	5.142955	6	6	18.5185	0.2
Red	134.2922	65.11155	48.33744	290.0246	193.3498	966.7633	287.9371	9.486928	1.897367	20.0003	4	6	18.5185	0.48485
Red	136.4804	66.17251	47.20481	283.2289	188.8193	944.1104	281.5168	9.486928	1.897367	20.0003	4	6	18.5185	0.48485
Red	133.29	64.62564	51.35746	308.1448	205.4299	1027.165	305.7643	9.486928	1.897367	20.0003	4	6	18.5185	0.48485
Red	147.5932	71.56055	54.85118	329.1071	219.4047	1097.04	329.037	9.486928	1.897367	20.0003	4	6	18.5185	0.48485
Red	131.7554	63.88162	57.36765	344.2059	229.4706	1147.37	341.2693	9.486928	1.897367	20.0003	4	6	18.5185	0.48485

Table D.3: Parameters used in the Box-Behnken experimental design for the line drive system. Level 0 indicates a normal score transform mean of the parameter; level ±1 indicates values that are ±2 standard deviations away from the normal score mean values.

Level	T_{avg} (C)	T_{inj} (C)	τ (C/m)	$Length$ (m)	$Thickness(m)$	$Dip angle$	K_z/K_x	$Poro.$
-1	100.3	30	0.024	2000	33.1	0	0.1	0.14
0	133.7	60	0.0255	3000	103.4	5	0.5	0.22
+1	167.2	90	0.027	4000	173.8	10	1	0.30

Level	Q (m^3/day)	β_r (C^{-1})	β_f (C^{-1})	Cp_r $(J/m^3.C)$	Cp_{ob} $(J/m^3.C)$	Cp_f $(J/m^3.C)$
-1	500	0.5×10^{-5}	6×10^{-4}	1.5×10^6	1.5×10^6	3.9×10^6
0	1250	1×10^{-5}	8×10^{-4}	2×10^6	2×10^6	4×10^6
+1	2000	1.5×10^{-5}	10×10^{-4}	2.5×10^6	2.5×10^6	4.1×10^6

Level	k_r $(J/m.day.C)$	k_{ob} $(J/m.day.C)$	k_f $(J/m.day.C)$	C_r (kpa^{-1})	C_f (kpa^{-1})	$Perm.$ (md)
-1	1.5×10^5	1.5×10^5	5.5×10^4	1×10^{-6}	3.5×10^{-7}	19
0	2×10^5	2×10^5	5.9×10^4	2.5×10^{-7}	4.5×10^{-7}	127
+1	2.5×10^5	2.5×10^5	6.3×10^4	5×10^{-7}	5.5×10^{-7}	235

Table D.4: Parameters used in the Box-Behnken experimental design for the ZMW system.

Level	T_{avg} (C)	T_{inj} (C)	$Thickness$ (m)	L_{prod} (m)	L_{ins} (m)	L_{inj} (m)	Q (m^3/day)	α_x
-1	100.3	30	33.1	100	100	100	500	2.5
0	133.7	60	103.4	400	400	400	1250	13.8
+1	167.2	90	173.8	700	700	700	2000	25

Level	β_r (C^{-1})	β_f (C^{-1})	Cp_r $(J/m^3.C)$	Cp_{ob} $(J/m^3.C)$	Cp_f $(J/m^3.C)$	k_r $(J/m.day.C)$
-1	0.5×10^{-5}	6×10^{-4}	1.5×10^6	1.5×10^6	3.9×10^6	1.5×10^5
0	1×10^{-5}	8×10^{-4}	2×10^6	2×10^6	4×10^6	2×10^5
+1	1.5×10^{-5}	10×10^{-4}	2.5×10^6	2.5×10^6	4.1×10^6	2.5×10^5

Level	k_{ob} $(J/m.day.C)$	k_f $(J/m.day.C)$	C_r (kpa^{-1})	C_f (kpa^{-1})	K_z/K_x	$Perm.(md)$	$Poro.$
-1	1.5×10^5	5.5×10^4	1×10^{-6}	3×10^{-7}	0.1	19	0.14
0	2×10^5	5.9×10^4	2.5×10^{-7}	4×10^{-7}	0.5	127	0.22
+1	2.5×10^5	6.3×10^4	5×10^{-7}	5×10^{-7}	1	235	0.30

Vita

Esmail Ansari, son of Ahmad and Kheyronnesa, was born in Fars province, Iran. He started his B.S. studies in petroleum engineering at Sharif University of Technology, Tehran, and graduated in September 2009. He continued his M.S. studies at the same university and graduated in November 2011. He joined Louisiana State University in January 2012 and is expected to receive his Doctor of Philosophy from Craft and Hawkins Department of Petroleum Engineering in May 2016. Esmail plays soccer and enjoys swimming.